INVESTIGATING METAL HOMEOSTASIS IN MAMMALIAN CELLS USING HIGH RESOLUTION IMAGING TECHNIQUES

A Thesis
Presented to
The Academic Faculty

by

Reagan L. McRae

In Partial Fulfillment
Of the Requirements for the Degree
Doctor of Philosophy in the
School of Chemistry and Biochemistry

Georgia Institute of Technology
August 2010

INVESTIGATING METAL HOMEOSTASIS IN MAMMALIAN CELLS USING HIGH RESOLUTION IMAGING TECHNIQUES

Approved by:

Dr. Christoph J. Fahrni, Advisor
School of Chemistry and Biochemistry
Georgia Institute of Technology

Dr. Nael McCarty
Department of Pediatrics
Emory University

Dr. Uwe Bunz
School of Chemistry and Biochemistry
Georgia Institute of Technology

Dr. Jake Soper
School of Chemistry and Biochemistry
Georgia Institute of Technology

Dr. Donald Doyle
School of Chemistry and Biochemistry
Georgia Institute of Technology

Date Approved: June 08, 2010

ACKNOWLEDGEMENTS

I gratefully acknowledge Professor Christoph J. Fahrni for his steadfast encouragement and guidance throughout my graduate school career. I appreciate his support and, most of all, his allowing me the freedom to pursue a wide range of endeavors. I appreciate the support of the past and current members of the Fahrni group with whom it has been a pleasure to work. I appreciate the support of the members of the Doyle lab group. I appreciate the unconditional support and friendship given to me by Dr. Karl Huettinger. He has been a wonderful friend and it was a pleasure working with him in the Fahrni group. I thank Dr. Bahareh Azizi, Banafsheh Azizi, Dr. Kenyetta Johnson, Jennifer Taylor, and Hilda Castillo for their support and friendship. I appreciate Dr. Nael McCarty for his support and much needed help with my presentation skills. I thank Dr. Donald Doyle for supporting me and for playing a fundamental role in my persistence through graduate school. I thank Dr. Uwe Bunz for his support and the Bunz research group for treating me like a member of their group. I appreciate the guidance and support of Dr. Barry Lai and Dr. Stefan Vogt at Argonne National Laboratory. I express my gratitude to my family, to all of my friends, and to my committee for their assistance and support throughout the years.

I am grateful for the financial support provided by Georgia Institute of Technology and the National Institute of Health (Grants R01GM067169 and R01DK68096). I appreciate the use of the Advanced Photon Source at Argonne National Laboratory financially supported by the U.S. Department of Energy, Office of Science, Office of Basic Energy Sciences, under Contract No. W-31-109-Eng-38.

TABLE OF CONTENTS

LIST OF FIGURES

List of Abbreviations

1PA	One-photon Absorption
2PA	Two-photon Absorption
AD	Alzheimer's Disease
ALS	Amyotrophic Lateral Sclerosis
APS	Advanced Photon Source
Atox1	Antioxidant 1
ATP7a	Menkes' ATPase
ATP7b	Wilson's ATPase
CCS	Copper Chaperone for Superoxide Dismutase
CTAP-1	Cu(I)-selective Fluorescent Probe 1
Ctr1	Copper Transporter 1

DMEM	Dulbecco's Modified Eagle's Medium
DTO	3,6-dithia-1,8-octanediol
EM	Electron Microscopy
EPXMA	Electron Probe X-ray Microanalysis
ER	Endoplasmic Reticulum
GA	Golgi Apparatus
GFP	Green Fluorescent Protein
H_2O_2	Hydrogen Peroxide
IMS	Inner Membrane Space
LA-ICP-MS	Laser Ablation-Inductively Couples Plasma-Mass Spectrometry
MD	Menkes' Disease
MRI	Magnetic Resonance Imaging

MT	Metallothionein
NIR	Near-Infrared Radiation
PD	Parkinson's Disease
PDB	Protein Data Bank
PET	Positron Emission Tomography
Pyr	Pyrithione
RFP	Red Fluorescent Protein
Si_3N_4	Silicon Nitride
SIMS	Secondary Ion Mass Spectrometry
SOARS	Statistical Optimization Analysis for Ratiometric Signals
SVD	Singular Value Decomposition
SXRF	Synchrotron radiation x-ray fluorescence

TGN	Trans Golgi Network
TPA	Two Photon Absorption
TPEM	Two-photon Excitation Microscopy
TPEN	N,N,N',N'-tetrakis-(2-pyridylmethyl)-ethylenediamine
TTM	Tetrathiomolybdate
WD	Wilson's Disease
XANES	X-ray Absorption Near Edge Spectroscopy
XAS	X-ray absorption
XRF	X-ray fluorescence
ZIP	Zn^{2+} regulatory transporter, iron regulatory metal transporter-like protein
ZnT	Zn^{2+} transporter

SUMMARY

Copper and zinc are essential trace elements that are important for a diverse spectrum of biological processes. Over the past two decades, it has become increasingly evident that a number of severe diseases including Alzheimer's disease, Parkinson's disease, diabetes, and cancer are associated with impaired copper and/or zinc homeostasis. The primary aim of the work presented in this thesis is to elucidate novel information regarding the uptake, storage, distributions, and functions of both copper and zinc in mammalian cells by predominantly using a combination of the high resolution imaging modalities, synchrotron radiation X-ray fluorescence microscopy (SXRF) and standard fluorescence imaging.

Chapter 1 introduces a general summary of the roles for metals in nature as well as detailed descriptions and recent developments in the field of metal detection in situ.

In Chapter 2, a Cu(I)-selective fluorescent probe is characterized in mammalian cells. The fluorescent probe, CTAP-1 shows an approximate 3-fold fluorescence emission enhancement, upon supplementation of cells with excess copper. The enhancement could be reversed to baseline fluorescence in the presence of excess amounts of a cell permeable copper chelator, DTO. SXRF analysis shows a strong correlation between the fluorescence of CTAP-1 with the 2D copper topography. Additionally, immunofluorescence analysis reveals strong co-localization between the probe fluorescence with the mitochondria and Golgi apparatus.

Chapter 3 highlights the intracellular characterization of a Zn(II)-selective ratiometric fluorescence probe, SL-326. Co-localization experiments revealed the presence of labile zinc pools within the mitochondria, ER, and associated with Rab5 vesicles. SXRF imaging revealed a strong correlation between the intracellular XRF Zn(II) distribution and the probe fluorescence, thus confirming the integrity of the probe. Additionally, dynamic imaging of SL-326 revealed a significant increase in the fluorescence ratio emission upon addition of Zn(II) to the extracellular milieu and upon perturbation of the cellular redox status by the addition of H_2O_2 to the growth media.

Chapter 4 discusses the development and application of a correlative SXRF and fluorescence imaging technique. By using ultrasmall gold-clusters as xenobiotic elemental labels, we were able to identify, based on the characteristic Au XRF elemental map, the sub-cellular location of individual organelles in adherent mouse fibroblast cells. Although we found a significant degree of non-specific binding in the nuclear area, presumably mediated through the gold-cluster label, the technique should be well suited to specifically label sub-cellular structures within the cytoplasm, and thus to study the elemental composition of organelles in single cells. SXRF imaging complements existing techniques, notably electron microscopy and optical fluorescence microscopy, in a synergistic fashion. By applying dual-labeled markers that contain a fluorescence reporter in combination with the ultrasmall gold-cluster, the three methods can be combined through correlative microscopy.

Chapter 5 provides an application of SXRF imaging to investigating metal distributions in a disease-model mouse cell line. Spatially well-resolved SXRF elemental maps of individual adherent mouse fibroblast cells revealed intriguing differences in the Cu distribution of Atox1$^{-/-}$ cells compared to the corresponding wild-type cells. While the latter cells showed a well-defined perinculear Cu localization, the copper distribution in Atox1$^{-/-}$ cells was reproducibly unstructured and diffuse throughout the entire cell. Although the SXRF elemental maps cannot reveal the nature of the associated cellular structure or organelles in the absence of a xenobiotic label, the characteristic perinuclear Cu distribution pattern might point towards the involvement of the Golgi apparatus, late endosomes, or mitochondria, all of which are typically found in the vicinity of the nuclear envelope. Therefore, the data highlight the importance of Atox1, not only as a metallochaperone for delivering Cu to essential cuproemzymes, but also as a key player in maintaining the proper distribution and organization of Cu at the cellular level.

Chapter 6 provides studies of elemental distributions and associated changes as cells progress through the cell cycle. Spatially well-resolved SXRF elemental maps of single, adherent mouse cells revealed remarkable changes in the distributions of both zinc and copper as the cells progressed through the cell cycle. Zinc and copper showed relatively homogenous nucleocytoplasmic distributions concentrating in regions of elevated sulfur as well as phosphorus for each stage of interphase. Conversely, upon the entry of cells into mitosis, zinc and copper moved from areas of significant phosphorus content to regions predominantly overlapping with sulfur. Furthermore, zinc showed an approximate 3-fold increase in its overall content upon the transition of cells from

interphase into mitosis. Although SXRF, in the absence of a xenobiotic label, is unable to provide information regarding the nature of the cellular structures and/or organelles associated with copper and zinc, evidence strongly points toward their localization within the mitotic spindle. Moreover, the data strongly point towards an association with the Golgi apparatus, particularly for zinc, given the overall similarity between their distributions during cell division. Taken together, the data highlight the potential importance of zinc as well as copper for the appropriate progression of cells through mitosis, a previously unconsidered notion in reports investigating the mechanistic details underscoring the progression of mammalian cells through the cell cycle.

Chapter 7 discusses the future directions of this research.

CHAPTER 1
INTRODUCTION

1.1 Biological Relevance of Metals

Approximately 1/3 of the human proteome contains metal cations, either in the form of cofactors with catalytic functions, or as structural support [1, 2]. To guarantee a proper maintenance of this metal ion pool, both at the cellular and whole organism levels, nature has evolved a highly sophisticated machinery comprised of a complex interplay between DNA, proteins, and biomolecules [3]. Over the past decades, a steadily growing number of diseases have been identified, which are characterized by metal imbalance in cells and tissues. Among the most prominent examples rank Alzheimer's disease and Parkinson's disease, two neurodegenerative disorders that involve abnormal accumulation of transition metals in brain tissue [4]. While some progress has been made towards understanding the molecular basis of these disorders, many important questions remain unanswered. For example, little is known about the cellular structures that are involved in transiently storing metal ions prior to their incorporation into metalloproteins or the fate of metal ions upon protein degradation. An important first step towards unraveling the regulatory mechanisms involved in trace metal transport, storage, and distribution represents the identification and quantification of the metals, ideally in context of their native physiological environment in tissues, cells, or even at the level of individual organelles and sub-cellular compartments.

Since the inception of the first histochemical methods for the microscopic demonstration of transition metals in tissues more than 140 years ago [5], many highly

sensitive microanalytical techniques and instruments have been developed for the in situ analysis of trace metals. The aim of this chapter is to provide an overview of the most recent achievements in trace metal imaging with a particular emphasis on fluorescence probe based detection and synchrotron radiation X-ray fluorescence (SXRF) imaging methods. A detailed description of the biological relevance of the individual metals investigated within the context of this thesis will be provided as they are introduced in the subsequent chapters.

1.2 Overview of Methods for Metal Detection In Situ

An overview of the most important microanalytical techniques currently available for the in situ detection of trace metals in cells and tissues is compiled in Table 1.1 [6].

Table 1.1: Spatially resolved microanalytical techniques for in situ imaging of trace metals in biology [7-12]. Reproduced from reference [6].

Analytical Method	Detection Limit	Spatial Resolution (µm)	Analytical Depth (µm)	Quantification
Electron Probe X-ray Microanalysis (EPXMA) [7]	100 - 1000 µg/g	0.5	0.1 - 1	Semi-quantitative
Proton Beam Microprobe (PIXE, RBS, & STIM) [7]	1 - 10 µg/g	0.2 - 2	10 - 100	Quantitative (PIXE-RBS)
X-ray Microprobe (SXRF, µXAS, µXANES) [7, 8]	0.1 – 1 (SXRF) 100 (µXAS) µg/g	0.03 – 0.2	> 100	Quantitative
Laser Ablation - Inductively coupled plasma - mass spectrometry (LA-ICP-MS) [7]	0.01 µg/g	15 - 50	200	Semi-quantitative
Secondary Ion Mass Spectrometry (SIMS) [7]	0.1 µg/g	0.05	0.1	Quantitative
Magnetic Resonance Imaging (MRI) [9]	mM - low µM	25 - 100	no limit	Semi-quantitative
Positron Emission Tomography (PET) [9]	high pM	1000 - 2000	no limit	Semi-quantitative
Autoradiography [10]		0.1	no limit	Semi-quantitative
Autometallography [11, 12]	nM	low-mid nm (EM)	0.01-1 (EM)	Semi-quantitative
Optical Fluorescence Microscopy [10]	pM to nM	2000 – 3000 (in vivo) 0.2 - 0.5 (in vitro)	< 1 cm	Qualitative / Semi-quantitative
Visible Light Microscopy	low-µM	0.2 - 0.5	0.01-1	Qualitative

Depending on the task, each technique may offer specific advantages, as well as, disadvantages. Currently, synchrotron beam and focused ion beam microprobes presumably offer the best combination of sensitivity and spatial resolution; however, the ionizing high-energy excitation beam is not compatible with studying live organisms. Conversely, techniques specifically developed for physiological imaging in clinical medicine, notably magnetic resonance imaging and positron emission tomography, inherently offer only a low spatial resolution and are merely suitable for obtaining information at the organ or tissue level. Although fluorescence microscopy based methods provide very high sensitivity down to the single molecule level while simultaneously being compatible with live cell and tissue studies, scattering and limited penetration depth renders these techniques unsuitable for imaging opaque specimens. There are also important differences regarding the type of quantitative information that can be gained by each of these analytical techniques. For example, the histochemical detection with chromogenic and fluorogenic dyes relies on a competitive exchange of the metal ion within its native environment, most likely coordinated to endogenous ligands. Depending on the exchange kinetics and thermodynamic affinity of the histochemical indicator, only a fraction of the total metal ion contents in a cell or tissue can be probed. Nevertheless, this kinetically labile pool is of particular interest within the context of understanding the uptake and distribution of trace elements at the cellular level, and in this regard, these methods offer unique opportunities for dynamically imaging metal ion fluxes in living cells with high sensitivity and spatial resolution. At the same time, organelles and proteins of interest can be readily labeled with genetically encoded green fluorescent protein tags [13], thus offering an opportunity to understand the dynamic

processes in a larger cellular and biochemical context. In contrast, similar correlative information is difficult to gain with the fully quantitative focused ion-beam methods, which would depend on a xenobiotic tag for identifying sub-cellular structures. Autoradiographic tracer experiments offer much improved resolution over PET; however, the technique is only applicable to fixed or frozen tissues and cells. Furthermore, tracer studies cannot provide direct information regarding the endogenous metal composition of a system, and are primarily limited to metal uptake, distribution, and release studies. Finally, mass spectrometric analyses are surface-based methods that destroy the sample while measuring its elemental composition. Clearly, only the combination of several analytical techniques and specific biochemical studies may lead to a fully comprehensive analysis of a biological system.

1.3 Metal Detection with Fluorescence Probes

Histology is the branch of biology dealing with the study of microscopic anatomy of cells and tissues of plants and animals. Histological studies are typically carried out on thin sections of tissue or with cultured cells. To visualize and identify particular structures, a broad spectrum of histological stains and indicators are available. Among the most widely used dyes are hematoxylin and eosin, which stain nuclei blue and the cytoplasm pink, respectively [14]. The history of detecting biological trace metals by histological methods dates back more than 140 years. Although these techniques have been today mostly replaced by the much more sensitive modern analytical methods described in this review article, histochemical approaches for visualizing metals mark the very beginning in the exploration of the inorganic physiology of transition metals.

Compared with chromogenic histochemical stains, fluorescent dyes offer much greater optical sensitivity and harbor the potential for observing biological processes at the single-molecule level [15]. Because of their small molecular size, synthetic indicators may passively diffuse across cell membranes and are thus well suited for the non-invasive imaging of cation fluxes in living cells. Given these attractive properties, it is not surprising that the development of new fluorescent probes and indicators represents a very active and steadily growing research area [16]. At present, fluorescent indicators have been developed for most biologically relevant metal cations, including calcium, magnesium, sodium, potassium, zinc, copper, and iron [16, 17]. Furthermore, an increasing number of probes selective towards xenobiotic, toxic heavy metals have been described. Over the past decade, many excellent review articles summarizing these developments have been published, with topical areas covering both the principles and photophysics of probe design [18-21], as well as comprehensive overviews on fluorescence detection of selected metal ions, most notably zinc [22-29] and mercury [30]. Since studies of zinc and copper are the primary focus of this thesis, the following paragraphs discuss a few corner stones in the evolution of Zn(II)-selective and Cu(I)-selective fluorescence probes for biological applications.

For many years, dithizone was the only histochemical stain available for demonstrating Zn(II)-ions in tissues [31]. In 1969, Mahanand and Houck described the first fluorescence indicator for the selective detection of Zn(II) in blood plasma and urine using 8-hydroxy-quinoline (**1**, Figure 1.1) [32].

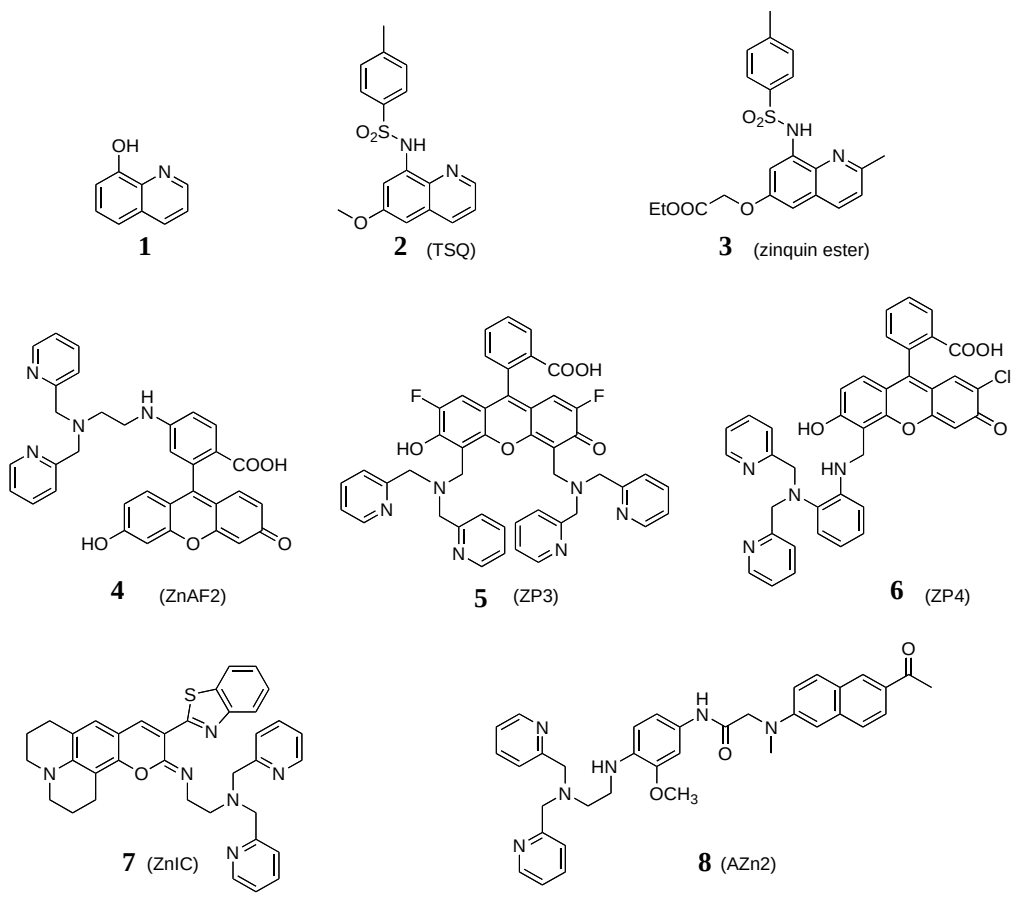

Figure 1.1: Chart of Zn(II)-selective fluorescence probes. Reprinted from ref [6].

While the indicator formed stable complexes with many divalent metal ions, only binding of Zn(II), Mg(II), and Ca(II) led to a strong fluorescence increase, with Zn(II) displaying the highest binding affinity [33]. Similarly, a 2-methyl-derivative of 8-hydroxy-quinoline was also described as histochemical Zn(II) indicator [34]. Structurally related to the 8-hydroxy-quinoline indicators, Toroptsev and Eschenko explored the utility of several quinoline sulfonamide derivatives as fluorescence probes for Zn(II) [35-39]. The bright green fluorescence was found to co-localize with the dithizone staining in pancreatic beta cells and hippocampal mossy fibres. In the 1980s, Frederickson et al. explored the utility of another quinoline derivative, 6-methoxy-8-p-toluene sulfonamide quinoline (TSQ, **2**)

as histological indicator for Zn(II) [40, 41]. A comparison of TSQ with the established neo-Timm method demonstrated that the indicator is well suited as stain for demonstrating histochemically reactive Zn(II) in various tissues. In order to improve the water solubility and cellular retention, TSQ was later further modified with a carboxylate group [42-45]. The resulting probe, zinquin ester (**3**), has been instrumental in elucidating the role of labile Zn(II) pools in a wide range of biological systems; however, the origin of the distinct vesicular staining pattern observed with zinquin ester remains controversial. To address the question whether these zinc-rich vesicles, also referred to as zincosomes, might arise from a dye-induced sequestration of Zn(II), Wellenreuther et al. performed in situ microXanes (section 1.4) measurements with RAW264.7 cells [46]. The in situ data matched the X-ray absorption near-edge signature of isolated vesicles and implied that Zn(II) is present in complexed form with a coordination environment composed of sulfur, nitrogen (histidine), and oxygen donor atoms.

To avoid potentially damaging UV excitation, several fluorescein-based probes tethered to varying chelating units have been recently developed for excitation in the visible spectral range. For example, the ZnAF family of fluorescent probe developed by Nagano and coworkers combined the fluorescein platform with N,N-bis(2-pyridylmethyl)ethylenediamine as Zn(II)-selective binding unit. With a Zn(II) affinity of 2.7 nM, ZnAF2 (4) was successfully used for detecting synaptically released Zn(II) in hippocampal slices [47, 48]. Further modifications with various chelating moieties furnished a series of indicators with a wide dynamic range for detecting Zn(II) from nM to mM concentrations [49]. The fluorescent dyes revealed intriguing concentrations differences of synaptically released Zn(II) in acute hippocampal slices [50]. In parallel,

Lippard and coworkers developed a large family of Zn(II)-responsive indicators, primarily aimed at unraveling the neurobiology of this metal ion. For example, the difluorofluorescein derivative ZP3 (5) was successfully utilized to image endogenous Zn(II) pools in hippocampal slices [51], whereas the cell-impermeant indicator ZP4 (6) proved to be suitable for imaging extracellular Zn(II) and Zn(II)-damaged neurons [52, 53]. A detailed review of this extensive body of work has been recently published [29].

Several efforts focused on developing ratiometric probes for the detection of Zn(II) in biological systems [28]. Originally described by Tsien and coworkers for the dynamic visualization of Ca(II)-fluxes [54], ratiometric probes undergo a shift of the excitation or emission maxima upon binding of the analyte. By taking the ratio of the emission intensity at two different wavelengths, fluctuations due to uneven dye distribution, cellular uptake, or instrument dependent factors are cancelled out. For example, the iminocoumarin based Zn(II) sensor, ZnIC (**7**), undergoes a red shift, from 543- 558 nM, associated with an enhanced intramolecular charge transfer up on zinc binding at physiological pH. With a Kd of 1.3 pM, the sensor was successfully used for the ratiometric detection of Zn(II) in cultured cells and in rat hippocampal slices [49].

The development of new imaging technologies typically requires also a tailored optimization of the indicator properties. With this goal in mind, Zn(II)-responsive indicators for applications in two-photon excitation microscopy [55, 56], near-infrared (NIR) fluorescence imaging [57-59] have been developed. Due to the increased penetration depth of the low-energy infrared excitation, these two fluorescence microscopy techniques are particularly attractive for imaging thick tissues or potentially for imaging whole animal studies. As illustrated with Figure 1.2, staining of rat

hippocampal slices with the Zn(II)-responsive two-photon indicator AZn2 (**8**) revealed a characteristic staining pattern of histochemically labile Zn(II) pools. The fluorescence staining was reversed by addition of the high affinity Zn(II)-chelator, TPEN (N,N,N',N'-tetrakis-(2-pyridylmethyl)-ethylenediamine) (Figure 1.2c), and a distinct increase in fluorescence intensity was observed upon stimulation with 50 mM KCl, suggesting the release of presynaptic Zn(II) stores (Figure 1.2e).

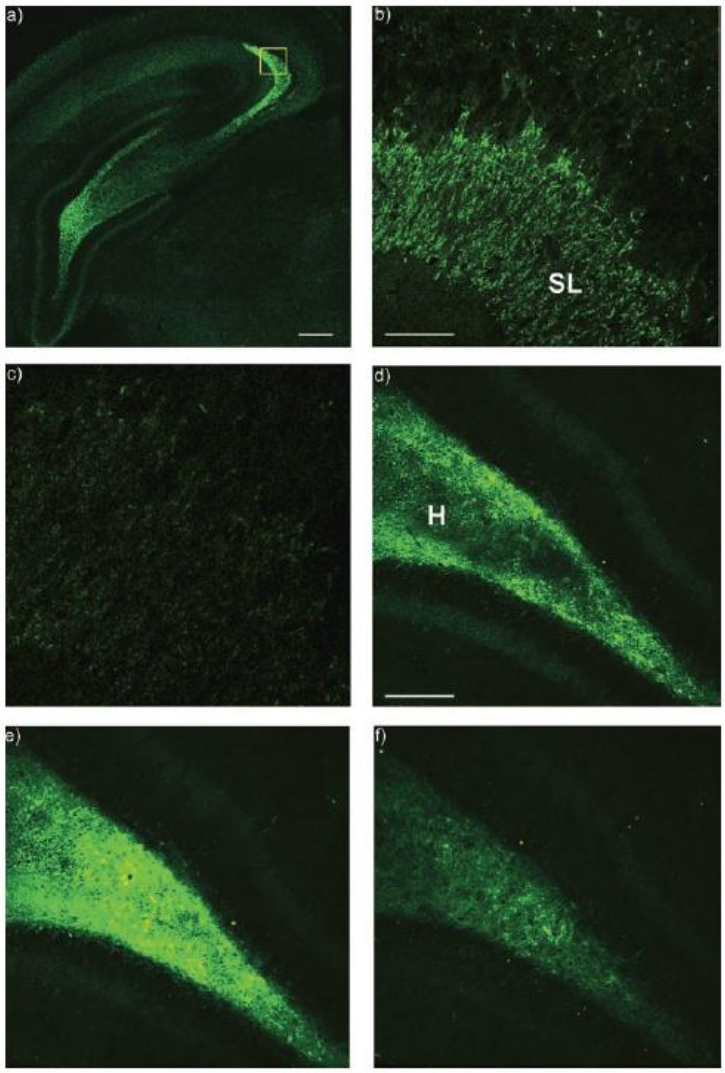

Figure 1.2: Two-photon excitation microscopy (TPM) images of a rat hippocampal slice stained with 10 μM AZn2 (**8**). a) At a depth of ca. 120 mm with magnification 10x. Scale bar: 300 mm. b,c) Magnification at 100x in the stratum lucidum (SL) of CA3 regions (yellow box in (a)) at a depth of ca. 100 mm before (b) and after (c) addition of 200 μM TPEN to the imaging solution. Scale bar: 150 mm. d–f) TPM images in the hilus (H) of dentate gyrus (DG) regions at a depth of ca. 100 mm before (d) and after (e) addition of 50 μM KCl to the buffer solution. Scale bar: 300 mm. f) After addition of 200 μM TPEN to (e). The TPEF images were collected at 500–620 nm with excitation at 780 nm using a femtosecond pulsed laser. Reproduced from ref [21].

To this point, only few biologically oriented studies have taken advantage of the capabilities of these newly fluorescent dyes. While the histochemical methods were

limited to demonstrating labile Zn(II) in fixed specimens, the inherently high detection sensitivity of fluorescence microscopy combined with the broad range of thermodynamic affinities, Zn(II)-responsive fluorescent indicators harbor great potential for visualizing dynamic Zn(II) fluxes with sub-cellular resolution in live cells, and thus for elucidating important questions regarding the complex mechanisms of cellular zinc homeostasis.

In contrast to the rich literature on Zn(II)-selective fluorescent probes, there are only a few reports on the detection of biological copper, despite the fact that it is equally important as zinc within the cellular metallome. The fluorescence-based detection of redox-active metals, such as copper, is particularly challenging due to competing metal-initiated fluorescence quenching pathways. The adverse fluorescence quenching can be minimized with a rigid fluorophore-ligand architecture, which electronically decouples the metal cation from the fluorescence emitter [20, 60]. Following this concept, fluorescent probes for the detection of Cu(I) in cultured cells have been described [61, 62]. Although the fluorescence detection of copper in a biological environment presently still poses significant challenges, these initial successes clearly demonstrate its feasibility. Given that most biological laboratories are equipped with fluorescence microscopes, synthetic fluorescent probes remain particularly attractive for routine imaging of labile metal pools and will remain an active research area for developing materials with further improved selectivity and sensitivity.

1.4 Synchrotron Radiation X-ray Fluorescence (SXRF) Microscopy

X-ray fluorescence (XRF) based imaging techniques rank currently among the most sensitive imaging modalities for detecting trace elements in biological samples with submicron resolution [7, 63-66]. These methods rely on the direct excitation of the core-shell electrons of atoms, which subsequently relax with emission of photons. Because the emitted X-ray energy depends on the nuclear charge, the elemental composition of a sample can be precisely identified and quantified. Depending on the mode of excitation, XRF analytical techniques can be categorized into three different classes: electron beam, proton beam, and X-ray (photon) beam methods, each of which offers its own set of advantages and disadvantages. This chapter will focus on the X-ray beam based method, synchrotron radiation X-ray fluorescence (SXRF) microscopy, because it is extensively applied throughout the scope of the work presented in this thesis. After a brief description of the physical principles and instrumentation, the subsequent sections offer a brief overview of the broad spectrum of biological questions that have been addressed with SXRF microscopy.

Physical Background and Instrumentation

Synchrotron X-ray fluorescence microprobes (SXRF) rely on spatially coherent high brilliance X-rays as the excitation source. SXRF uses the detection of the emitted X-rays to achieve spatially resolved 2D elemental distribution maps. The individual components of an SXRF microscope are illustrated in Figure 1.3.

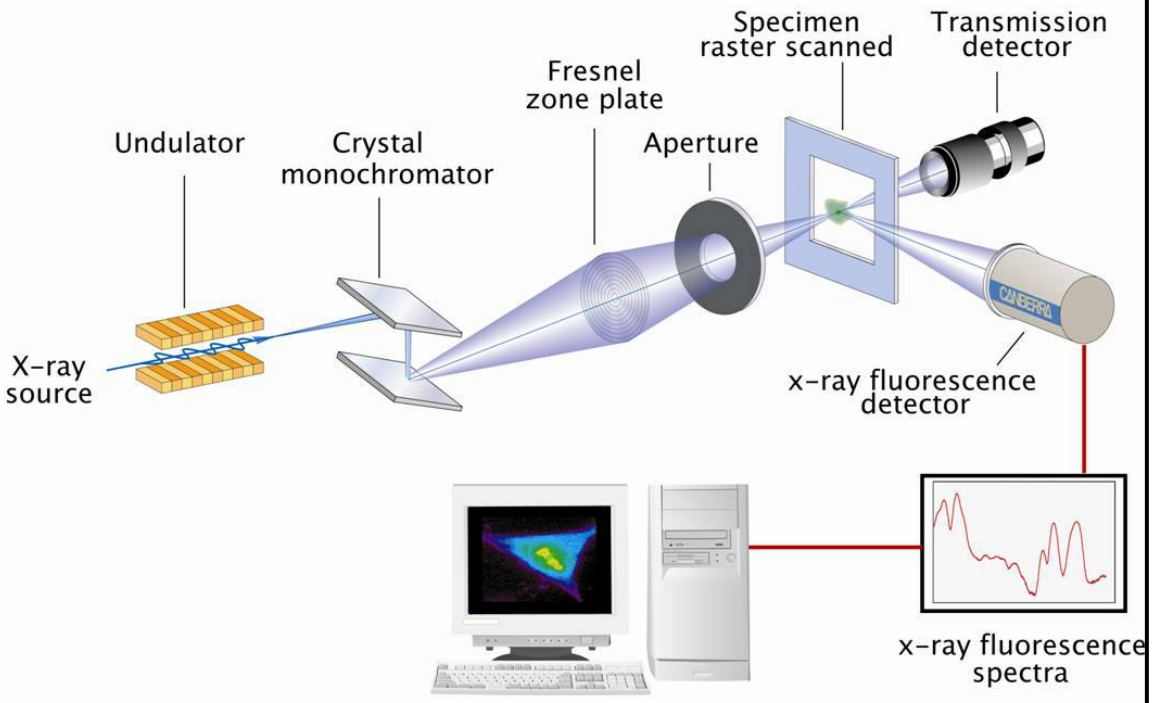

Figure 1.3: Schematic diagram illustrating the components of a synchrotron radiation X-ray fluorescence (SXRF) microscope. A crystal monochromator is used to select the energy of the X-ray beam, which is focused with a Fresnel zone plate on the specimen. The emitted X-rays are collected with an energy dispersive detector, thus allowing for simultaneous multi-element analysis. Raster-scanning across the specimen area then yields quantitative elemental maps, as illustrated on the computer monitor. The purpose of the transmission detector is to help orient the sample on the scanning stage . Reproduced from reference [64].

The transition energies associated with electronic relaxation are equal to the difference between the inner and outer shell binding energies, which are specific for individual elements (Figure 1.4). X-rays are detected using energy-dispersive detectors offering detection limits ranging from 5×10^{-20} – 3.9×10^{-19} mol/µm^2, corresponding to a few thousand atoms within an irradiated spot. The number of X-ray photons emitted scales directly as a function of atomic abundance, thus allowing for a straightforward determination of individual element quantities (Figure 1.4).

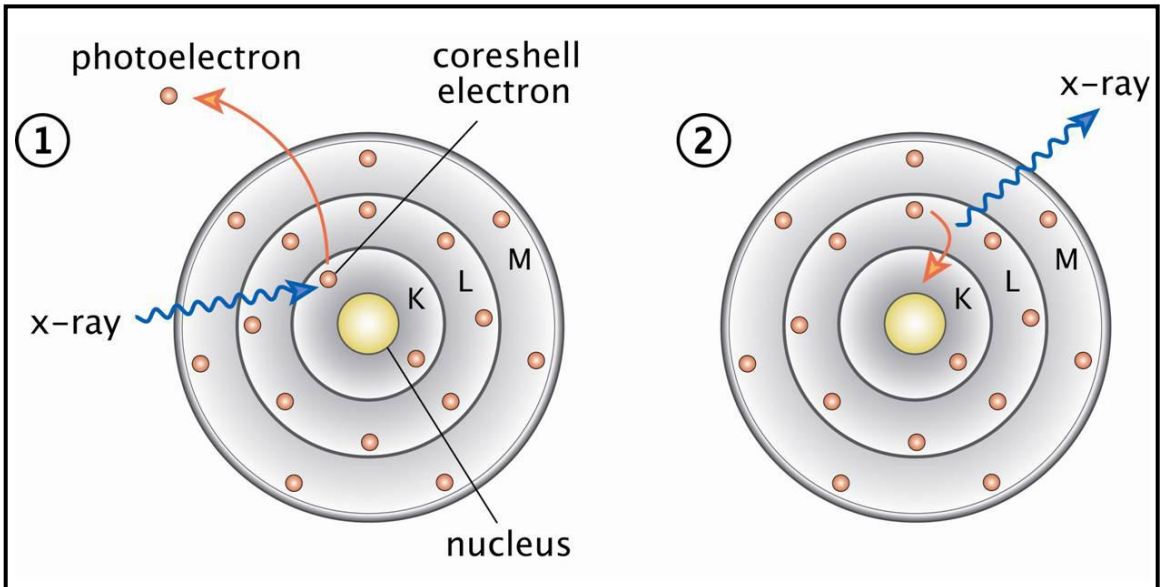

Figure 1.4: Bohr atom model illustrating the basic principles of X-ray fluorescence. **(a)** X-ray excitation leads to ejection of a core-shell electron from the atom. **(b)** The generated vacancy is filled through a higher-shell electron, a process that results in the emission of a photon whose energy is equal to the difference in binding energies of the two shells involved in the transition. Reproduced from reference [64].

As illustrated with the analysis of a NIH 3T3 mouse fibroblast cell (Figure 1.5), a single raster scan with an incident X-ray energy of 10 keV simultaneously produced quantitative maps with sub-cellular spatial resolution for selected biologically relevant elements.

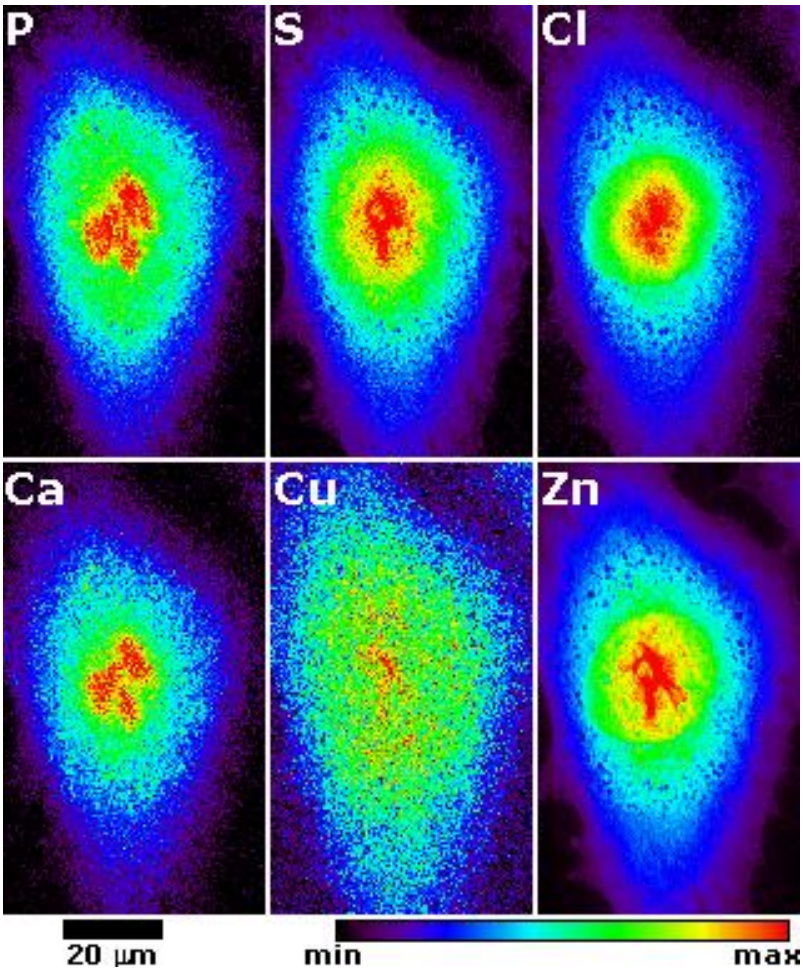

Figure 1.5: SXRF imaging of mouse fibroblast cells grown on electron microscopy (EM) silicon nitride (Si_3N_4) windows. Raster-scanned SXRF topographical maps for selected elements (excitation at 10 keV, pixel size 0.3 µM, integration time 1 sec/pixel).

Recent advances in X-ray optics permit beam focusing to 30-150 nm spots using Kirkpa-trick-Baez mirrors [67, 68], refractive lenses [69], or Fresnel zone plates [70], thus enabling the production of spatially highly resolved, 2D elemental distribution maps. By offering a penetration depth of up to 1000 µm and routine spatial resolutions down to 100 nm, synchrotron radiation induced X-ray imaging (SXRF) is especially useful for analyzing hydrated biological specimens [64]. Furthermore, by scanning the incident photon energy across the X-ray absorption (XAS) edge of the element(s) of interest,

information regarding the oxidation state and local coordination environment of an element can be obtained (microXANES) [71]. Given these features, X-ray microprobe methods have contributed to numerous research studies in geochemistry, cosmetic chemistry, environmental science, materials science, and more recently, in biology and medicine.

1.5 Overview of SXRF Applications in Biology

The following sub-sections highlight some of the significant contributions made by SXRF imaging studies towards understanding a number of severe diseases. The examples presented also serve to illuminate the fundamental significance of the roles played by copper and zinc in the onset and progression of these diseases.

Cancer

Angiogenesis is a physiological process that leads to formation of new blood vessels from existing vasculature. While angiogenesis is vital to normal growth and development, it plays a particularly critical role in tumor development [72]. Because tumor progression is limited without adequate supply of oxygen and nutrients through the host vascular system, the suppression of angiogenesis has evolved as an important target for cancer treatment strategies. The depletion of copper has been shown to inhibit angiogenesis in a broad range of cancer types; however, the underlying reasons for the copper sensitivity remain elusive [73]. To gain insights into the role of copper in angiogenesis, Finney et al. utilized X-ray fluorescence microscopy to image cellular copper stores in microvascular endothelial cells. These experiments revealed a massive

re-localization of copper from intracellular compartments to the tips of cell filopodia and across the plasma membrane [74].

Breast cancer is the most common form of cancer in Western women [75]. Farquharson and co-workers applied SXRF to investigate the quantity and spatial distribution of trace metals in breast tissue slices with primary invasive ductal carcinoma [76-78]. The studies revealed an increase in all measured metal concentrations, particular for Zn and Cu, in the tumor areas of the studied samples. Further analysis of the X-ray absorption near edge structure (XANES) indicated that Cu is present as a mixture of its monovalent and divalent oxidation states, for both normal and cancerous tissue [78]. Interestingly, the data suggested that the cancerous tissue contains a higher fraction of Cu(I) compared with normal tissue. Additionally, SXRF analysis of the metal distributions revealed a similar pattern for Ca, Cu, P, S, and Zn while Fe maintained a uniquely different distribution [77]. Similar results were obtained in two independent studies, which used SXRF to elucidate quantitative metal distributions in breast carcinoma tissue samples [79, 80]. The results indicated also increased amounts of Ca, Cu, and Zn in areas of the cancer clusters and a different spatial distribution for Fe compared with Ca, Cu, and Zn. A combined X-ray fluorescence microtomography (XRFCT) and X-ray transmission microtomography (CT) system was implemented at the Brazilian Synchrotron Light Source (LNLS) and applied to investigate the spatial distribution of Zn, Cu, and Fe in breast cancer tissue samples [81-84]. Cylindrically shaped tissue samples with 1.5-2 mm thickness were scanned over 180° with a beam focused to 200 μm. Although tissue self-absorption prevented from obtaining

quantitative elemental information, tomographic reconstructions revealed the qualitative 3D distribution of Fe, Cu, and Zn.

Despite substantial efforts in screening and early detection, prostate cancer is still the most common, non-cutaneous human malignancy and is the second most lethal tumor among men [84]. The concentration of zinc in the human prostate tissue is higher compared to any other soft tissue in the body [85], and there is compelling evidence that altered prostate zinc homeostasis is an important factor in the development of prostate malignancy [86]. To investigate the potential causal effects of Zn in prostate cancer development and progression, SXRF was utilized to image the distribution of Zn in malignant tissue versus control samples [87]. The study revealed significantly lower amounts of Zn in cancerous compared with normal tissue and striking differences in the correlation of Zn and Ca densities, suggesting that Ca might play a significant role in the ability of the cell to accumulate Zn.

Neurodegenerative Diseases

The central nervous system (CNS) is comprised of the brain and spinal cord and functions as the body's information gatherer, storage center, and control system [88]. While the brain serves as the center for cognitive and motor functions, the spinal cord communicates messages from the body to the brain and vice versa. Although the brain accounts for only 2% of the total human body mass, it consumes 20% of the oxygen absorbed through respiration. Compared with other regions of the body, the brain contains also significantly higher concentrations of metal ions [16, 53]. It is therefore not

surprising that many neurological disorders are associated with a metal imbalance in the nervous system [4, 89]. While the accumulation of redox active transition metal ions is believed to induce oxidative stress through the generation of free radicals [90]; the relationship between metal ion imbalance and the pathology of neurological disorders remains largely elusive. Synchrotron radiation based imaging techniques offer new opportunities to visualize and quantify transition metal ions at the subcellular level, and thus may greatly help in unraveling the role of metal ions and their speciation in neurobiology [91].

Parkinson's disease (PD) is the second most common neurodegenerative disease affecting more than four million people [92, 93]. Entailing loss of motor and sensory functions as well as memory impairment, the pathological hallmark of this disorder is a pronounced reduction of dopaminergic neurons from the substantia nigra (SN) resulting in decreased dopamine production within the basal ganglia [93]. While there is contradicting evidence that direct occupational exposures to metals poses a risk factor for PD [94], several studies have shown alterations in Cu and Zn homeostasis and accumulation of Fe within the SN [95, 96]. In an effort to unravel details of altered metal homeostasis in PD, a number of investigations have applied SXRF imaging to quantitatively asses changes in the distribution of Fe, Cu, and Zn within Parkinson's disease models compared to control cases.

According to recent SXRF studies, transition metals other than Fe may also contribute to PD pathogenesis [97-100]. For example, abnormal accumulation of Cu and Se were found inside neurons of the SN of human brain tissue sections from PD patients

[98]. No differences in the speciation of copper between PD and control samples were found in a recent XANES microbeam study [100]. The data suggest that the bulk of copper inside SN neurons is coordinated in a tetrahedral environment in its divalent oxidation state. In a comparative study of SN from tissue representing PD, amyotrophic lateral sclerosis, and control cases, Chwieji et al. found that areas of high Zn content correlated with the location of the SN neuron bodies, while Br levels within the white matter of the SN were slightly elevated [99]. Multivariate cluster analysis of SXRF data confirmed significant differences in trace metal accumulation in SN of brain tissue from PD patients compared with either amyotrophic lateral sclerosis patients or a control group [99].

Alzheimer's disease (AD) is the most common form of senile dementia and affects approximately 26 million people worldwide [101]. AD manifests gradually with progressive and irreversible cognitive decline first experienced in the form of memory impairment at the early stage of the disease and a decline of motor and sensory functions at later stages. Concluding from postmortem AD brains, the pathology of AD progression is characterized by an accumulation of insoluble Aβ amyloid peptides (Aβ), neurofibrillary tangles, neuropil threads, and neuronal losses. An increasing body of literature indicates that Aβ amyloid formation is central to AD pathogenesis [102]. Furthermore, abnormal interactions of Aβ with neocortical metal ions, especially Zn, Cu, and Fe, might play an important role in amyloid formation and toxicity [103, 104].

The combination of different imaging modalities is particularly advantageous for simultaneously identifying the location and analyzing the elemental composition of AD

plaques and brain tissues. For this purpose, Miller et al. integrated an epifluorescence module within a SXRF microprobe beamline, and directly identified metal accumulation within Thioflavin-S-stained AD plaques with a precision of 2-5 mm [105]. To circumvent histochemical staining of the specimens, a process that might introduce artifacts, synchrotron Fourier transform infrared micro-spectroscopy (FTIRM) was combined with an SXRF microprobe [106]. Amyloid plaques are associated with an elevated b-sheet content, which can be identified by FTIRM on basis of the characteristic amide absorbance around 1630 cm^{-1} [107]. The study demonstrated a strong correlation between an elevated b-sheet content in AD plaques and the accumulation of Cu and Zn in "hot spots", thus strongly supporting the association of metal ions with amyloid formation in AD.

The disruption of cellular copper trafficking is at the center of both Menkes and Wilson's disease [108], underscoring the importance of maintaining the delicate homeostatic balance of copper. On the one hand, copper is essential to a multitude of cellular processes, including mitochondrial respiration, antioxidant defense, neurotransmitter synthesis, connective tissue formation, pigmentation, peptide amidation and iron metabolism, on the other hand, copper excess may facilitate the production of reactive oxygen species through Fenton type reactions [109]. The two copper transporting ATPases, ATP7a and ATP7b, are key elements in controlling the overall copper balance in the human body. Mutations in ATP7A or ATP7B gene disrupt this balance, resulting in copper deficiency as in the case of Menkes disease, or copper overload as in Wilson's disease [110].

In an effort to elucidate the speciation and distribution of tetrathiomolybdate (TTM), a promising copper chelator for treating Wilson's disease [111, 112], Zhang et al. used a combination of X-ray absorption spectroscopy and SXRF imaging to analyze the liver and kidney of a TTM-treated animal model of Wilson's disease [113]. The XAS spectra of TTM-treated rat liver and kidney indicated the presence of three- and four-coordinate Cu(I)-S species. In kidney, most copper appeared to be present as multinuclear Cu-Mo complexes, whereas the liver samples pointed also towards the presence of non-clusterbound Cu. A pronounced accumulation of Cu was observed in the cortex of the kidney for TTM treated rats with a high degree of correlation between Mo and Cu. The results are consistent with a mechanism in which copper is bound by TTM in the liver, and then in part mobilized to the kidney.

1.6 Thesis Objective

The primary objective of this work is to elucidate novel information regarding intracellular trace metals by predominantly using a combination of high resolution imaging modalities. Specifically, the unique opportunities offered by metal-ion selective fluorescence probes are combined with those of SXRF microscopy to illuminate new details regarding the uptake, storage, distributions, and functions of both copper and zinc in mammalian cells. This combination of methods is expected to produce high resolution, quantitative data that shed new light on the mechanistic aspects of numerous metal-ion associated diseases and ultimately contribute to their treatment and/or prevention.

1.7 Literature Cited

1. Li, Y. F., Chen, C. Y., Qu, Y., Gao, Y. X., Li, B., Zhao, Y. L., et al. (2008) Metallomics, elementomics, and analytical techniques. *Pure Appl. Chem.* **80**, 2577-2594.

2. Ascone, I., & Strange, R. (2009) Biological X-ray absorption spectroscopy and metalloproteomics. *J. Synchrot. Radiat.* **16**, 413-421.

3. Finney, L. A., & O'halloran, T. V. (2003) Transition metal speciation in the cell: Insights from the chemistry of metal ion receptors. *Science* **300**, 931-936.

4. Bush, A. I. (2000) Metals and neuroscience. *Curr. Opin. Chem. Biol.* **4**, 184-191.

5. Perls, M. (1867). *Virchows Archiv Path Anat* **39**, 42-48.

6. Mcrae, R., Lai, B., & Fahrni, C. J. (2010) Copper redistribution in atox1-deficient mouse fibroblast cells. *J. Biol. Inorg. Chem.* **15**, 99-105.

7. Lobinski, R., Moulin, C., & Ortega, R. (2006) Imaging and speciation of trace elements in biological environment. *Biochimie* **88**, 1591-1604.

8. Twining, B. S., Baines, S. B., Vogt, S., & De Jonge, M. D. (2008) Exploring ocean biogeochemistry by single-cell microprobe analysis of protist elemental composition. *J. Eukaryot. Microbiol.* **55**, 151-162.

9. Cheon, J., & Lee, J. H. (2008) Synergistically integrated nanoparticles as multimodal probes for nanobiotechnology. *Accounts Chem. Res.* **41**, 1630-1640.

10. Barthe, N., Chatti, K., Coulon, P., Maitrejean, S., & Basse-Cathalinat, B. (2004) Recent technologic developments on high-resolution beta imaging systems for quantitative autoradiography and double labeling applications. *Nucl. Instrum. Methods Phys. Res. Sect. A-Accel. Spectrom. Dect. Assoc. Equip.* **527**, 41-45.

11. Goldschmidt, J., Zuschratter, W., & Scheich, H. (2004) High-resolution mapping of neuronal activity by thallium autometallography. *Neuroimage* **23**, 638-647.

12. Powell, R. D., Pettay, J. D., Powell, W. C., Roche, P. C., Grogan, T. M., Hainfeld, J. F., et al. (2007) Metallographic in situ hybridization. *Hum. Pathol.* **38**, 1145-1159.

13. Giepmans, B. N. G., Adams, S. R., Ellisman, M. H., & Tsien, R. Y. (2006) Review - the fluorescent toolbox for assessing protein location and function. *Science* **312**, 217-224.

14. Pearse, A. G. E. (1980). *Histochemistry. Theoretical and applied*. Edinburgh.

15. Yanagida, T., & Ishii, Y. (2009). *Single molecule dynamics in life science*. Weinheim.

16. Que, E. L., Domaille, D. W., & Chang, C. J. (2008) Metals in neurobiology: Probing their chemistry and biology with molecular imaging. *Chem. Rev.* **108**, 1517-1549.

17. Domaille, D. W., Que, E. L., & Chang, C. J. (2008) Synthetic fluorescent sensors for studying the cell biology of metals. *Nat. Chem. Biol.* **4**, 168-175.

18. Desilva, A. P., Gunaratne, H. Q. N., Gunnlaugsson, T., Huxley, A. J. M., Mccoy, C. P., Rademacher, J. T., et al. (1997) Signaling recognition events with fluorescent sensors and switches. *Chem. Rev.* **97**, 1515-1566.

19. Valeur, B., & Leray, I. (2000) Design principles of fluorescent molecular sensors for cation recognition. *Coord. Chem. Rev.* **205**, 3-40.

20. Rurack, K. (2001) Flipping the light switch 'on' - the design of sensor molecules that show cation-induced fluorescence enhancement with heavy and transition metal ions. *Spectroc. Acta Pt. A-Molec. Biomolec. Spectr.* **57**, 2161-2195.

21. Kim, H. M., Seo, M. S., An, M. J., Hong, J. H., Tian, Y. S., Choi, J. H., et al. (2008) Two-photon fluorescent probes for intracellular free zinc ions in living tissue. *Angew. Chem.-Int. Edit.* **47**, 5167-5170.

22. Kimura, E., & Aoki, S. (2001) Chemistry of zinc(ii) fluorophore sensors. *Biometals* **14**, 191-204.

23. Kimura, E., & Koike, T. (1998) Recent development of zinc-fluorophores. *Chem. Soc. Rev.* **27**, 179-184.

24. Jiang, P. J., & Guo, Z. J. (2004) Fluorescent detection of zinc in biological systems: Recent development on the design of chemosensors and biosensors. *Coord. Chem. Rev.* **248**, 205-229.

25. Kikuchi, K., Komatsu, K., & Nagano, T. (2004) Zinc sensing for cellular application. *Curr. Opin. Chem. Biol.* **8**, 182-191.

26. Lim, N. C., Freake, H. C., & Bruckner, C. (2005) Illuminating zinc in biological systems. *Chem.-Eur. J.* **11**, 38-49.

27. Thompson, R. B. (2005) Studying zinc biology with fluorescence: Ain't we got fun? *Curr. Opin. Chem. Biol.* **9**, 526-532.

28. Carol, P., Sreejith, S., & Ajayaghosh, A. (2007) Ratiometric and near-infrared molecular probes for the detection and imaging of zinc ions. *Chem.-Asian J.* **2**, 338-348.

29. Nolan, E. M., & Lippard, S. J. (2009) Small-molecule fluorescent sensors for investigating zinc metalloneurochemistry. *Accounts Chem. Res.* **42**, 193-203.

30. Nolan, E. M., & Lippard, S. J. (2008) Tools and tactics for the optical detection of mercuric ion. *Chem. Rev.* **108**, 3443-3480.

31. Szerdahelyi, P., & Kasa, P. (1984) Histochemistry of zinc and copper. *Int.Rev.Cytol.* **89**, 1-33.

32. Mahanand, D., & Houck, J. C. (1968) Fluorometric determination of zinc in biologic fluids. *Clin. Chem.* **14**, 6-&.

33. Watanabe, S., Frantz, W., & Trottier, D. (1963) Fluorescence of magnesium-, calcium-, and zinc-8-quinolinol complexes. *Anal. Biochem.* **5**, 345-&.

34. Hahnvond.H, & Fiedler, H. (1970) Histochemical demonstration of histidine by diazonium-1-h-tetrazole. *Acta Histochem.* **38**, 263-&.

35. Toroptse.Iv, & Eshchenk.Va (1970) Identity of zinc-containing and insulin-containing granules in cells of islets of langerhans. **69**, 461-&.

36. Toroptse.Iv, & Eshchenk.Va (1971) Histochemical detection of zinc by means of sulfarsazene. **72**, 1097-&.

37. Toroptse.Iv, & Eshchenk.Va (1971) Distribution of zinc in islets of langerhans of healthy and diabetic animals receiving tolbutamide. **72**, 968-&.

38. Eshchenko, V. A. (1978). *Tsitologiya* **55**, 27.

39. Toroptsev, I. V., & Eshchenko, V. A. (1982) Investigation of toxic chelant action on the hippocamp in the animals. **45**, 82-84.

40. Frederickson, C. J. (1989) Neurobiology of zinc and zinc-containing neurons. *Int. Rev. Neurobiol.* **31**, 145-238.

41. Frederickson, C. J., Kasarskis, E. J., Ringo, D., & Frederickson, R. E. (1987) A quinoline fluorescence method for visualizing and assaying the histochemically reactive zinc (bouton zinc) in the brain. *J. Neurosci. Methods* **20**, 91-103.

42. Mahadevan, I. B., Kimber, M. C., Lincoln, S. F., Tiekink, E. R. T., Ward, A. D., Betts, W. H., et al. (1996) The synthesis of zinquin ester and zinquin acid, zinc(ii)-specific fluorescing agents for use in the study of biological zinc(ii). *Aust. J. Chem.* **49**, 561-568.

43. Coyle, P., Zalewski, P. D., Philcox, J. C., Forbes, I. J., Ward, A. D., Lincoln, S. F., et al. (1994) Measurement of zinc in hepatocytes by using a fluorescent-probe, zinquin - relationship to metallothionein and intracellular zinc. *Biochem. J.* **303**, 781-786.

44. Zalewski, P. D., Millard, S. H., Forbes, I. J., Kapaniris, O., Slavotinek, A., Betts, W. H., et al. (1994) Video image-analysis of labile zinc in viable pancreatic-islet cells using a specific fluorescent-probe for zinc. *J. Histochem. Cytochem.* **42**, 877-884.

45. Zalewski, P. D., Forbes, I. J., & Betts, W. H. (1993) Correlation of apoptosis with change in intracellular labile zn(ii) using zinquin [(2-methyl-8-p-toluenesulphonamido-6-quinolyloxy)acetic acid], a new specific fluorescent-probe for zn(ii). *Biochem. J.* **296**, 403-408.

46. Wellenreuther, G., Cianci, M., Tucoulou, R., Meyer-Klaucke, W., & Haase, H. (2009) The ligand environment of zinc stored in vesicles. *Biochem. Biophys. Res. Commun.* **380**, 198-203.

47. Hirano, T., Kikuchi, K., Urano, Y., Higuchi, T., & Nagano, T. (2000) Highly zinc-selective fluorescent sensor molecules suitable for biological applications. *J. Am. Chem. Soc.* **122**, 12399-12400.

48. Hirano, T., Kikuchi, K., Urano, Y., & Nagano, T. (2002) Improvement and biological applications of fluorescent probes for zinc, znafs. *J. Am. Chem. Soc.* **124**, 6555-6562.

49. Komatsu, K., Urano, Y., Kojima, H., & Nagano, T. (2007) Development of an iminocoumarin-based zinc sensor suitable for ratiometric fluorescence imaging of neuronal zinc. *J. Am. Chem. Soc.* **129**, 13447-13454.

50. Komatsu, K., Kikuchi, K., Kojima, H., Urano, Y., & Nagano, T. (2005) Selective zinc sensor molecules with various affinities for zn2+, revealing dynamics and regional distribution of synaptically released zn2+ in hippocampal slices. *J. Am. Chem. Soc.* **127**, 10197-10204.

51. Chang, C. J., Nolan, E. M., Jaworski, J., Burdette, S. C., Sheng, M., & Lippard, S. J. (2004) Bright fluorescent chemosensor platforms for imaging endogenous pools of neuronal zinc. *Chem. Biol.* **11**, 203-210.

52. Frederickson, C. J., Burdette, S. C., Sensi, S. L., Weiss, J. H., Yin, H. Z., Balaji, R. V., et al. (2004) Method for identifying neuronal cells suffering zinc toxicity by use of a novel fluorescent sensor. *J. Neurosci. Methods* **139**, 79-89.

53. Burdette, S. C., Frederickson, C. J., Bu, W. M., & Lippard, S. J. (2003) Zp4, an improved neuronal zn2+ sensor of the zinpyr family. *J. Am. Chem. Soc.* **125**, 1778-1787.

54. Grynkiewicz, G., Poenie, M., & Tsien, R. Y. (1985) A new generation of ca-2+ indicators with greatly improved fluorescence properties. *J. Biol. Chem.* **260**, 3440-3450.

55. Kim, B. E., Nevitt, T., & Thiele, D. J. (2008) Mechanisms for copper acquisition, distribution and regulation. *Nat. Chem. Biol.* **4**, 176-185.

56. Sumalekshmy, S., Henary, M. M., Siegel, N., Lawson, P. V., Wu, Y., Schmidt, K., et al. (2007) Design of emission ratiometric metal-ion sensors with enhanced two-photon cross section and brightness. *J. Am. Chem. Soc.* **129**, 11888-+.

57. Tang, B., Huang, H., Xu, K. H., Tong, L. L., Yang, G. W., Liu, X., et al. (2006) Highly sensitive and selective near-infrared fluorescent probe for zinc and its application to macrophage cells. *Chem. Commun.*, 3609-3611.

58. Kiyose, K., Kojima, H., Urano, Y., & Nagano, T. (2006) Development of a ratiometric fluorescent zinc ion probe in near-infrared region, based on tricarbocyanine chromophore. *J. Am. Chem. Soc.* **128**, 6548-6549.

59. Atilgan, S., Ozdemir, T., & Akkaya, E. U. (2008) A sensitive and selective ratiometric near ir fluorescent probe for zinc ions based on the distyryl-bodipy fluorophore. *Org. Lett.* **10**, 4065-4067.

60. Rurack, K., & Resch-Genger, U. (2002) Rigidization, preorientation and electronic decoupling - the 'magic triangle' for the design of highly efficient fluorescent sensors and switches. *Chem. Soc. Rev.* **31**, 116-127.

61. Yang, L. C., Mcrae, R., Henary, M. M., Patel, R., Lai, B., Vogt, S., et al. (2005) Imaging of the intracellular topography of copper with a fluorescent sensor and by synchrotron X-ray fluorescence microscopy. *Proc. Natl. Acad. Sci. U. S. A.* **102**, 11179-11184.

62. Zeng, L., Miller, E. W., Pralle, A., Isacoff, E. Y., & Chang, C. J. (2006) A selective turn-on fluorescent sensor for imaging copper in living cells. *J. Am. Chem. Soc.* **128**, 10-11.

63. Ralle, M., & Lutsenko, S. (2009) Quantitative imaging of metals in tissues. *Biometals* **22**, 197-205.

64. Fahrni, C. J. (2007) Biological applications of X-ray fluorescence microscopy: Exploring the subcellular topography and speciation of transition metals. *Curr. Opin. Chem. Biol.* **11**, 121-127.

65. Paunesku, T., Vogt, S., Maser, J., Lai, B., & Woloschak, G. (2006) X-ray fluorescence microprobe imaging in biology and medicine. *J. Cell. Biochem.* **99**, 1489-1502.

66. Ortega, R., Deves, G., & Carmona, A. (2009) Bio-metals imaging and speciation in cells using proton and synchrotron radiation X-ray microspectroscopy. *J. R. Soc. Interface* **6**, S649-S658.

67. Matsuyama, S., Mimura, H., Katagishi, K., Yumoto, H., Handa, S., Fujii, M., et al. (2008) Trace element mapping using a high-resolution scanning X-ray fluorescence microscope equipped with a kirkpatrick-baez mirror system. *Surf. Interface Anal.* **40**, 1042-1045.

68. Matsuyama, S., Mimura, H., Yumoto, H., Hara, H., Yamamura, K., Sano, Y., et al. (2006) Development of mirror manipulator for hard-X-ray nanofocusing at sub-50-nm level. *Rev. Sci. Instrum.* **77**, 5.

69. Snigirev, A., & Snigireva, I. (2008) High energy X-ray micro-optics. *C. R. Phys.* **9**, 507-516.

70. Di Fabrizio, E., Romanato, F., Gentili, M., Cabrini, S., Kaulich, B., Susini, J., et al. (1999) High-efficiency multilevel zone plates for kev X-rays. *Nature* **401**, 895-898.

71. Bacquart, T., Deves, G., Carmona, A., Tucoulou, R., Bohic, S., & Ortega, R. (2007) Subcellular speciation analysis of trace element oxidation states using synchrotron radiation micro-X-ray absorption near-edge structure. *Anal. Chem.* **79**, 7353-7359.

72. Bergers, G., & Benjamin, L. E. (2003) Tumorigenesis and the angiogenic switch. *Nat. Rev. Cancer* **3**, 401-410.

73. Finney, L., Vogt, S., Fukai, T., & Glesne, D. (2009) Copper and angiogenesis: Unravelling a relationship key to cancer progression. *Clin. Exp. Pharmacol. Physiol.* **36**, 88-94.

74. Finney, L., Mandava, S., Ursos, L., Zhang, W., Rodi, D., Vogt, S., et al. (2007) X-ray fluorescence microscopy reveals large-scale relocalization and extracellular translocation of cellular copper during angiogenesis. *Proc. Natl. Acad. Sci. U. S. A.* **104**, 2247-2252.

75. Weigelt, B., Peterse, J. L., & Van't Veer, L. J. (2005) Breast cancer metastasis: Markers and models. *Nat. Rev. Cancer* **5**, 591-602.

76. Geraki, K., Farquharson, M. J., & Bradley, D. A. (2004) X-ray fluorescence and energy dispersive X-ray diffraction for the quantification of elemental concentrations in breast tissue. *Phys. Med. Biol.* **49**, 99-110.

77. Farquharson, M. J., Geraki, K., Falkenberg, G., Leek, R., & Harris, A. (2007) The localisation and micro-mapping of copper and other trace elements in breast tumours using a synchrotron micro-xrf system. *Appl. Radiat. Isot.* **65**, 183-188.

78. Farquharson, M. J., Al-Ebraheem, A., Falkenberg, G., Leek, R., Harris, A. L., & Bradley, D. A. (2008) The distribution of trace elements ca, fe, cu and zn and the determination of copper oxidation state in breast tumour tissue using mu srxrf and mu xanes. *Phys. Med. Biol.* **53**, 3023-3037.

79. Geraki, K., Farquharson, M. J., & Bradley, D. A. (2002) Concentrations of fe, cu and zn in breast tissue: A synchrotron xrf study. *Phys. Med. Biol.* **47**, 2327-2339.

80. Geraki, K., Farquharson, M. J., Bradley, D. A., Gundogdu, O., & Falkenberg, G. (2008) The localisation of biologically important metals in soft and calcified tissues using a synchrotron X-ray fluorescence technique. *X-ray Spectrom.* **37**, 12-20.

81. Pereira, G. R., Rocha, H. S., Anjos, M. J., Farias, P., Perez, C. A., & Lopes, R. T. (2008) Elemental distribution mapping on breast tissue samples. *Eur. J. Radiol.* **68**, S104-S108.

82. Pereira, G. R., Anjos, M. J., Rocha, H. S., Faria, P., Perez, C. A., & Lopes, R. T. (2007) Computed tomography and X-ray fluorescence ct of biological samples. *Nucl. Instrum. Methods Phys. Res. Sect. A-Accel. Spectrom. Dect. Assoc. Equip.* **580**, 951-954.

83. Pereira, G. R., Rocha, H. S., Anjos, M. J., Faria, P., Perez, C. A., & Lopes, R. T. (2007) X-ray fluorescence and X-ray transmission microtomography imaging system. *Nucl. Instrum. Methods Phys. Res. Sect. A-Accel. Spectrom. Dect. Assoc. Equip.* **581**, 128-132.

84. Rocha, H. S., Pereira, G. R., Anjos, M. J., Faria, P., Kellermann, G., Perez, C. A., et al. (2007) Diffraction enhanced imaging and X-ray fluorescence microtomography for analyzing biological samples. *X-ray Spectrom.* **36**, 247-253.

85. Kuhn, D. M., Arthur, R. E., Thomas, D. M., & Elferink, L. A. (1999) Tyrosine hydroxylase is inactivated by catechol-quinones and converted to a redox-cycling quinoprotein: Possible relevance to parkinson's disease. *J. Neurochem.* **73**, 1309-1317.

86. Costello, L. C., & Franklin, R. B. (2006) Tumor cell metabolism: The marriage of molecular genetics and proteomics with cellular intermediary metabolism; proceed with caution! *Mol. Cancer* **5**.

87. Ide-Ektessabi, A., Fujisawa, S., Sugimura, K., Kitamura, Y., & Gotoh, A. (2002) Quantitative analysis of zinc in prostate cancer tissues using synchrotron radiation microbeams. *X-ray Spectrom.* **31**, 7-11.

88. Nieuwenhuys, R., Voogd, J., & Van Huijzen, C. (2007). *The human central nervous system*. Berlin Heidelberg: Springer.

89. Zatta, P., Tognon, G., & Carampin, P. (2003) Melatonin prevents free radical formation due to the interaction between beta-amyloid peptides and metal ions [al(iii), zn(ii), cu(ii), mn(ii), fe(ii)]. *J. Pineal Res.* **35**, 98-103.

90. Valko, M., Morris, H., & Cronin, M. T. D. (2005) Metals, toxicity and oxidative stress. *Curr. Med. Chem.* **12**, 1161-1208.

91. Szczerbowska-Boruchowska, M., Lankosz, M., Ostachowicz, J., Adamek, D., Krygowska-Wajs, A., Tomik, B., et al. (2003) Application of synchrotron radiation for elemental microanalysis of human central nervous system tissue. *J. Phys. IV* **104**, 325-328.

92. Macdonald, B. K., Cockerell, O. C., Sander, J., & Shorvon, S. D. (2000) The incidence and lifetime prevalence of neurological disorders in a prospective community-based study in the uk. *Brain* **123**, 665-676.

93. Lotharius, J., & Brundin, P. (2002) Pathogenesis of parkinson's disease: Dopamine, vesicles and alpha-synuclein. *Nat. Rev. Neurosci.* **3**, 932-942.

94. Dick, F. D., De Palma, G., Ahmadi, A., Scott, N. W., Prescott, G. J., Bennett, J., et al. (2007) Environmental risk factors for parkinson's disease and parkinsonism: The geoparkinson study. *Occup. Environ. Med.* **64**, 666-672.

95. Dexter, D. T., Wells, F. R., Agid, F., Agid, Y., Lees, A. J., Jenner, P., et al. (1987) Increased nigral iron content in postmortem parkinsonian brain. *Lancet* **2**, 1219-1220.

96. Dexter, D. T., Carayon, A., Javoyagid, F., Agid, Y., Wells, F. R., Daniel, S. E., et al. (1991) Alterations in the levels of iron, ferritin and other trace-metals in parkinsons-disease and other neurodegenerative diseases affecting the basal ganglia. *Brain* **114**, 1953-1975.

97. Szczerbowska-Boruchowska, M., Lankosz, M., Ostachowicz, J., Adamek, D., Krygowska-Wajs, A., Tomik, B., et al. (2004) Topographic and quantitative microanalysis of human central nervous system tissue using synchrotron radiation. *X-ray Spectrom.* **33**, 3-11.

98. Szczerbowska-Boruchowska, M. (2008) X-ray fluorescence spectrometry, an analytical tool in neurochemical research. *X-ray Spectrom.* **37**, 21-31.

99. Szczerbowska-Boruchowska, M., Chwiej, J., Lankosz, M., Adamek, D., Wojcik, S., Krygowska-Wajs, A., et al. (2005) Intraneuronal investigations of organic components and trace elements with the use of synchrotron radiation. *X-ray Spectrom.* **34**, 514-520.

100. Chwiej, J., Adamek, D., Szczerbowska-Boruchowska, M., Krygowska-Wajs, A., Bohic, S., & Lankosz, M. (2008) Study of cu chemical state inside single neurons from

parkinson's disease and control substantia nigra using the micro-xanes technique. *J. Trace Elem. Med. Biol.* **22**, 183-188.

101.Ferri, C. P., Prince, M., Brayne, C., Brodaty, H., Fratiglioni, L., Ganguli, M., et al. (2005) Global prevalence of dementia: A delphi consensus study. *Lancet* **366**, 2112-2117.

102.Hardy, J., & Selkoe, D. J. (2002) Medicine - the amyloid hypothesis of alzheimer's disease: Progress and problems on the road to therapeutics. *Science* **297**, 353-356.

103.Bush, A. I., Masters, C. L., & Tanzi, R. E. (2003) Copper, beta-amyloid, and alzheimer's disease: Tapping a sensitive connection. *Proc. Natl. Acad. Sci. U. S. A.* **100**, 11193-11194.

104.Liu, G. J., Huang, W. D., Moir, R. D., Vanderburg, C. R., Lai, B., Peng, Z. C., et al. (2006) Metal exposure and alzheimer's pathogenesis. *J. Struct. Biol.* **155**, 45-51.

105.Miller, L. M., Smith, R. J., Ruppel, M. E., Ott, C. H., & Lanzirotti, A. (2005) Development and applications of an epifluorescence module for synchrotron X-ray fluorescence microprobe imaging. *Rev. Sci. Instrum.* **76**.

106.Miller, E. W., Zeng, L., Domaille, D. W., & Chang, C. J. (2006) Preparation and use of coppersensor-1, a synthetic fluorophore for live-cell copper imaging. *Nat. Protoc.* **1**, 824-827.

107.Byler, D. M., & Susi, H. (1986) Examination of the secondary structure of proteins by deconvolved ftir spectra. *Biopolymers* **25**, 469-487.

108.De Bie, P., Muller, P., Wijmenga, C., & Klomp, L. W. J. (2007) Molecular pathogenesis of wilson and menkes disease: Correlation of mutations with molecular defects and disease phenotypes. *J. Med. Genet.* **44**, 673-688.

109.Stohs, S. J., & Bagchi, D. (1995) Oxidative mechanisms in the toxicity of metal-ions. *Free Radic. Biol. Med.* **18**, 321-336.

110.Suzuki, M., & Gitlin, J. D. (1999) Intracellular localization of the menkes and wilson's disease proteins and their role in intracellular copper transport. *Pediatr. Int.* **41**, 436-442.

111.Brewer, G. J., Dick, R. D., Yuzbasiyangurkin, V., Tankanow, R., Young, A. B., & Kluin, K. J. (1991) Initial therapy of patients with wilsons-disease with tetrathiomolybdate. *Arch. Neurol.* **48**, 42-47.

112.Wiggelinkhuizen, M., Tilanus, M. E. C., Bollen, C. W., & Houwen, R. H. J. (2009) Systematic review: Clinical efficacy of chelator agents and zinc in the initial treatment of wilson disease. *Aliment. Pharmacol. Ther.* **29**, 947-958.

113. Zhang, L. M., Lichtmannegger, J., Summer, K. H., Webb, S., Pickering, I. J., & George, G. N. (2009) Tracing copper-thiomolybdate complexes in a prospective treatment for wilson's disease. *Biochemistry* **48**, 891-897.

CHAPTER 2
INVESTIGATING LABILE COPPER POOLS

2.1 Detecting Intracellular Kinetically Labile Copper

Copper is a trace element essential for the maintenance of human health. Often serving as an enzyme cofactor, copper is involved in numerous vital biological processes such as mitochondrial respiration, electron transfer, and detoxification of oxygen radicals [1]. However, copper must not accumulate to excessive intracellular levels given the ability of copper ions (Cu^{+}) to generate highly reactive hydroxyl radicals, which damage DNA, lipids, proteins, and other essential bio-molecules [2-4]. In order to achieve the proper intracellular balance of copper, nature has developed sophisticated homeostatic machinery for providing copper to essential enzymes, proteins, and intracellular locations, while simultaneously preventing its accumulation. A cell's essential need for copper regulation is indeed underscored by two inherited disorders of copper metabolism, Menkes' disease and Wilson's disease [5-7]. Furthermore, copper de-regulation has also been linked with the onset and progression of other serious neurodegenerative diseases including amyotrophic lateral sclerosis (ALS), Parkinson's, and Alzheimer's disease [8, 9]. Given the severe and often life-threatening nature of the aforementioned neurodegenerative diseases combined with a current lack of effective treatments, studies dedicated to elucidating details associated with copper homeostasis and dyshomeostasis at the cellular level would prove greatly beneficial.

Intracellular Regulation of Copper

Copper is regulated by a network of intracellular pathways comprised of trafficking proteins and molecules rich in sulfur atoms ideally suited for copper coordination. These copper chaperones are commonly characterized by a CXXC amino acid motif essential for copper acquisition and delivery [10]. Upon reduction to its monovalent oxidation state [11], copper enters the cell via a high affinity membrane permease, copper transporter 1 (hCtr1) [12-14] from which it is directed into copper trafficking pathways (Figure 2.1).

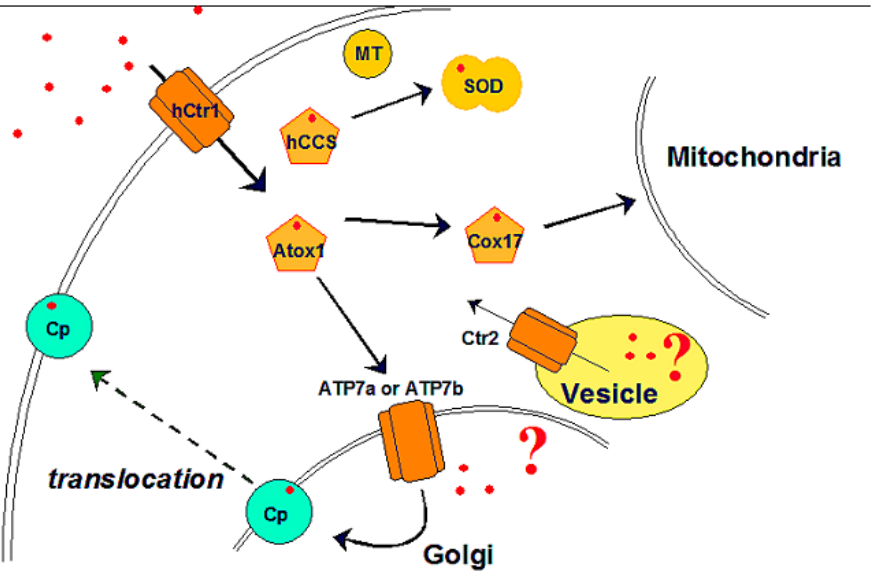

Figure 2.1: Copper trafficking in mammalian cells.

One pathway involves hCCS, the copper chaperone for superoxide dismustase (SOD) localized either in the cytoplasm or within the inner membrane space (IMS) of the mitochondria [15]. SOD is an essential enzyme that catalyzes the disproportionation of highly reactive superoxide (O_2^{2-}) radicals into peroxide (H_2O_2) and dioxygen (O_2) species

[16-18]. Defects in this pathway have been directly linked to a severe disease of the central nervous system, amyotrophic lateral sclerosis (ALS) [19]. Another pathway involves the incorporation of copper into cytochrome *c* oxidase (CcO), an enzyme required for cellular respiration and localized in the mitochdria [15],[20-22]. Metallation of CcO occurs within the mitochondria and is mediated by Sco1 and Cox11 metallochaperones upon their acquisition of copper from Cox17 [15],[20-22],[23]. In a third pathway the copper chaperone, Atox1, interacts with and delivers copper to either the Menkes' ATPase (ATP7a) or Wilson's ATPase (ATP7b) residing in the trans-Golgi network for the delivery of copper into the secretory pathway and ultimate incorporation into enzymes such as lysyl oxidase and ceruloplasmin [24-29]. As previously mentioned, defects in this pathway resulting from genetic mutations within the ATP7A or ATP7B gene directly foster the development of Menkes' disease or Wilson's disease, respectively [11],[30].

Labile Intracellular Copper

Although the thermodynamically estimated level of solvated copper ions in the cytoplasm lies below a single ion per cell [31], a significant fraction remains exchangeable with the extracellular environment. Evidence for the existence of kinetically labile copper pools was provided by studies, which showed surprisingly rapid uptake and release of radioactive copper, ^{64}Cu, from mammalian cells where copper increased 20-fold within an hour and decreased at a similar rate upon washing with metal-free media [32]. Fluorescent probes offer an effective and non-destructive opportunity to probe the intracellular behavior of kinetically exchangeable metal ions.

The goal of the present study was to investigate the applicability of a rationally designed fluorescent probe for probing the intracellular manner of Cu(I).

2.2 Optical Sensing of Monovalent Copper

Although monovalent copper typically acts as an effective fluorescence quencher, we successfully developed a Cu(I)-selective fluorescent sensor (CTAP-1) that undergoes a four-fold emission enhancement upon binding of Cu(I) under physiological conditions (Figure 2.2) [33].

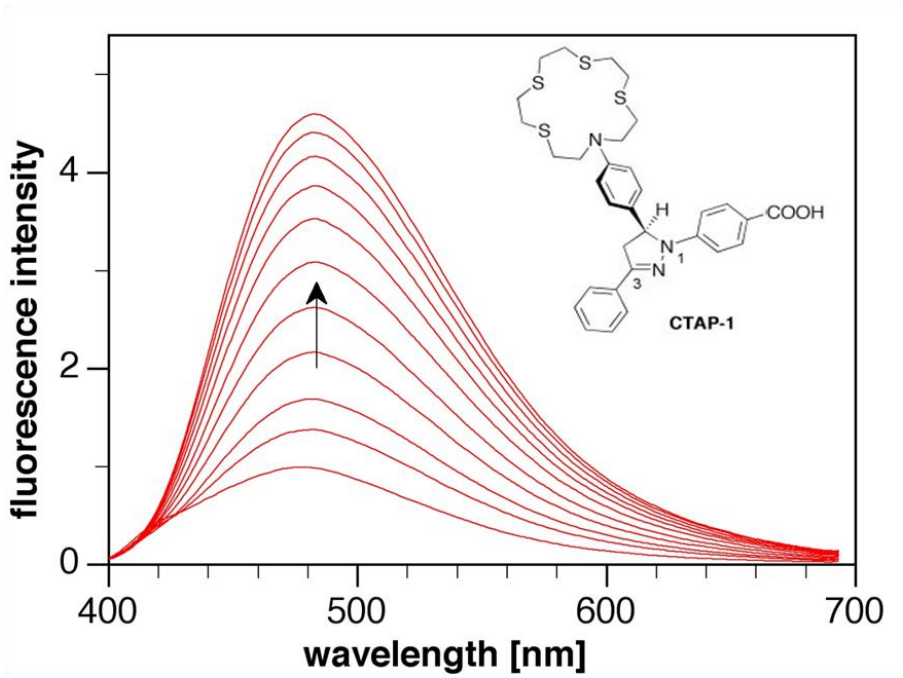

Figure 2.2: Fluorescence emission response of CTAP-1 as a function of added $Cu(CH_3CN)_4PF_6$ (5 µM ligand, 10 mM PIPES, pH 7.2). Data provided by Dr. Maged Henary and Dr. Liuchun Yang.

Additional experiments further revealed the fluorescence response of CTAP-1 is highly selective towards Cu(I) as the presence of other biologically relevant metal cations such as Mg(II), Ca(II), Fe(II), Fe(III), or Zn(II) (1mM) showed no obvious effect on the fluorescence emission (Figure 2.3) [33].

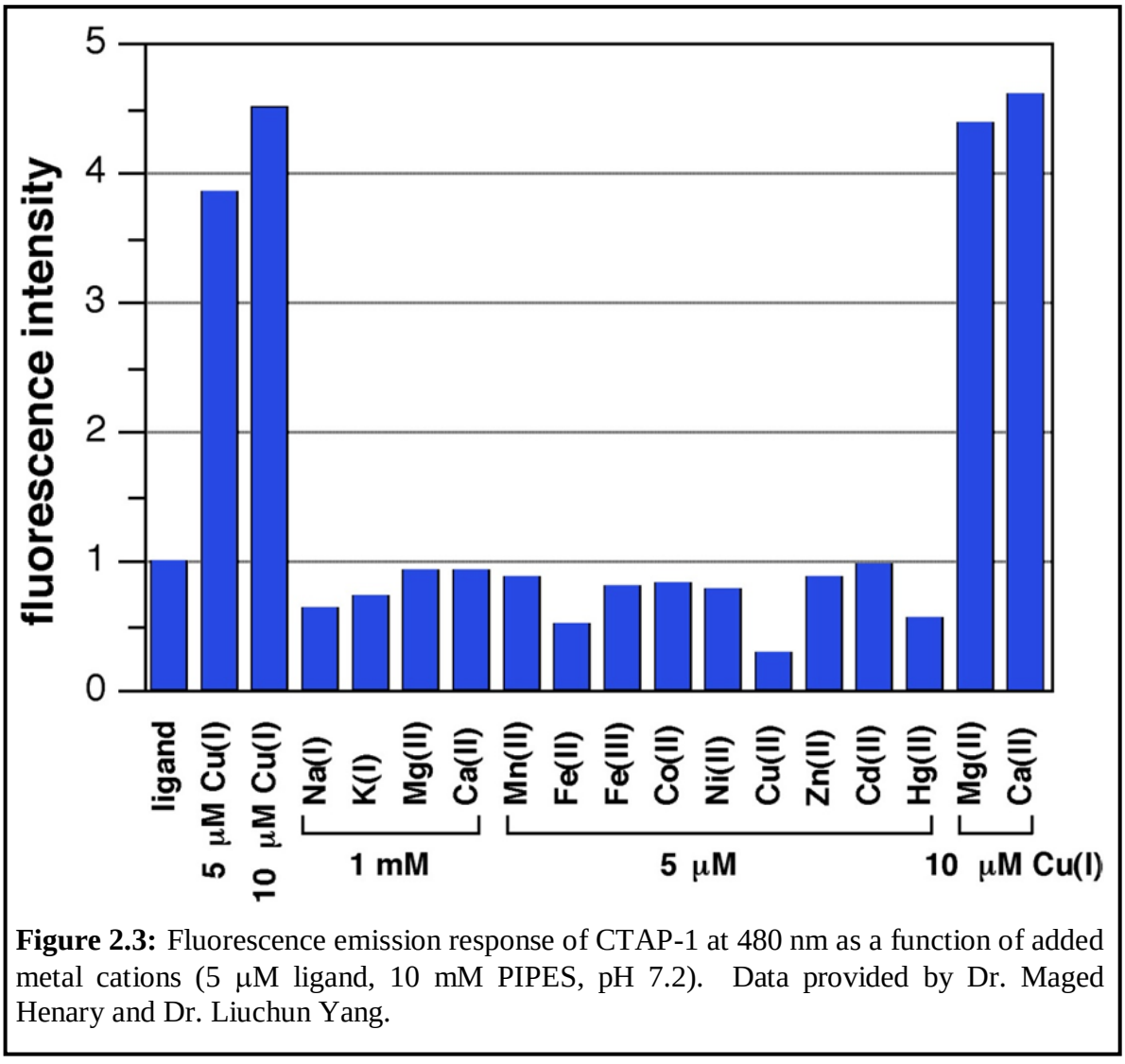

Figure 2.3: Fluorescence emission response of CTAP-1 at 480 nm as a function of added metal cations (5 μM ligand, 10 mM PIPES, pH 7.2). Data provided by Dr. Maged Henary and Dr. Liuchun Yang.

Moreover, the intracellular fluorescence response of CTAP-1 in cells cultured in growth media supplemented with 150 μM $CuCl_2$ for 12 h (Figure 2.4, lower) showed a 2 to 3-fold increase in intensity relative to basal conditions (Figure 2.4, upper) [33].

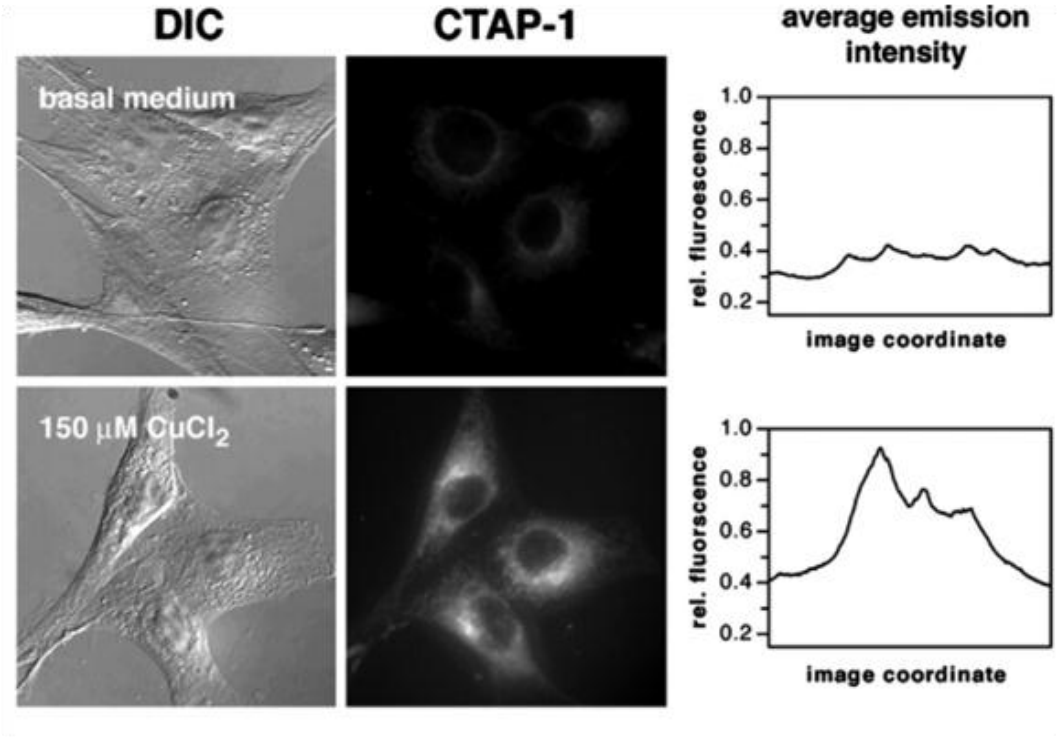

Figure 2.4: Fluorescence micrographs showing the intracellular staining pattern of 3t3 cells incubated with CTAP-1. (Left and Center) Influence of copper supplementation. (Upper) Cells were grown in basal medium. (Lower) Media supplemented with 150 μM CuCl2 for 12 h. (Right) The graphs represent the average intensity profile along the x-coordinate of the fluorescent micrographs.

Experiments designed to reverse the observed intracellular fluorescence enhancement of CTAP-1 in cells grown in copper-supplemented media were performed to help eliminate the possibility of artifacts contributing to the enhancement [34]. Prior to performing cellular experiments, the ability of a non-fluorescent pre-cursor to CTAP-1, 3,6-dithia-1,8-octanediol (DTO), was tested for its ability to reverse the fluorescence response of CTAP-1 to copper in cuvette-based assays (Figure 2.5). The results

suggested a reversal of CTAP-1 fluorescence to baseline levels upon addition of DTO in excessive amounts (Figure 2.5).

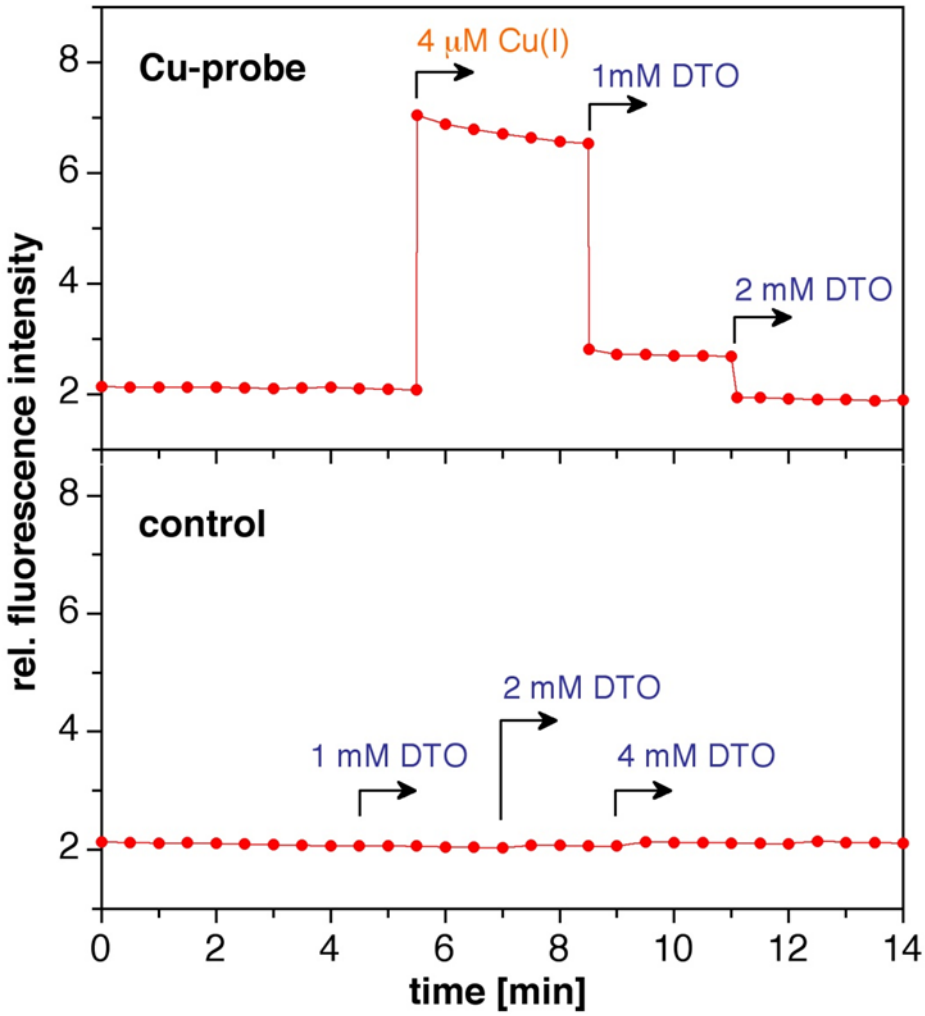

Figure 2.5: Cuvette based analysis of the fluorescence emission obtained from CTAP-1 either in the presence of 4 µM $CuCl_2$ and 1 mM or 2 mM DTO (*Top*) or 1, 2, and 4 mM DTO (*Bottom*) for fluorescence reversal assays. Data provided by Dr. Maged Henary and Dr. Liuchun Yang.

For tests in situ, cells were grown, as previously described, in growth media supplemented with 150 µM $CuCl_2$ for 12 h and subsequently either received no additional treatment or were treated with a cell-permeant Cu(I) chelator, 3,6-dithia-1,8-octanediol

(DTO) following incubation with 5 μM CTAP-1 for 30 minutes [33]. Quantitative image analysis of the fluorescence micrographs revealed that the average intracellular fluorescence intensity of the control cells (Figure 2.6A) was approximately 50% higher (40 cells; $P < 0.0001$, Student's t test) compared with DTO-treated cells (Figure 2.6B) [33]. Hence, these results served as further validation of the integrity of CTAP-1 as a genuine fluorescent sensor for probing intracellular labile copper pools.

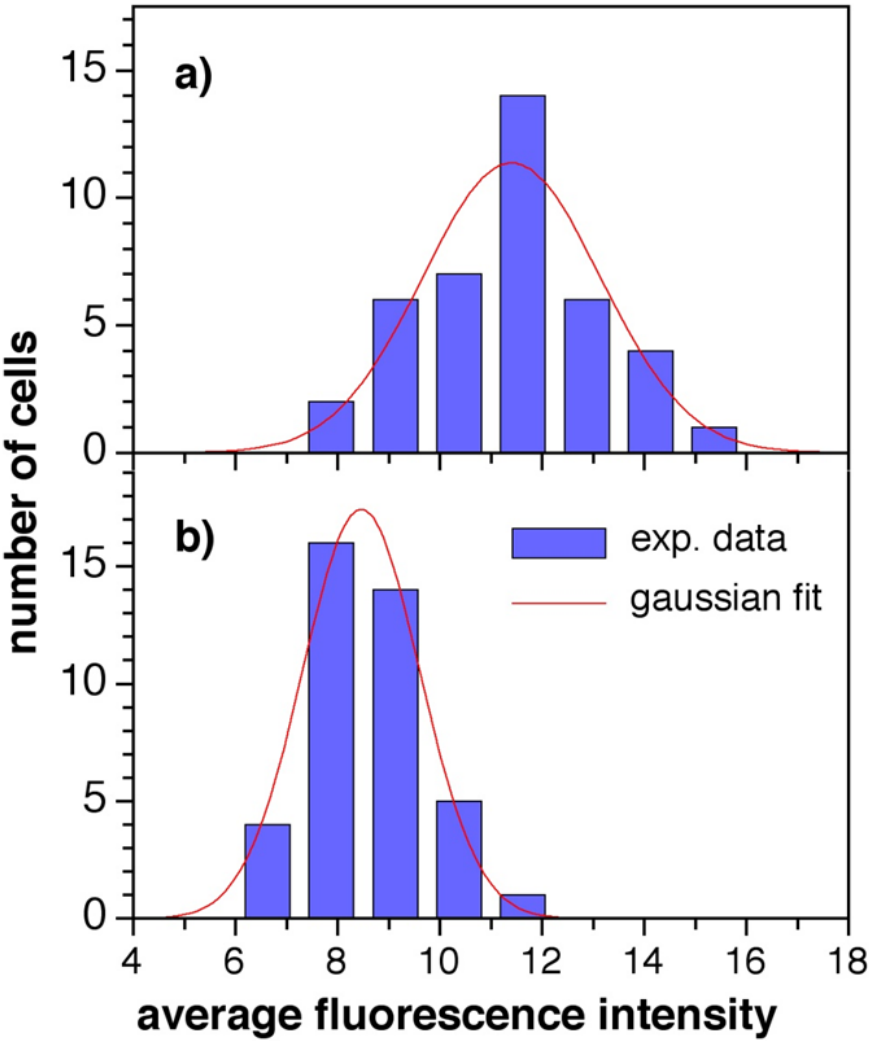

Figure 2.6: Quantitative image analysis of the fluorescence micrographs obtained from cells pre-treated with 150 μM $CuCl_2$ and stained with either CTAP-1 only (A) or CTAP-1 and 10 mM DTO (B) for fluorescence reversal assays.

After confirming the ability of CTAP-1 to respond to copper in a cellular environment, the intracellular localization of the probe was investigated using standard immunofluorescence assays and correlative fluorescence microscopy. CTAP-1 produced a staining pattern with pronounced fluorescence in a region proximal to the nucleus and slightly weaker fluorescence throughout the cytoplasm. Immunofluorescence co-

localization revealed the juxtanuclear region with prominent fluorescence to be the trans-Golgi network (TGN), labeled with anti-GS28, as indicated by the yellow-colored region in the overlay image (Figure 2.7, upper) [33]. Considerable co-localization of the probe fluorescence with the TGN is not surprising given the well-established presence of the copper transporting Menkes ATPase (ATP7a) protein in this region [34],[35]. The weaker, cytoplasmic fluorescence co-localized substantially with the mitochondria, labeled with anti-OxPhos, again indicated by the yellow color present in the overlay image (Figure 2.7, lower) [33]. Evidence for labile copper pools localized within the mitochondria was recently reported in a study performed on yeast cells [36] thus providing support for the present results revealing significant CTAP-1 fluorescence in this organelle.

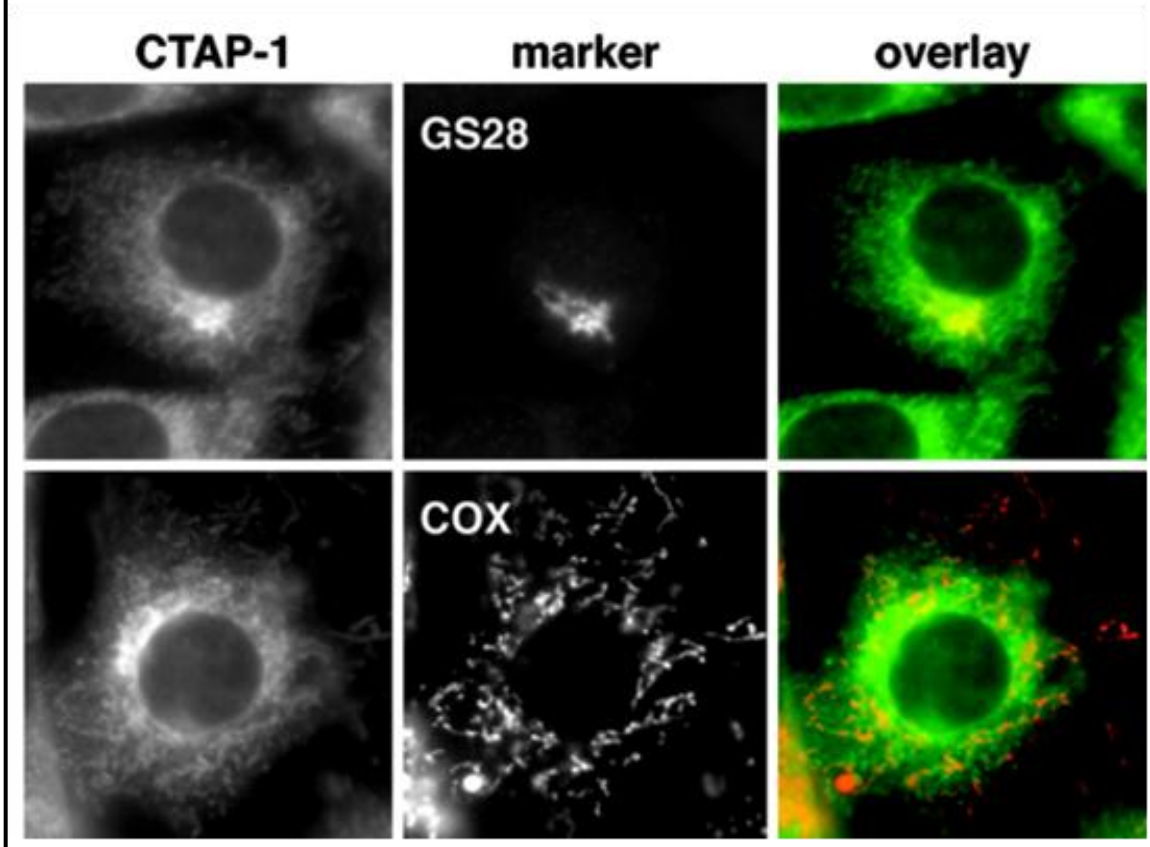

Figure 2.7: Immunofluorescence colocalization of the CTAP-1 staining pattern (Left) with two organelle-specific antibodies (Center). (Upper) Anti-GS28 for visualization of the Golgi. (Lower) Anti-OxPhos to visualize the mitochondria. (Right) False color overlay (CTAP-1, green; antibody, red; areas of colocalization, orange/yellow).

2.3 Correlating Probe Fluorescence with Copper Distribution

Synchrotron radiation based X-ray fluorescence microscopy (SXRF) has recently emerged as a promising technique for whole cell elemental imaging [35-39]. Preliminary experiments demonstrated that the intracellular fluorescence intensity of cells incubated with CTAP-1 directly reflects the availability of copper in the growth media [33]. To investigate whether the observed staining pattern is indeed due to differences in the intracellular copper distribution, we performed a series of experiments at the 2-ID-D

beam line of the Advanced Photon Source (APS) located at Argonne National Laboratory (ANL). NIH 3t3 cells were grown on the formvar layer, pre-coated with polylysine, of an electron microscopy (EM) gold grid either in basal media or in the presence of 150 μM $CuCl_2$ for 12 h, washed with 1X-PBS, and fixed in methanol/acetone (1:1) at -20°C for 2 min. Following treatment with CTAP-1 as previously described, cells were imaged via standard optical fluorescence microscopy, air-dried, and shipped to ANL for SXRF analysis.

Cells, which were cultured in medium supplemented with 150 μM $CuCl_2$, showed an approximate 20-fold increase in the K∝ signal (Figure 2.8, lower) at 8.0 keV compared with cells grown in basal media (Figure 2.8, upper) [33]. The distinct perinuclear fluorescence revealed by the copper XRF map (Figure 2.8) strongly resembles the optical fluorescence staining pattern observed for CTAP-1 (Figure 2.4) [33]. Interestingly, the XRF image also displayed a marked presence of copper localized to the nucleus of cells grown in the presence of excess copper. Accordingly, CTAP-1 also revealed a nuclear staining pattern in the cells cultured in the presence of 150 μM $CuCl_2$. However, upon consideration of the conditions used to prepare the samples, which involved a rather harsh fixation/permeabilization step with methanol/acetone, additional experiments are required to assess the integrity of the observed presence of copper in the nucleus.

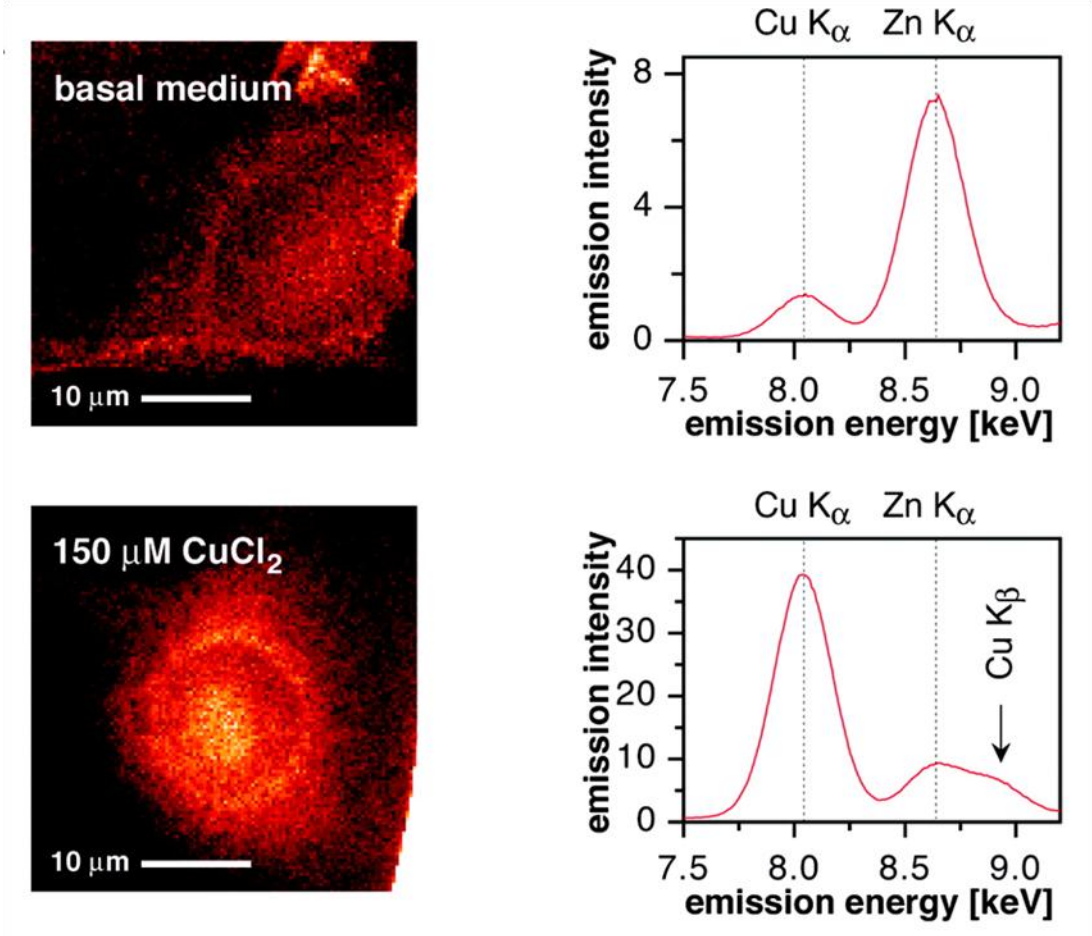

Figure 2.8: SXRF imaging of the subcellular copper topography. (Left) XRF copper maps of 3t3 cells grown under basal conditions (Upper) or in medium supplemented with 150 μM $CuCl_2$ (Lower). (Right) X-ray emission spectra for copper and zinc averaged over the entire area of the corresponding cell. Data provided by Dr. Christoph Fahrni.

The degree of co-localization between the epifluorescence staining pattern of CTAP-1 and the sub-cellular copper topography was investigated by optical and SXRF microscopy, respectively, in cells grown under elevated copper conditions (150 μM $CuCl_2$) for 12 h (Figure 2.9) [33]. Although drying the cells, a requirement for SXRF imaging, inevitably results in some distortion of the overall cellular morphology, the fluorescence micrographs indicated a high degree of co-localization between CTAP-1

fluorescence and the XRF copper distribution. Further comparison of the XRF copper topography with that of sulfur revealed significant co-localization between the two elements (Figure 2.9), hence suggesting that copper may be primarily coordinated by sulfur-donor ligands in the overlapping regions [33].

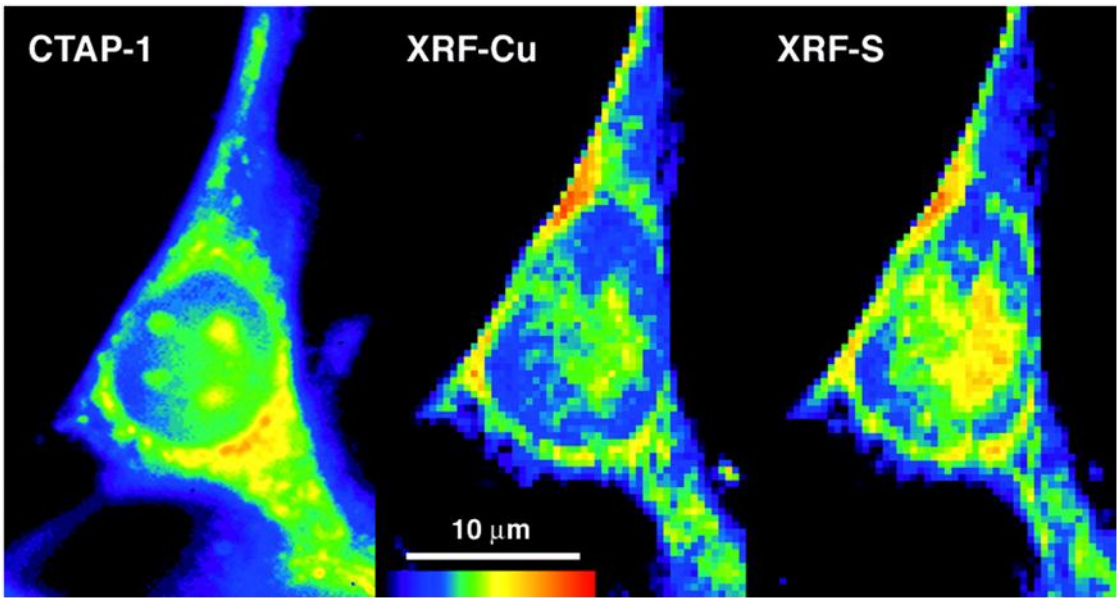

Figure 2.9: False-color micrographs of a single cell grown in medium supplemented with 150 μM $CuCl_2$ and treated with CTAP-1. (Left) Epifluorescence image acquired with a DAPI filter set. (Center) XRF copper map. (Right) XRF sulfur map. The relative intensities increase from blue to red. Data provided by Dr. Christoph Fahrni.

microXANES

The energy and shape of the near-edge x-ray absorption band of copper complexes is very sensitive toward variations in oxidation state and coordination environment. Whereas Cu(I) complexes exhibit a pre-edge feature centered around 8,984 eV characteristic for the 1s→4p transition, the analogous transition of Cu(II) complexes occurs at a significantly higher energy of 8,986 eV [40]. MicroXANES performed on a

copper-loaded NIH 3T3 (Figure 2.10A) cell revealed at all tested sub-cellular locations a near-edge feature that is characteristic for monovalent copper (Figure 2.10B). Given the higher energy of Cu(II), the observed band shape does not exclude the presence of Cu(II); nevertheless, the spectrum demonstrates that a significant portion of the total copper is present as Cu(I). Because of the complex mixture of potentially coordinating endogenous ligands, a detailed interpretation of the XANES spectrum is not possible; however, qualitative comparison with two reference compounds suggests a low-coordinate linear or trigonal geometry (Figure 10B, lower) [41, 42]. According to the literature, neither metallothionein nor glutathione exhibit the observed, characteristic XANES near-edge feature [43-45] and are therefore most likely not the prevalent endogenous ligands for coordination of kinetically labile copper in these pools.

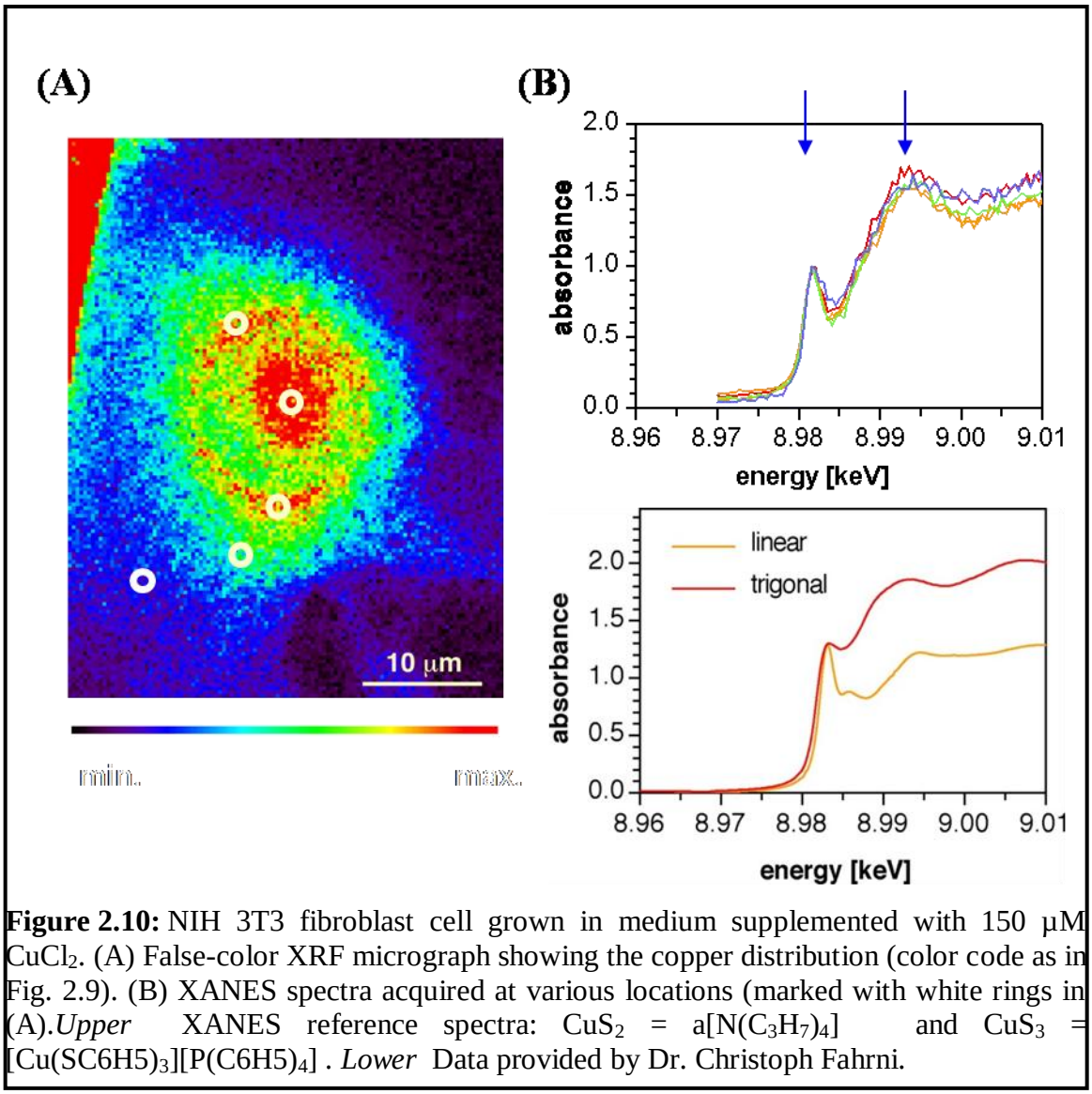

Figure 2.10: NIH 3T3 fibroblast cell grown in medium supplemented with 150 μM $CuCl_2$. (A) False-color XRF micrograph showing the copper distribution (color code as in Fig. 2.9). (B) XANES spectra acquired at various locations (marked with white rings in (A).*Upper* XANES reference spectra: CuS_2 = a$[N(C_3H_7)_4]$ and CuS_3 = $[Cu(SC6H5)_3][P(C6H5)_4]$. *Lower* Data provided by Dr. Christoph Fahrni.

Another study involved determining the oxidation state of copper within a cellular environment, an issue highly debated throughout the literature. To obtain an SXRF image with only Cu(I), a mammalian cell was first scanned at the pre-edge energy of 8,984 eV specific for Cu(I) to exclude any possible excitation of Cu(II), which has a pre-edge feature centered around an energy of 8,986 eV (Figure 2.11, *Upper Left*). Then an SXRF image incorporating both Cu(I) and Cu(II) was acquired (Figure 2.11, *Upper*

Right). The Cu(I) image was subsequently divided by the Cu(I)+Cu(II) image to obtain a ratio image illustrating the presence, if any, of Cu(II) inside of the cell (Figure 2.11, *Lower*).

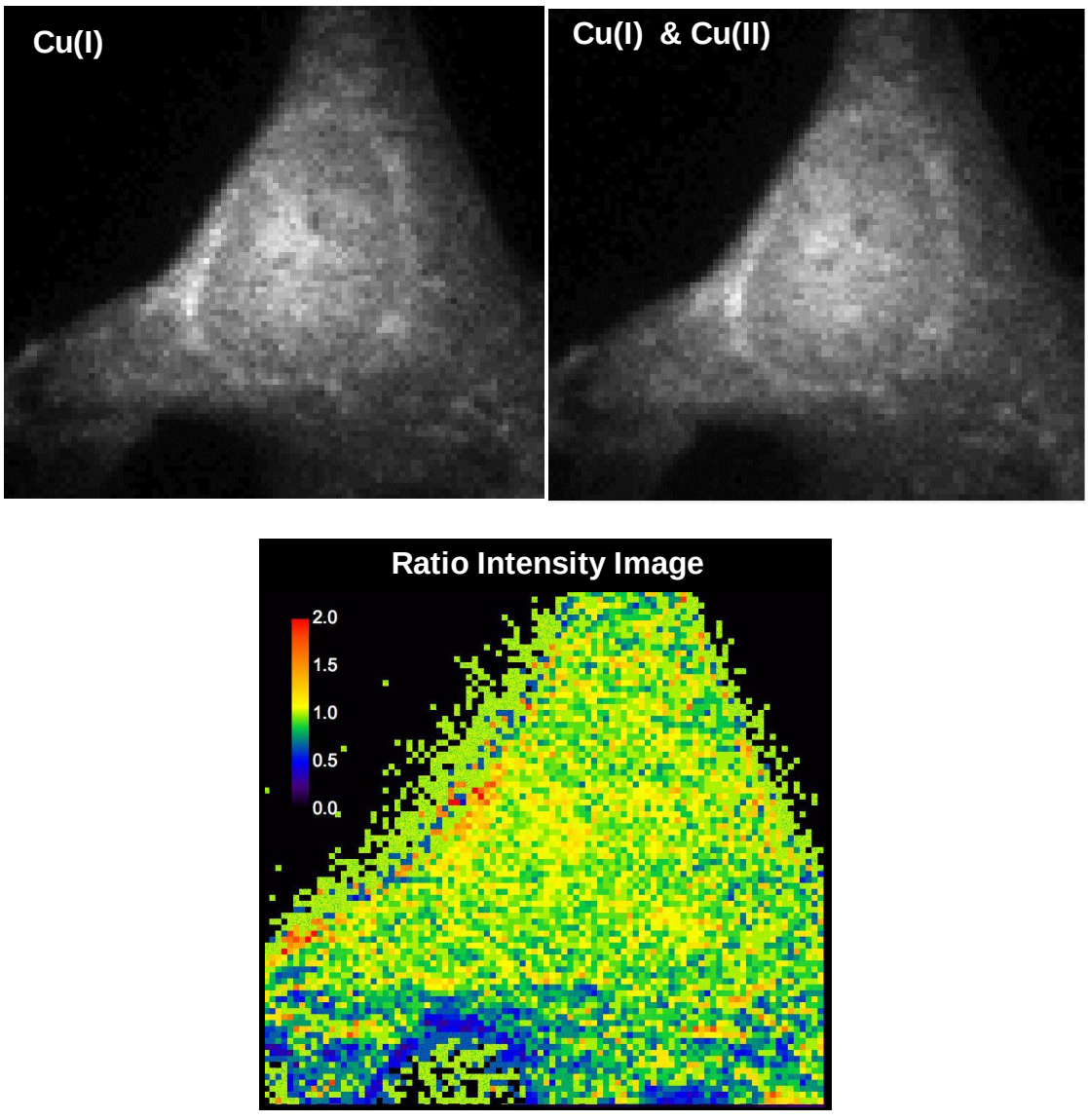

Figure 2.11: Mouse fibroblast cell grown in media supplemented with 50 µM $CuCl_2$. (*Upper, Left*) Gray scale XRF micrograph showing the Cu(I) distribution. (*Upper, Right*) Gray scale XRF micrograph showing the Cu(I)+Cu(II) distribution. (*Lower)* Ratio intensity image acquired by dividing the Cu(I) image *(upper, left)* by the Cu(I) + Cu(II) image (*upper, right*).

The resulting ratio image revealed a predominance of copper in its monovalent oxidation state as illustrated by the yellow color (ratio = 1) occurring throughout the entire cells. However, the image also suggests the presence of Cu(II) indicated by the blue color (ratio = 0.5) in a few areas located at the periphery of the cell. These data suggest that the intracellular copper primarily exists in a monovalent oxidation state within a cellular environment with negligible amounts in a divalent oxidation state.

2.4 Conclusions

A combination of standard fluorescence microscopy experiments together with SXRF elemental imaging served to validate the integrity of CTAP-1 as a Cu(I)-fluorescent probe. Fluorescence correlation of the copper-dependent intracellular staining pattern observed for CTAP-1 with immune-labeled intracellular organelles provided compelling evidence for the existence of kinetically labile copper pools localized within the mitochondria and the Golgi apparatus. Furthermore, SXRF copper topographic maps correlated strongly with CTAP-1 fluorescence and additionally showed striking similarities with the XRF sulfur topography suggesting a possible sulfur-rich coordination environment for intracellular copper. MicroXANES spectra confirmed the predominance of low-coordinate, monovalent copper throughout the cell and are inconsistent with a majority of this copper being coordinated to metallothionein or glutathione.

2.5 Materials and Methods

Materials and Cell Culture

The fluorescent probe for copper was synthesized and characterized in vitro by Dr. Maged Henary and Dr. Liuchun Yang.

Mouse NIH 3T3 cells were cultivated in DMEM supplemented with 5% calf serum and 200 mM L-glutamine. Copper uptake studies were performed in the same medium but supplemented with 150 µM copper(II) chloride. For the staining experiments cells were incubated with 10 µM CTAP-1 (in DMEM) for 50 min at 37°C, washed with PBS, and fixed with 3.7% paraformaldehyde for 30 min before mounting on slides with ProLong (Molecular Probes). For immunofluorescence co-localization, NIH 3T3 cells were fixed (3.7% paraformaldehyde, 30 min), permeabilized (0.2% Triton X-100, 2 min), and incubated with either mouse anti-GS28 IgG1 (Stressgen Bioreagents, Victoria, Canada) or mouse anti-OxPhos complex V IgG1 (Molecular Probes) primary antibodies (1:500 dilution, 1 h), respectively, and goat anti-mouse IgG Alexa Fluor 546 (Molecular Probes) as a secondary antibody following a standard immunofluorescence protocol. After the last washing step, the cells were further incubated with 10 µM CTAP-1 (in PBS, filtered) for 50 min at room temperature. The cells were imaged with a Zeiss Axiovert fluorescence microscope equipped with a standard filter set (DAPI, FITC, RITC).

Reversibility of Fluorescence Response upon Competitive Chelation of Cu(I) with 3,6-dithia-1,8-octanediol (DTO)

To test whether the fluorescence enhancement upon addition of Cu(I) to CTAP-1 is indeed due to Cu(I)-coordination, we utilized DTO as competitive exogenous chelator. Mouse NIH 3T3 fibroblast cells were grown on acid-washed coverslips to 50% confluency in Dulbecco's modified Eagle's medium (DMEM) supplemented with 5% calf serum and 200 mM L-glutamine. Upon addition of 150 μM copper(II) chloride the cells were incubated for an additional 12 hours. After washing twice with phosphate buffered saline (PBS), the cells were fixed with 3.7% paraformaldehyde for 15 min, washed again with PBS, and incubated for 50 min with a 2 μM solution of CTAP-1 (in PBS) in the presence or absence of 10 mM DTO. To guarantee a meaningful quantitative assessment of the intracellular fluorescence emission intensities, both incubation solutions were prepared from the same 2 μM stock solution of CTAP-1 in PBS. Furthermore, to minimize artifacts due to leakage of the dye into the surrounding mounting medium, the cells were mounted on glass slides by using the incubation solution that contained exactly the same concentration of CTAP-1. The fluorescence emission intensity of the CTAP1-loaded cells was quantitatively inspected with a Zeiss Axiovert fluorescence microscope equipped with a standard filter set (DAPI) and a cooled CCD camera (CoolSnap HQ, Photometrics). The average fluorescence intensity was determined based on region-of-interest (ROI) analysis of individual cells using the quantitative image analysis software package IMAGEJ [46]. For each incubation condition a total of 40 cells was analyzed, and the average fluorescence intensity distribution was plotted as histogram. The copper loaded control cells showed a

distinctly different average fluorescence intensity, which is approximately 50% higher ($p < 0.0001$; Student's t-test) compared with DTO-treated cells.

Microprobe X-ray Fluorescence Microscopy (SXRF)

Scanning x-ray fluorescence (XRF) microscopy was performed at beamline 2-ID-D of the Advanced Photon Source at the Argonne National Laboratory. Incident x-rays of 10 keV (1 eV + 1.602 x 10^{19} J) energy were chosen to excite elements from P to Zn. A Fresnel zone plate focused the x-ray beam to a spot size of 0.2 x 0.2 μm^2 on the specimen, which was raster-scanned [47]. XRF from the specimen was captured with an energy dispersive Ge detector. Spectral analysis of the fluorescence spectrum of each raster pixel then provided spatial images for each element [37]. At the hard x-ray regime, biological cells do not cause significant absorption or beam spreading, hence no specimen thinning is required, and the fluorescence image represents a two-dimensional projection of the volumetric distribution for each element. For sample preparation, cells were allowed to attach to the formvar layer of a gold electron microscopy (EM) grid. Upon treatment with CTAP-1 as described above, cells were washed in PBS, fixed in methanol acetone (1:1) at 20°C for 2 min, and then air dried.

Microprobe X-Ray Absorption Near-Edge Structure (microXANES)

Once an interesting area was identified in the XRF image, microXANES [48] was performed by scanning the energy of the incident x-ray across the Cu K edge (≈ 8.979 keV). The zone plate and the specimen remained stationary during the measurement,

which ensured that the illuminated area was fixed during the energy scan, although slight defocusing increased the spot size to 0.25 x 0.25 μm^2.

2.3 Literature Cited

1. Tapiero, H., Townsend, D. M., & Tew, K. D. (2003) Trace elements in human physiology and pathology. Copper. *Biomed. Pharmacother.* **57**, 386-398.

2. Bertinato, J., & L'abbe, M. R. (2004) Maintaining copper homeostasis: Regulation of copper-trafficking proteins in response to copper deficiency or overload. *J. Nutr. Biochem.* **15**, 316-322.

3. Llanos, R. M., & Mercer, J. F. B. (2002) The molecular basis of copper homeostasis and copper-related disorders. *DNA Cell Biol.* **21**, 259-270.

4. Harris, E. D. (2001) Copper homeostasis: The role of cellular transporters. *Nutr. Rev.* **59**, 281-285.

5. Huffman, D. L., & O'halloran, T. V. (2001) Function, structure, and mechanism of intracellular copper trafficking proteins. *Annu. Rev. Biochem.* **70**, 677-701.

6. Mercer, J. F. B. (2001) The molecular basis of copper-transport diseases. *Trends Mol. Med* **7**, 64-69.

7. Waggoner, D. J., Bartnikas, T. B., & Gitlin, J. D. (1999) The role of copper in neurodegenerative disease. *Neurobiol. Dis.* **6**, 221-230.

8. Sayre, L. M., Perry, G., Atwood, C. S., & Smith, M. A. (2000) The role of metals in neurodegenerative diseases. *Cell. Mol. Biol.* **46**, 731-741.

9. Sayre, L. M., Perry, G., & Smith, M. A. (1999) Redox metals and neurodegenerative disease. *Curr. Opin. Chem. Biol.* **3**, 220-225.

10. Rosenzweig, A. C. (2001) Copper delivery by metallochaperone proteins. *Accounts Chem. Res.* **34**, 119-128.

11. Puig, S., & Thiele, D. J. (2002) Molecular mechanisms of copper uptake and distribution. *Curr. Opin. Chem. Biol.* **6**, 171-180.

12. Easmon, J. (2002) Copper and iron complexes with antitumour activity. *Expert Opin. Ther. Patents* **12**, 789-818.

13. Eisses, J. F., Chi, Y. Q., & Kaplan, J. H. (2005) Stable plasma membrane levels of hctr1 mediate cellular copper uptake. *J. Biol. Chem.* **280**, 9635-9639.

14. Eisses, J. F., & Kaplan, J. H. (2005) The mechanism of copper uptake mediated by human ctr1 - a mutational analysis. *J. Biol. Chem.* **280**, 37159-37168.

15. Cobine, P. A., Pierrel, F., & Winge, D. R. (2006) Copper trafficking to the mitochondrion and assembly of copper metalloenzymes. *Biochim. Biophys. Acta-Mol. Cell Res.* **1763**, 759-772.

16. Schmidt, P. J., Kunst, C., & Culotta, V. C. (2000) Copper activation of superoxide dismutase 1 (sod1) in vivo - role for protein-protein interactions with the copper chaperone for sod1. *J. Biol. Chem.* **275**, 33771-33776.

17. Schmidt, P. J., Rae, T. D., Pufahl, R. A., Hamma, T., Strain, J., O'halloran, T. V., et al. (1999) Multiple protein domains contribute to the action of the copper chaperone for superoxide dismutase. *J. Biol. Chem.* **274**, 23719-23725.

18. Casareno, R. L. B., Waggoner, D., & Gitlin, J. D. (1998) The copper chaperone ccs directly interacts with copper/zinc superoxide dismutase. *J. Biol. Chem.* **273**, 23625-23628.

19. Gitlin, J. D. (2003) Wilson disease. *Gastroenterology* **125**, 1868-1877.

20. Culotta, V. C., Yang, M., & O'halloran, T. V. (2006) Activation of superoxide dismutases: Putting the metal to the pedal. *Biochim. Biophys. Acta-Mol. Cell Res.* **1763**, 747-758.

21. Lamb, A. L., Wernimont, A. K., Pufahl, R. A., Culotta, V. C., O'halloran, T. V., & Rosenzweig, A. C. (1999) Crystal structure of the copper chaperone for superoxide dismutase. *Nat. Struct. Biol.* **6**, 724-729.

22. Lamb, A. L., Wernimont, A. K., Pufahl, R. A., O'halloran, T. V., & Rosenzweig, A. C. (2000) Crystal structure of the second domain of the human copper chaperone for superoxide dismutase. *Biochemistry* **39**, 1589-1595.

23. Horng, Y. C., Cobine, P. A., Maxfield, A. B., Carr, H. S., & Winge, D. R. (2004) Specific copper transfer from the cox17 metallochaperone to both sco1 and cox11 in the assembly of yeast cytochrome c oxidase. *J. Biol. Chem.* **279**, 35334-35340.

24. Arnesano, F., Banci, L., Bertini, I., & Bonvin, A. (2004) A docking approach to the study of copper trafficking proteins: Interaction between metallochaperones and soluble domains of copper atpases. *Structure* **12**, 669-676.

25. Strausak, D., Howie, M. K., Firth, S. D., Schlicksupp, A., Pipkorn, R., Multhaup, G., et al. (2003) Kinetic analysis of the interaction of the copper chaperone atox1 with the metal binding sites of the menkes protein. *J. Biol. Chem.* **278**, 20821-20827.

26. Hamza, I., Schaefer, M., Klomp, L. W., & Gitlin, J. D. (1999) Interaction of the copper chaperone hah1 with the wilson disease protein is essential for copper homeostasis. **96**, 13363-13368.

27. Petris, M. J., Camakaris, J., Greenough, M., Lafontaine, S., & Mercer, J. F. B. (1998) A c-terminal di-leucine is required for localization of the menkes protein in the trans-Golgi network. *Hum. Mol. Genet.* **7**, 2063-2071.

28. Petris, M. J., Mercer, J. F. B., Culvenor, J. G., Lockhart, P., Gleeson, P. A., & Camakaris, J. (1996) Ligand-regulated transport of the menkes copper p-type atpase efflux pump from the Golgi apparatus to the plasma membrane: A novel mechanism of regulated trafficking. **15**, 6084-6095.

29. Petris, M. J., Voskoboinik, I., Cater, M., Smith, K., Kim, B. E., Llanos, R. M., et al. (2002) Copper-regulated trafficking of the menkes disease copper atpase is associated with formation of a phosphorylated catalytic intermediate. *J. Biol. Chem.* **277**, 46736-46742.

30. Arnesano, F., Banci, L., Bertini, I., & Ciofi-Baffoni, S. (2004) Perspectives in inorganic structural genomics: A trafficking route for copper. *Eur. J. Inorg. Chem.*, 1583-1593.

31. Rae, T. D., Schmidt, P. J., Pufahl, R. A., Culotta, V. C., & O'halloran, T. V. (1999) Undetectable intracellular free copper: The requirement of a copper chaperone for superoxide dismutase. *Science* **284**, 805-808.

32. Herd, S. M., Camakaris, J., Christofferson, R., Wookey, P., & Danks, D. M. (1987) Uptake and efflux of copper-64 in menkes-disease and normal continuous lymphoid-cell lines. *Biochem. J.* **247**, 341-347.

33. Yang, L. C., Mcrae, R., Henary, M. M., Patel, R., Lai, B., Vogt, S., et al. (2005) Imaging of the intracellular topography of copper with a fluorescent sensor and by synchrotron x-ray fluorescence microscopy. *Proc. Natl. Acad. Sci. U. S. A.* **102**, 11179-11184.

34. Yang, L., Mcrae, R., Henary, M. M., Patel, R., Lai, B., Vogt, S., et al. (2005) Imaging of the intracellular topography of copper with a fluorescent sensor and by synchrotron x-ray fluorescence microscopy. **102**, 11179-11184.

35. Dillon, S. A., Burmi, R. S., Lowe, G. M., Billington, D., & Rahman, K. (2003) Antioxidant properties of aged garlic extract: An in vitro study incorporating human low density lipoprotein. *Life Sci.* **72**, 1583-1594.

36. Kemner, K. M., Kelly, S. D., Lai, B., Maser, J., O'loughlin, E. J., Sholto-Douglas, D., et al. (2004) Elemental and redox analysis of single bacterial cells by x-ray microbeam analysis. **306**, 686-687.

37. Twining, B. S., Baines, S. B., Fisher, N. S., Maser, J., Vogt, S., Jacobsen, C., et al. (2003) Quantifying trace elements in individual aquatic protist cells with a synchrotron x-ray fluorescence microprobe. *Anal. Chem.* **75**, 3806-3816.

38. Twining, B. S., Baines, S. B., Fisher, N. S., Jacobsen, C., & Maser, J. (2003) Quantification and localization of trace metals in natural plankton cells using a synchrotron x-ray fluorescence microprobe. *J. Phys. IV* **104**, 435-438.

39. Paunesku, T., Stojicevic, N., Vogt, S., Maser, J., Lai, B., Rajh, T., et al. (2003) Intracellular localization of titanium dioxide-biomolecule nanocomposites. *J. Phys. IV* **104**, 317-319.

40. Kau, L. S., Spirasolomon, D. J., Pennerhahn, J. E., Hodgson, K. O., & Solomon, E. I. (1987) X-ray absorption-edge determination of the oxidation-state and coordination-number of copper - application to the type-3 site in rhus-vernicifera laccase and its reaction with oxygen. **109**, 6433-6442.

41. Koch, S. A., Fikar, R., Millar, M., & Osullivan, T. (1984) Steric control of metal thiolate coordination - synthesis and structure of monomeric cobalt(ii) and copper(i) thiolate complexes. *Inorg. Chem.* **23**, 121-122.

42. Coucouvanis, D., Murphy, C. N., & Kanodia, S. K. (1980) Metal-mercaptide chemistry - synthesis and structural characterization of the [cu(sc6h5)3]2- anion - a rational synthesis and the structure of the [cu4(sc6h5)6]2- cluster. *Inorg. Chem.* **19**, 2993-2998.

43. Pickering, I. J., George, G. N., Dameron, C. T., Kurz, B., Winge, D. R., & Dance, I. G. (1993) X-ray-absorption spectroscopy of cuprous thiolate clusters in proteins and model systems. **115**, 9498-9505.

44. Smith, T. A., Lerch, K., & Hodgson, K. O. (1986) Structural study of the cu sites in metallothionein from neurospora-crassa. **25**, 4677-4680.

45. Corazza, A., Harvey, I., & Sadler, P. J. (1996) H-1,c-13-nmr and x-ray absorption studies of copper(i) glutathione complexes. **236**, 697-705.

46. Ringkob, T. P., Swartz, D. R., & Greaser, M. L. (2004) Light microscopy and image analysis of thin filament lengths utilizing dual probes on beef, chicken, and rabbit myofibrils. *J. Anim. Sci.* **82**, 1445-1453.

47. Yun, H. K., Yi, S. Y., Yu, S. H., & Choi, D. (1999) Cloning of a pathogenesis-related protein-1 gene from nicotiana glutinosa l and its salicylic acid-independent induction by copper and beta-aminobutyric acid. *J. Plant Physiol.* **154**, 327-333.

48. Dillon, C. T., Kennedy, B. J., Lay, P. A., Lai, B., Cai, Z., Stampfl, A. P. J., et al. (2003) Implementation of x-ray microscopy and micro-xanes analysis for investigations of the cellular uptake and cellular metabolism of transition metals. **104**, 293-296.

CHAPTER 3
INVESTIGATING LABILE ZINC POOLS WITH RATIOMETRIC FLUORESCENT PROBES

3.1 Biological Relevance of Zinc

Divalent zinc is set apart from other transition metals by its lack of color, redox inactivity within the physiologically accessible potential range, and its failure to provide stability or inertness to its complexes [1],[2]. Because divalent zinc is characterized by a completely filled d-shell, Zn(II) chemistry involves no ligand field effects thereby providing Zn(II) complexes with relatively low thermodynamic stability and able to achieve low activation barriers in terms of reactivity [1]. Furthermore, compared with manganese, chromium, nickel, and copper, Zn(II) forms relatively soluble complexes and may be readily found in all waters [1]. The above properties, combined, render Zn(II) with the attractive properties of availability, mobility, and versatility for participating in a large number of biological roles [1]. Whether playing a structural role as in the Zn(II) finger proteins or, in a lesser number of cases, a functional role in enzymes, Zn(II) assumes a larger number of roles than any other metal in living organisms [1]. Indeed, as of 2007, over 12% of the proteins listed in the Brookhaven Protein Data Base (PDB) contained Zn(II) [1]. Consequently, Zn(II) is ubiquitous in nature and is an absolute necessity for the vitality of living organisms.

The biological roles for Zn(II) are both abundant and diverse [3]. The intracellular requirement for Zn(II) is revealed through its participation in both structural and functional roles in 3-10% of proteins in the mammalian genome [4, 5]. Additional

roles for Zn(II) in processes such as DNA/RNA synthesis, cell division, and apoptosis have also been reported [6-12]. The biological significance of this metal is further underscored by the pathological conditions of severe growth retardation and impaired brain and immune function, which manifest from Zn(II) deficiency [13, 14]. Moreover, reports have also suggested a role for Zn(II) in both the alleviation and development of diabetes, although the underlying molecular mechanisms governing these functions remain poorly understood [15, 16]. Hence, it is not surprising that cells have developed sophisticated homeostatic machinery to ensure that Zn(II) is present in amounts necessary for proper cellular functioning but does not accumulate to excess.

Intracellular Regulation of Zinc

The large number of proteins dedicated to the transport and buffering of intracellular Zn(II) levels illuminate both the significance and complexity of Zn(II) homeostasis (Figure 3.1) [3, 17, 18]. The homeostatic machinery consists of 10 members of the ZnT (Zn^{2+} transporter) family, 15 members of the ZIP (Zn^{2+} regulatory transporter, iron regulatory metal transporter-like protein) family, and 3 distinct isoforms of metallothionein (MT) [3, 17, 18]. The rapid exchange of Zn(II) with the extracellular medium as well as the existence of multiple pathways for Zn(II) uptake and export suggests the existence of significant roles for both exchangeable Zn^{2+} ions and Zn(II) transporters (ZnTs) in intracellular physiology and pathological conditions [3, 17, 18].

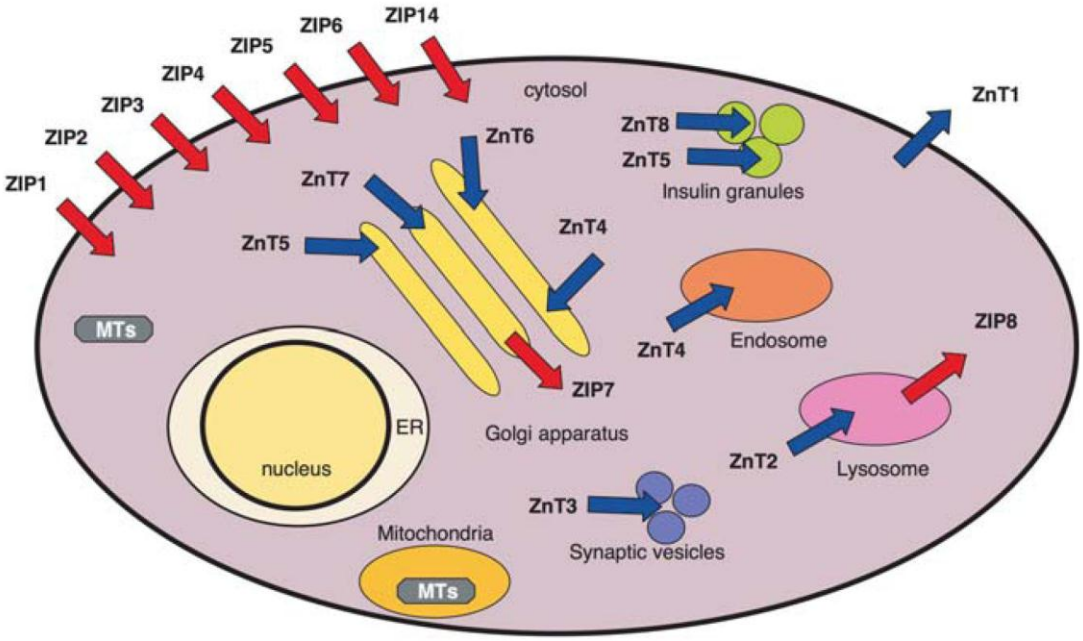

Figure 3.1: Zn(II) Trafficking in Mammalian Cells. Reproduced from reference [5].

Intracellular Labile Zinc Pools

The family of ZIP proteins mediates Zn(II) uptake from the extracellular environment into the cytoplasm [19]. Once inside the cell, Zn(II) may localize to one of four available pools of small molecules or proteins [3, 16, 20-22]. A major pool comprises metallothionein (MT) proteins, which buffer Zn(II) at two distinctly different concentrations of 5×10^{7} M^{-1} for the more loosely bound Zn(II) and 6×10^{11} M^{-1} for the more tightly bound Zn(II) [23]. The ZnT family of proteins both exports Zn(II) from the cytosol to the extracellular environment mediates the delivery of Zn(II) to major intracellular organelles such as the mitochondria, golgi apparatus (GA), and endoplasmic reticulum (ER) where Zn(II) is provided to its necessary proteins and enzymes [3, 16, 20-22]. These organelles may additionally serve to sequester Zn(II) into pools for Zn(II)

storage and/or detoxification [3, 16, 20-22]. Finally, ZnT proteins such as SOD and MT may also traffick Zn(II) into more specialized organelles such as secretory granules or insulin granules [3, 16, 20-22]. Given the abundance of high-affinity cytosolic Zn(II)-binding proteins, intracellular labile Zn(II) concentrations are estimated to be in the subnanomolar concentration range and are thus often difficult to investigate effectively [2, 4, 22]. This low concentration combined with the complexity of Zn(II) transport machinery render the development of sensitive methodologies for studying labile Zn(II) pools a worthwhile endeavor for acquiring a more complete understanding of the storage, uptake, and mechanisms involved in Zn(II) homeostasis.

3.2 Fluorescent Probes for the Detection of Labile Zinc

Numerous fluorescent probes have been developed for the detection of Zn(II) in biological systems (Table 3.1), and their widespread application has provided a wealth of information regarding the nature of labile Zn(II) pools [24]. More recently, genetically encoded Zn(II) sensors with specific target sequences and conjugated to green fluorescent protein (GFP) or a GFP variant as the reporter molecule have emerged and provided details of the physiological function of labile Zn(II) in various sub-cellular compartments [25, 26]. Although the development and application of Zn(II)-selective fluorescent probes have been largely successful, the majority of these sensors remain plagued with various drawbacks often characterized by a requirement for UV excitation and/or equivocal fluorescence responses to Zn^{2+}, which render them essentially unsuitable for obtaining accurate quantitative information. Therefore, the design of new fluorescent probes for labile Zn(II) remains an ongoing area of intense research.

Table 3.1: Thermodynamic and photophysical properties of Zn(II)-selective probes commonly applied in biology. *(f)* denotes the free ligand and *(b)* denotes the Zn(II)-bound ligand.

Zinc Probe	Structure	Ex/Em λ (nm)	Quantum Yield	Binding Affinity	Application (s)
Zinquin ester	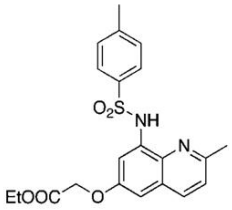	370 / 490 [Zalewski, 1993; Zalewski, 1996; Zalewski, 1994; Kimber, 2000; Hendrickson, 2003]		a	wide range of biological applications for determining the role of labile Zn(II) pools [Zalewski, 1993; Mahadevan, 1995; Ranaldi, 2002]
FluoZin-3	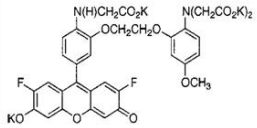	491 / 520	< 0.005 *(f)* 0.43 *(b)*	15 nM	wide range of biological applications for determining the role of labile Zn(II) pools [Gee, 2002; Gee, 2002; Muylle, 2006]
ZnAF2	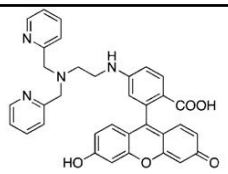	490 / 574 *(f)* 492 / 514 *(b)*	0.023 *(f)* 0.36 *(b)*	2.7 nM	detection of synaptically released Zn(II) in rat hippocampal slices [Hirano, 2002] and various cellular applications [Hirano, 2000; Hirano, 2002]
ZP3	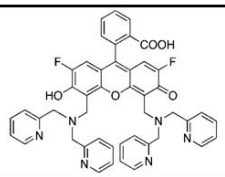	502 / 521 *(f)* 492 / 516 *(b)*	0.15 *(f)* 0.92 *(b)*	0.7 nM	imaging endogenous Zn(II) pools localizd within rat hippocampal slices [Chang, 2004]
ZnIC	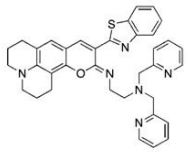	513 / 543 *(f)* 513 / 558 *(b)*	0.80 *(f)* 0.76 *(b)*	1.3 pM	ratiometric detection of Zn(II) in culture cells and in rat hippocampal slices [Komatsu, 2007]
AZn2	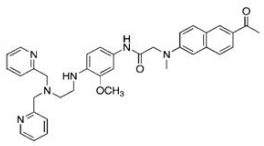	365 / 494 *(f)* 365 / 499 *(b)* 780 / 499 *(b)*	0.012 *(f)* 0.65 *(b)*	0.5 nM	applications investigating the release of presynaptic Zn(II) stores from rat hippocampal slices [Kim, 2008]

Ratiometric Fluorescent Probes

Several factors including the properties of the illumination source; the optical and spectroscopic characteristics of the microscope; and the resolution, sensitivity, and

signal-to-noise ratio achieved by the detector complicate the quantification of Zn(II) concentrations based on the fluorescence emission response [27]. Furthermore, the fluorescence intensity of a fluorophore may be attenuated by photobleaching that accompanies illumination, is sensitive to the physical environment, and is often affected by interactions occurring between fluorophore moieties when present at high concentrations [27]. Due to the large number of factors confounding the accurate quantification of fluorescence intensity, probes that undergo a change in fluorescence emission intensity upon selectively binding a particular analyte are effectively only useful for obtaining qualitative rather than quantitative information.

Fluorescence ratio imaging offers a unique opportunity to acquire quantitative information from a fluorescent probe [27]. Fluorescent probes that demonstrate a spectral shift upon binding analyte effectively circumvent the problems typically associated with quantifying fluorescence because the free ligand can be chromatically distinguished from the analyte-bound form [28, 29]. Fluorescence ratio microscopy hence involves collecting two fluorescence images and relating the analyte concentration to the intensity ratio of the two images [27]. The field of ratiometric imaging was originally introduced by Tsien and co-workers with the development and application of calcium-selective fluorescent probes designed for accurately quantifying intracellular levels of Ca^{2+} [28, 30]. For example, the widely applied calcium-selective probe, fura-2, undergoes a shift in the fluorescence excitation spectrum to shorter wavelengths upon binding Ca^{2+} (Figure 3.2), while maintaining a steady fluorescence emission maximum wavelength [30]. As illustrated with Equation (1), the free Zn(II) concentration can be directly related to the intensity ratios:

$$[M^{n+}] = K_d((F - F_{min})/(F_{max} - F)) \quad \textbf{(1)}$$

where K_d is the dissociation constant of the metal-probe complex, and F_{min} and F_{max} are the minimum and maximum intensity for the free and saturated probe, respectively.

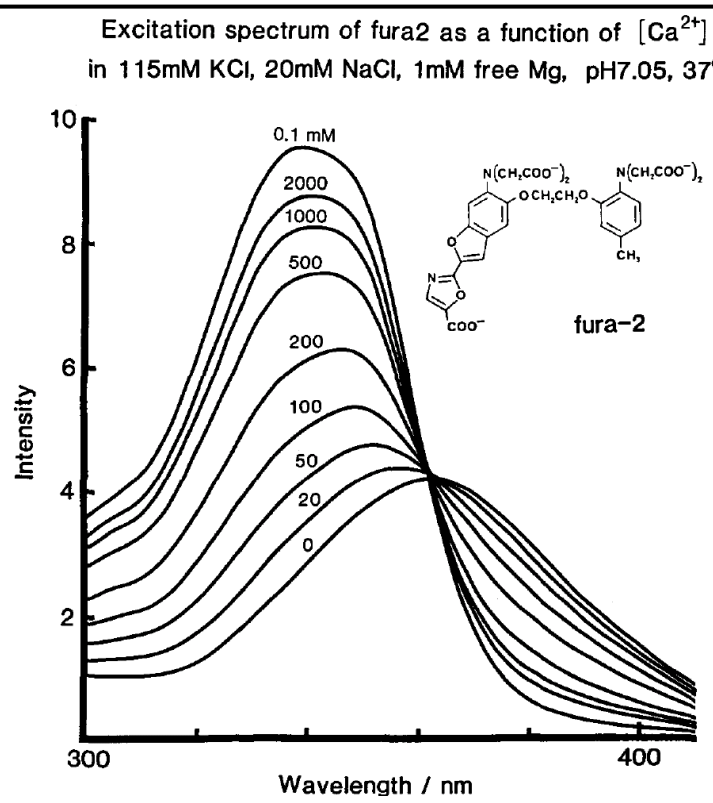

Figure 3.2: The excitation spectrum of fura-2 shifts upon binding calcium ions. The excitation maxima shifts toward 340 nm as the amount of calcium increases. The emission was monitored at 505 nm. Reproduced from reference [30].

Although ratiometric probes have been developed for Zn^{2+} (Table 3.1), only a few have been applied successfully to biological systems and their development remains a strongly pursued area of research.

Two-Photon Excitation Microscopy (TPEM)

With better depth penetration and excitation in the near infrared (IR), two-photon excitation microscopy (TPEM) is growing in popularity because of the distinct advantages it offers for bio-imaging applications compared with traditional fluorescence imaging, which uses single-photon excitation [31]. Two-photon absorption (2PA) involves the simultaneous interaction of two photons which increases non-linearly with the square of the light intensity, whereas 1PA depends linearly on the intensity [32-36]. Away from the focal plane, the TPE efficiency drops rapidly so that no fluorescence is emitted (Figure 3.3b) and three-dimensional image resolution is achieved [32-36].

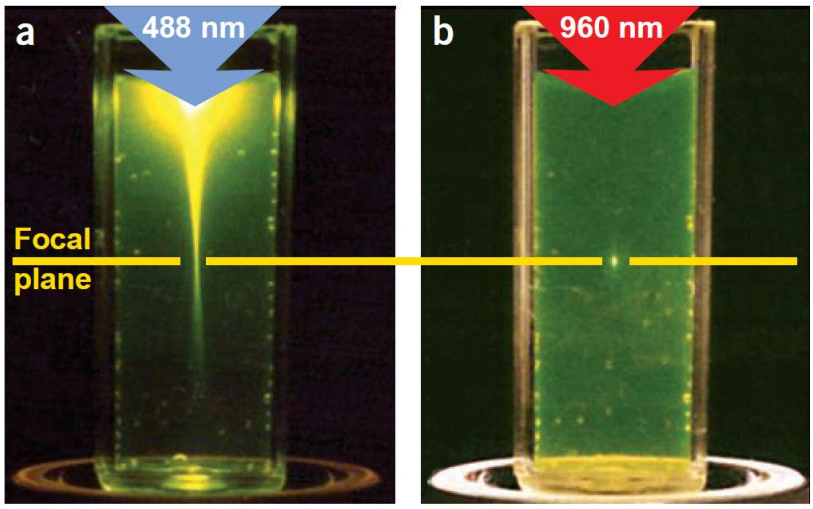

Figure 3.3: Localization of excitation by two-photon excitation (TPE). (a) Single-photon excitation of fluorescein by focused 488 nm light (0.16 NA). (b) Two-photon excitation using focused (0.16 NA) femtosecond pulses of 960 nm light. Reproduced from reference [31].

For TPE, two photons of approximately equal energy interact with a molecule, producing an excitation equivalent to the absorption of a single photon possessing twice the energy (Figure 3.3) [32-36]. Therefore, the two-photon process only requires half the energy or twice the wavelength to excite the fluorophore and therefore offers improved

depth penetration in scattering media, reduced phototoxicity, and negligible background fluorescence [32-36]. Furthermore, TPEM is characterized by a localized excitation (fL excitation volumes) and presents an expanded wavelength accessibility of most fluorophores [32-36]. These characteristics render TPEM particularly attractive for live cell imaging studies and imaging tissue samples in biomedical research [32-36].

Although presumably most fluorophore platforms can be used for TPEM applications as labels or fluorescent probes, they have typically not been optimized for TPEM applications. The brightness of a fluorescent dye is defined by the product of the quantum yield (η) and absorption cross section (δ)[32-36]. While the quantum yield can be assumed as independent of the excitation mode, the cross section follows different quantum mechanical rules for non-linear two-photon excitation versus one-photon excitation processes [32-36]. Consequently, optimizing the cross section of a fluorophore for TPEM is required in order to improve its optical sensitivity and brightness.

Given the advantages offered by TPEM combined with the unique opportunities presented by fluorescence ratio imaging compared with the more traditional fluorescence enhancement approach, a fluorescent probe incorporating both attributes would be ideal for biological applications. Systematic optimization of the TPA cross-section and Zn(II)-induced fluorescence shift led to the development of probe, SL-326 (Figure 3.4) [37]. The goal of the present study was therefore to characterize the intracellular Zn(II)-induced fluorescence shift of SL-326 and ultimately determine its ability to dynamically monitor subtle changes occurring in the both the extracellular and intracellular Zn(II) environments [29].

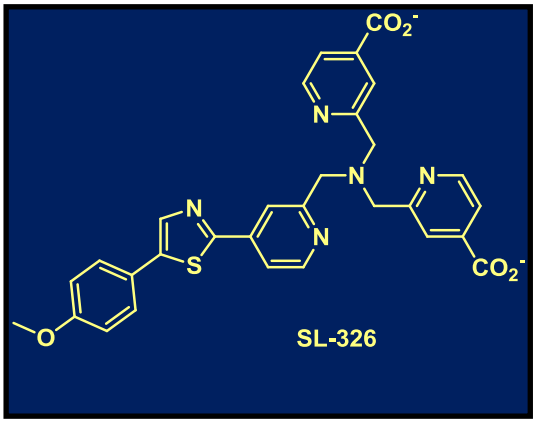

Figure 3.4: Schematic of Zn(II)-selective ratiometric probe with optimized two-photon absorption (TPA) cross section.

3.3 Optical Sensing of Zinc

Measurements performed *in vitro* of the TPA cross section revealed a maximum absorption of both the free ligand and Zn(II)-bound ligand centered around 710 nm (Figure 3.5), while the Zn(II)-bound ligand also showed substantially higher absorption than the free ligand at wavelengths around 850 nm or higher (Figure 3.5).

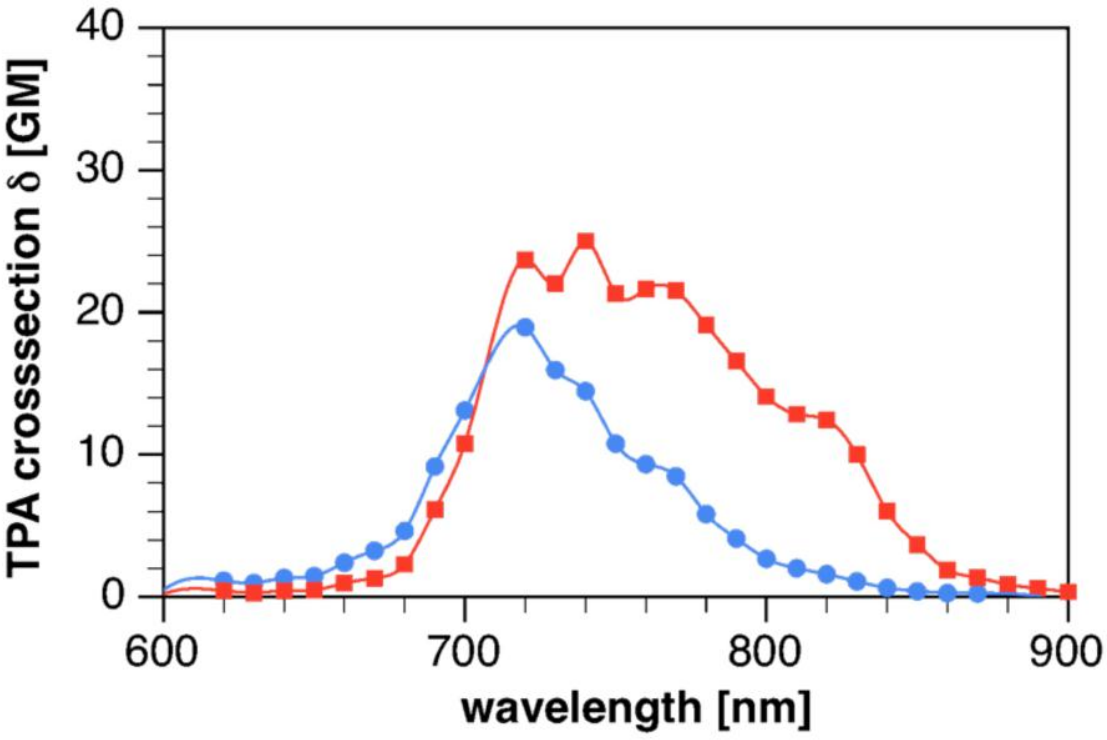

Figure 3.5: Two-photon absorption (TPA) cross-section of SL-326. (blue) TPA of the free ligand (86.3 µM SL-326) and (red) TPA of the SL-326 saturated with Zn(II) (10.3 µM) measured in PIPES (10 mM), KCl (0.1 mM) buffer at pH 7.05. Data provided by Dr. S. Sumalekshmy [*unpublished results*].

Investigation of the probe response to Zn(II) showed a maximum fluorescence emission of 482 nm for the unbound probe and a maximum fluorescence emission of 520 nm characterized by a substantially higher intensity in the presence of increasing amounts of Zn(II) ions (Figure 3.6).

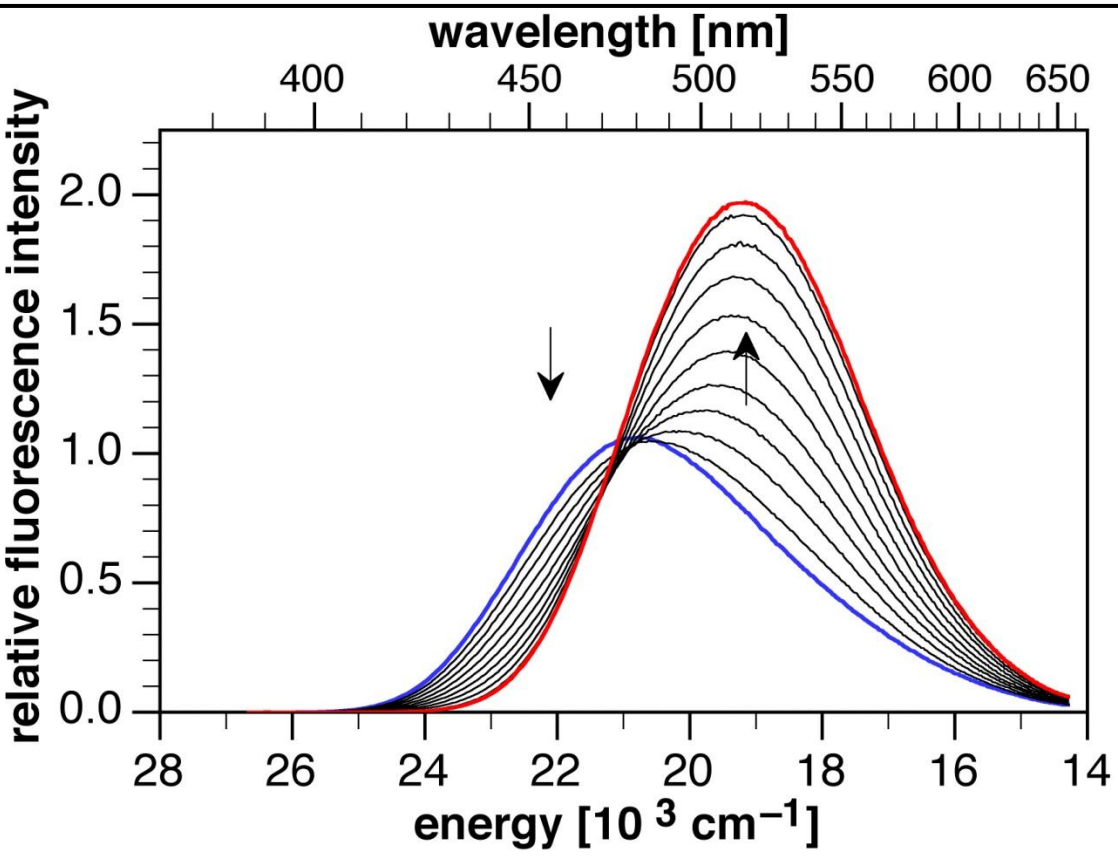

Figure 3.6: Fluorescence emission spectra of SL-326 as a function of Zn(II) concentration with excitation at 358 nm. (*blue*) Fluorescence emission of the free ligand (86.3 µM SL-326) and (*red*) in the presence of increasing amounts of Zn(II) (0-10.3 µM) measured in PIPES (10 mM), KCl (0.1 mM) buffer at pH 7.05. Data provided by Dr. S. Sumalekshmy [*unpublished results*].

For characterization of the dye properties *in situ*, NIH 3T3 mouse fibroblasts were pre-loaded with 10 µM SL-326 in basal growth media and received either no additional treatment or were supplemented with 100 µM $ZnSO_4$:10 µM pyrithione for 30 minutes. The cells received a mild fixation for 5 minutes with 3.7% paraformaldehyde (PFA) and were washed and subsequently mounted onto slides for TPEM. A wavelength emission scan was then performed for each sample using 760 nm for excitation and 20 nm intervals between channels ranging from 415 nm to 587 nm for collecting the fluorescence micrographs. The fluorescence images paralleled the *in vitro* measurements

indicating a similar emission maximum for the free ligand (Figure 3.7) as well as the Zn(II)-bound ligand (Figure 3.8).

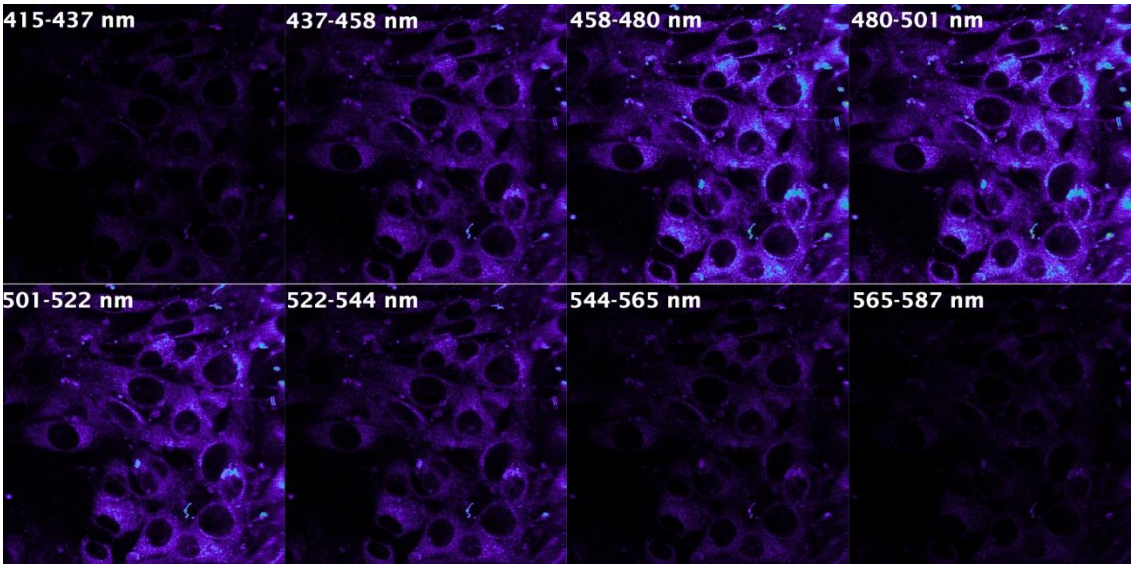

Figure 3.7: Fluorescence emission of SL-326 in fixed NIH 3T3 mouse fibroblasts grown in basal media. Excitation at 750 nm was used and emission was collected in separate channels at approximately 20 nm increments.

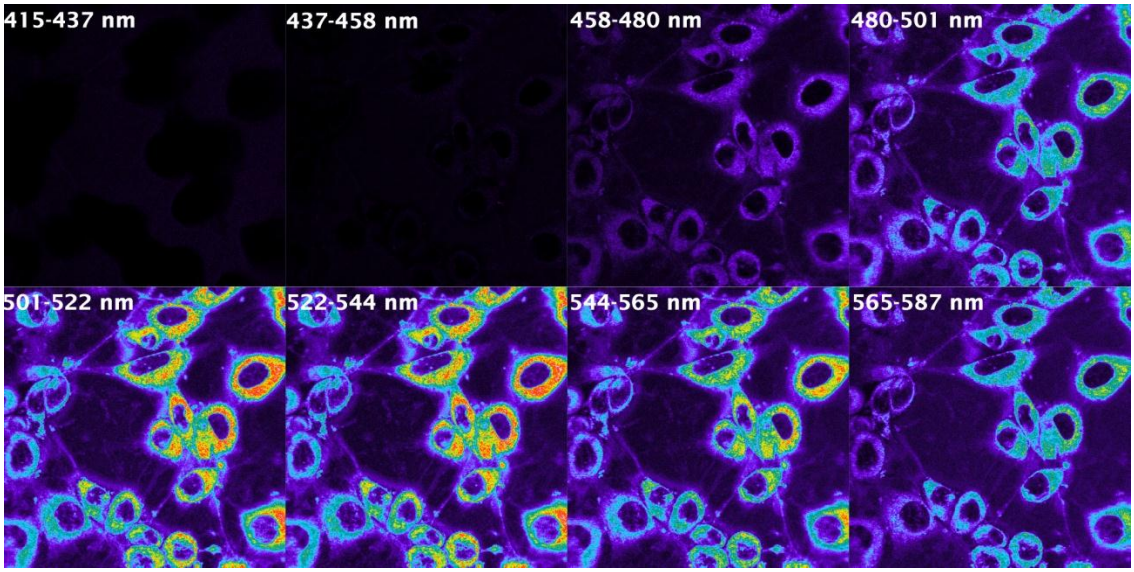

Figure 3.8: Fluorescence emission of SL-326 in fixed NIH 3T3 mouse fibroblasts grown in media supplemented with 100 µM $ZnSO_4$:10 µM pyrithione for 30 minutes. Excitation of 750 nm was used and emission was collected in separate channels at approximately 20 nm increments.

3.4 Probing Labile Zinc Under Various Growth Conditions

Live cell imaging can be used to visualize the dynamics of the fluorescence response of a probe in real-time. Dynamic imaging thus overcomes many of the limitations experienced with fluorescence microscopy experiments in fixed cells such as a potential re-distribution of the fluorophore upon chemical fixation as well as leakage of the dye due to compromised plasma membrane integrity fixation. Consequently, the following studies involve time-lapse imaging of NIH 3T3 mouse fibroblasts pre-loaded with 10 μM SL-326 under various conditions in order to assess the probe's response in live cells.

Dynamic Imaging of Zn(II) with SL-326

In a series of time-lapse imaging studies, the ability of SL-326 to monitor changes in intracellular labile Zn^{2+} was tested. Specifically, time-lapse sequences were acquired of NIH 3T3 mouse cells pre-loaded with 10 μM SL-326, followed by a perfusion with $ZnSO_4$:pyrithione (100 μM:10 μM), a perfusion with a cell permeable, non-fluorescent Zn(II) chelator, 50 μM TPEN (N,N,N',N'-tetrakis-(2-pyridylmethyl)-ethylenediamine), and finally a second perfusion with $ZnSO_4$:pyrithione (100 μM:10 μM). Prior to perfusion with Zn(II), the ratio images showed a rather uniform with higher ratio intensity throughout the cell cytoplasm and some areas in the perinuclear region (Figure 3.9) with a fluorescence emission ratio of approximately 1.0 (Figure 3.10). Immediately following perfusion with $ZnSO_4$:pyrithione (100 μM:10 μM), SL-326 revealed increased ratios in areas where it was localized (Figure 3.9) and a distinctive increase in its fluorescence emission ratio reaching a maximum of roughly 2.5 (Figure 3.10). The

intracellular selectivity and observed response of SL-326 to Zn(II) was further validated by a reversal of the observed intracellular fluorescence intensity (Figure 3.9) and emission ratio close to the initial value of 1.0 (Figure 3.10) following perfusion with 50 µM TPEN (N,N,N',N'-tetrakis-(2-pyridylmethyl)-ethylenediamine). Furthermore, a second perfusion with $ZnSO_4$:pyrithione (100 µM:10 µM) enabled an almost complete recovery of the previous ratio response (Figure 3.9) and emission ratio value (Figure 3.10) thereby providing additional confirmation of the probe's integrity in a cellular environment.

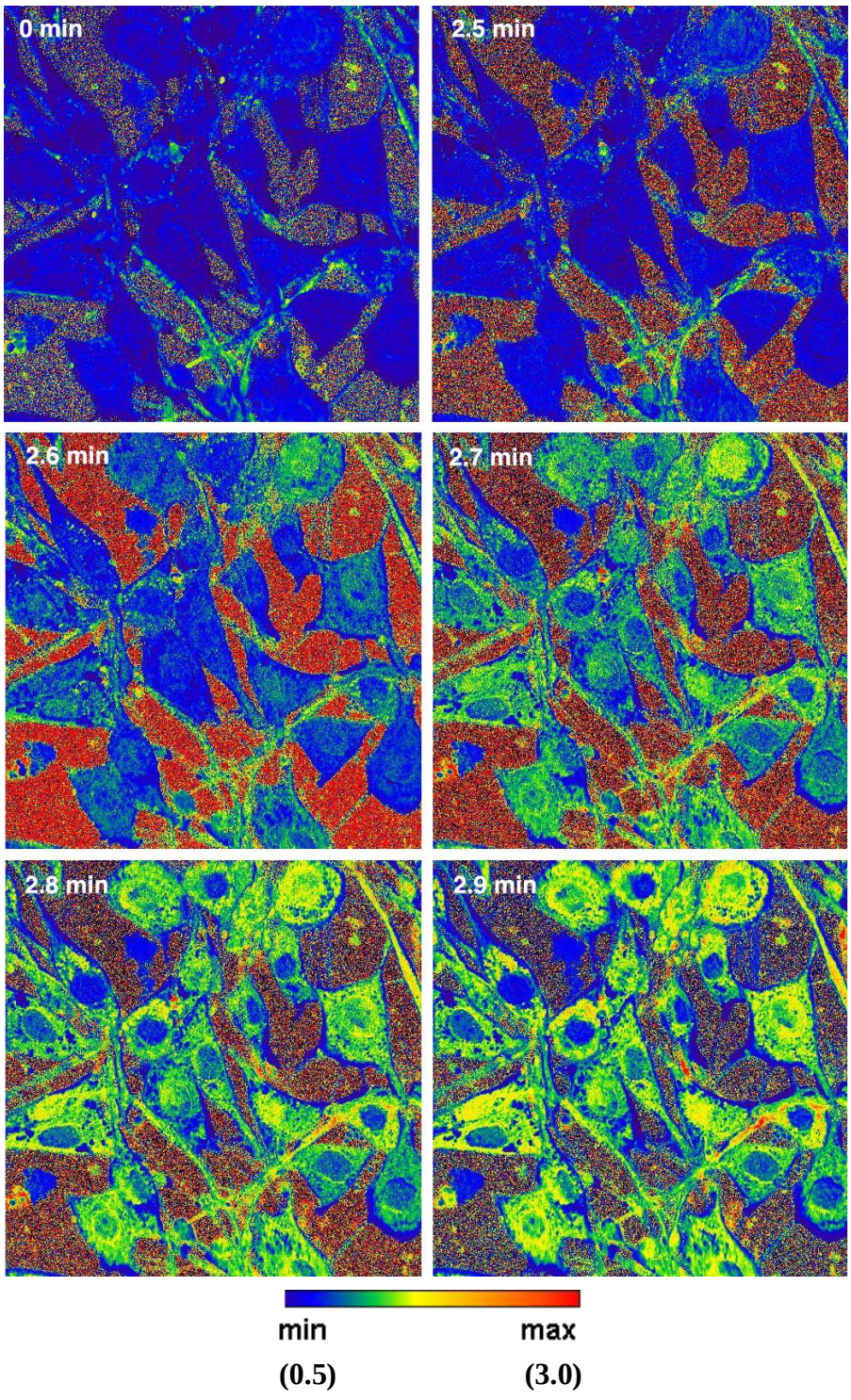

Figure 3.9: Time lapse false color ratio images of 10 µM SL-326 in NIH 3T3 mouse fibroblasts. Cells were perfused with 100 µM $ZnSO_4$:10 µM pyrithione for approximately 1.5 minutes total. The selected images illustrate the ratiometric changes in the fluorescence emission of SL-326 upon exposing the cells to Zn^{2+}. Ratio images by Soars (see text for details).

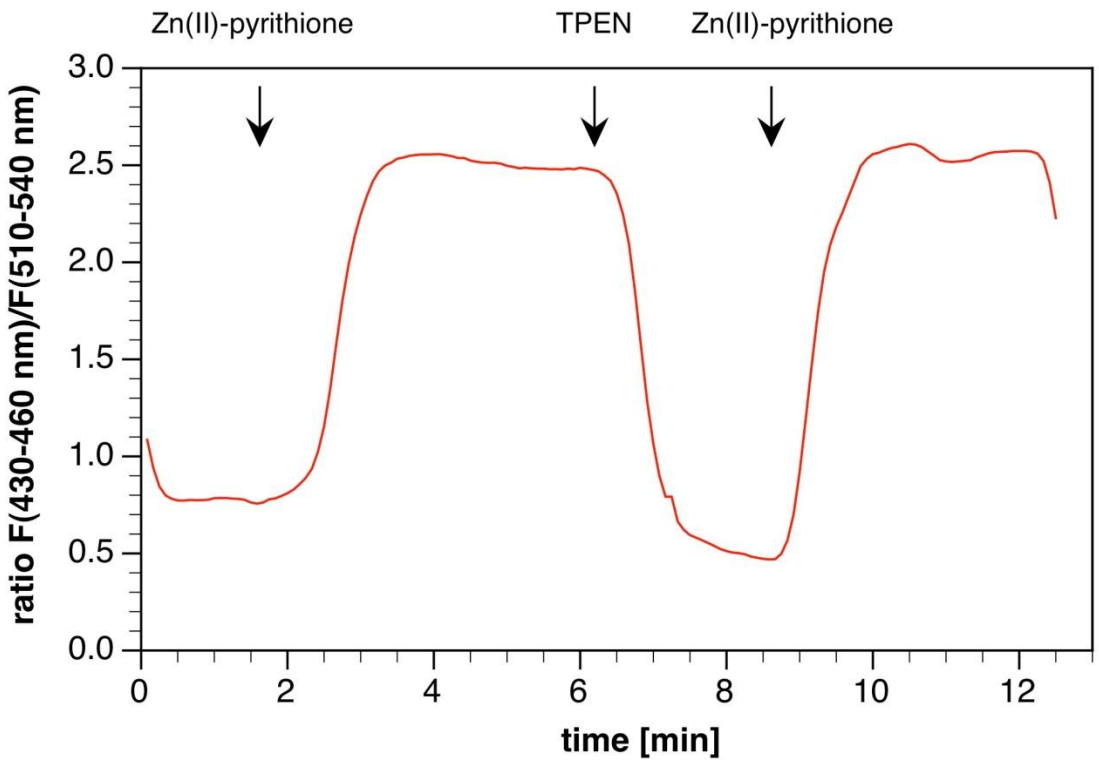

Figure 3.10: Time course dynamics of 10 µM SL-326 in NIH 3T3 mouse fibroblasts. Cells were perfused with 100 µM $ZnSO_4$:10 µM pyrithione followed by perfusion with 50 µM TPEN and a final perfusion with 100 µM $ZnSO_4$:10 µM pyrithione again. The graph illustrates the relative changes in the fluorescence ratio prior to and upon perfusion with Zn^{2+} or TPEN.

Image Processing

Although the intracellular fluorescence signal of SL-326 was distinctive and relatively stable with respect to photobleaching, data acquired via time lapse imaging are inherently noisy due to fast acquisition times and noise amplification in the ratio images. A multivariate statistical optimization analysis for ratiometric signals (SOARS) method was recently developed specifically for elucidating highly resolved spatiotemporal information from ratiometric time-lapse data sets [38]. SOARS has been successfully applied to data sets acquired from imaging ratiometric fluorescent indicators of calcium

spikes in PC-12 cancer cells [38] as well as zebrafish spinal neurons [39] and FRET imaging data from *Drosophila melanogaster* postfeeding larvae [40]. Given its reported successes [38-40], the SOARS method implemented into MATLAB was used for processing time-lapse imaging sequences in order to reduce or eliminate noise interference and to highlight the true performance of SL-326 in living cells.

The SOARS analysis involves: "(1) Standardization and subtraction of fluorescence signals from two wavelengths; (2) Performance of a SVD on the standardized, subtracted data; (3) Statistical selection of eigenimages; (4) Reconstruction of the ratio using only statistically significant eigenimages (a denoised, or optimally filtered, ratio) [38, 39]." Standardization is applied to fluorescence data sets acquired from the same spatial regions and yields two data sets in which pixel time-courses in one data set will be anti-correlated with pixels in the other data set if there is a signal present [38, 39]. A pixel-by-pixel subtraction of the two data sets produces a single data set representing any anti-correlation occurring in the sequence [38, 39]. Singular value decomposition (SVD) on the standardized, subtracted data set generates a series of eigenimages whose time-courses in the standardized data set will be anti-correlated in the presence of signal [38, 39]. In other words, the eigenimages represent weighted masks showing the spatial distribution of anti-correlation in the standardized, subtracted data set [38, 39]. Projection of the statistically significant eigenimages, or those representing any anti-correlation, into the original data set after standardization yields a substantially higher resolved data set with respect to the original data [38, 39].

Prior to data processing with the SOARS method, time-lapse sequences of SL-326 revealed an obvious increase upon addition of $ZnSO_4$:pyr and decrease after application of TPEN in the intracellular fluorescence intensity but well-defined intracellular regions with distinctive responses were not obvious. Applying the SOARS method to the data set enabled the selection and projection of statistically significant eigenimages onto a filtered data set containing only anti-correlated information thereby yielding a significantly less noisy time-lapse sequence.

3.5 Eliminating Potential Artifact Contribution to Probe Response

In vitro studies revealed the probe responds to protonation in way similar to its ratiometric response to Zn(II). Lysosomes are characterized by the presence of a large number of acid hydrolases and play major roles in the digestion and processing of non-native intracellular materials [41, 42]. The intracellular probe distribution appears relatively vesicular, so the probe could be localized within lysosomes and consequently responding to protonation rather than Zn(II).

Lysotracker dyes are often used in biological studies for labeling acidic organelles and compartments in either fixed or live cells. The lysotracker dyes have been particularly utilized for co-localization studies with fluorescent probes for various metals including calcium [43] and Zn(II) [31, 44-47] due to the often punctate fluorescence distribution of these sensors. In order to determine if SL-326 was localized within lysosomes, we used standard fluorescence microscopy to investigate the amount, if any, of co-localization between SL-326 and LysoTracker Red (LTR) in NIH 3T3 mouse fibroblasts. The results suggested a substantial amount of co-localization between SL-

326 and LTR (Figure 3.11), a result consistent with other fluorescent probes selective for Zn(II) including both zinquin [44] and FluoZin-3 [45].

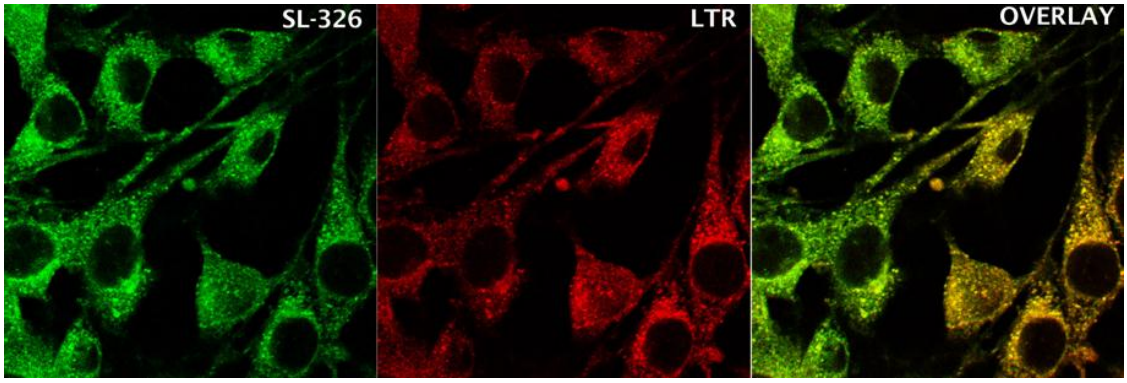

Figure 3.11: Co-localization of SL-326 with intracellular vesicles in NIH 3T3 mouse fibroblasts grown in basal media. (Left) Epifluorescence image of SL-326 excited at 850 nm using a multiphoton confocal laser. (Center) Epifluorescence image of vesicles labeled with LysoTracker Red (LTR) using an excitation of 543 nm. (Right) Overlay image indicating the amount of co-localization between SL-326 and LTR in orange/yellow color.

However, LTR presumably stains all acidic vesicles including both acidic endosomes and lysosomes. Furthermore, the mechanism by which LTR is retained in acidic organelles is not well understood. The significant amount of co-localization observed between SL-326 and LTR may actually be the result of an artifact imposed by LTR.

Lamp-1 (lysosome-associated membrane protein-1) is a major glycoprotein of mouse NIH 3T3 cells that is specifically associated with the lysosomal membrane [48]. In an attempt to unequivocally, establish whether SL-326 localized within lysosomes, co-localization and multicolor fluorescence microscopy were performed with Lamp1-EYFP. In these studies, Lamp1-EYFP was transfected into cells and co-localization with SL-326

was subsequently analyzed via fluorescence microscopy following sufficient expression of Lamp1-EYFP. Transfection rather than immunofluorescence (IF) labeling of Lamp-1 was used to avoid a potential re-distribution of SL-326 that could result from the permeabilization step required for IF preparation. The fluorescence images illustrated only a small amount of co-localization occurred between Lamp1-EYFP and SL-326 (Figure 3.12), unlike that observed with LTR (Figure 3.11). These results strongly imply the probe is localized somewhere other than within lysosomes in NIH 3T3 mouse fibroblasts.

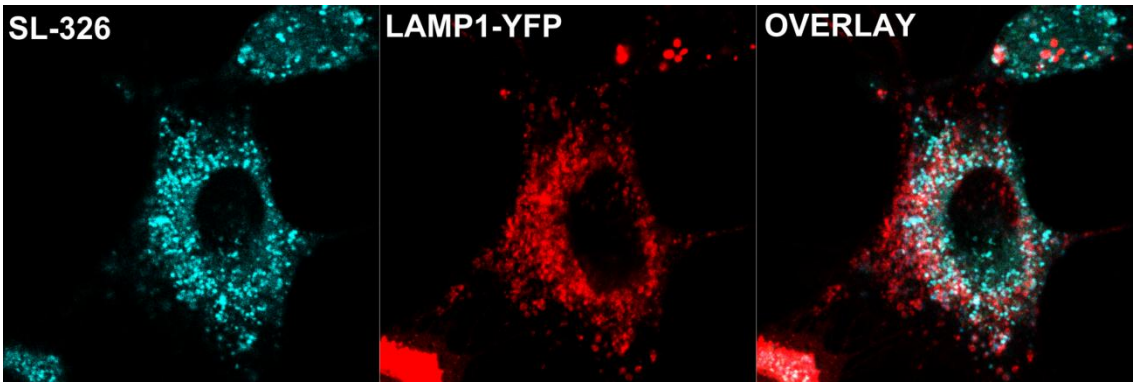

Figure 3.12: Co-localization of SL-326 with acidic vesicles in NIH 3T3 mouse fibroblasts grown in basal media. (Left) Epifluorescence image of SL-326 excited at 850 nm using a multiphoton confocal laser. (Center) Epifluorescence image of acidic vesicles labeled with Lamp1-YFP using an excitation of 488 nm. (Right) Overlay image indicating the amount of co-localization between SL-326 and Lamp1-YFP.

In an effort to determine if the proton gradient generated by the vacuolar-type H^+-ATPase was necessary for the vesicular fluorescence distribution of SL-326, time lapse microscopy was used to follow the potential localization changes occurring for SL-326 upon perfusion with 200 nM bafilomycin. Bafilomycin is a drug that specifically inhibits the vacuolar-type H^+-ATPase responsible for acidifying endosomal compartments

including lysosomes [49]. In these experiments, cells were first perfused with 100 µM Zn^{2+} in order to achieve a maximum ratiometric probe response followed by a perfusion with bafilomycin to investigate specifically whether the observed probe response would be affected. In order to ascertain the selected conditions were sufficient for effectively inhibiting the vacuolar-type H^+-ATPase, the same procedure was executed with LysoTracker Red (LTR) rather than SL-326 as a control.

Time lapse imaging revealed only a negligible reduction in the fluorescence ratio of SL-326 upon treatment of the cells with bafilomycin, (Figure 3.13 and Figure 3.14) while the punctate fluorescence pattern initially observed for LTR was considerably diminished (Figure 3.15 and Figure 3.16). The virtual disappearance of all LTR fluorescence upon bafilomycin treatment firmly established the conditions were appropriate for effectively inhibiting the vacuolar-type H^+-ATPase. The results therefore strongly insinuated that the fluorescence ratio change observed for SL-326 was genuinely from selectively binding to Zn^{2+} rather from an artifact induced by protonation.

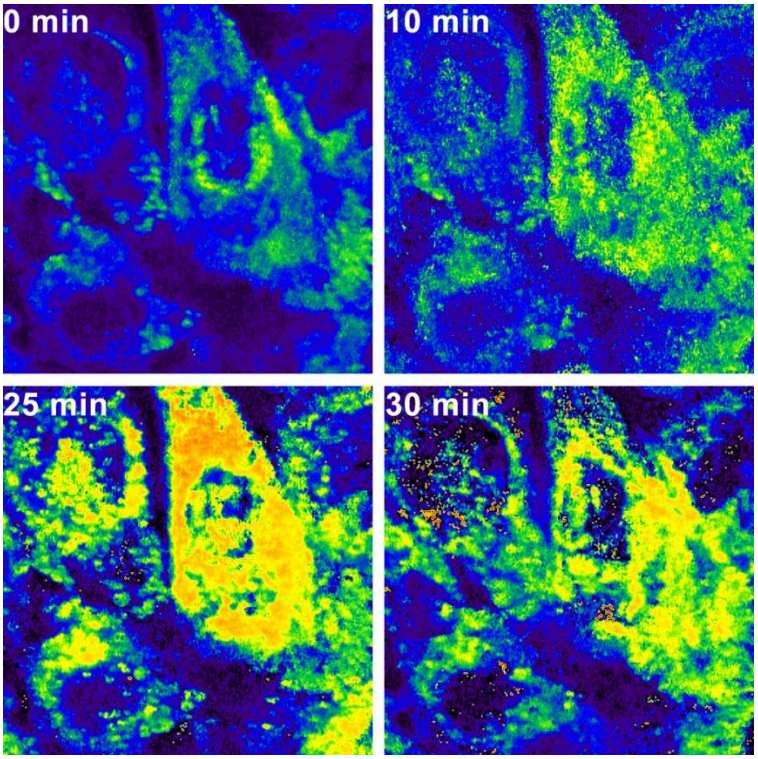

Figure 3.13: Time lapse images of 10 µM SL-326 in NIH 3T3 mouse fibroblasts. Cells were perfused with 100 µM $ZnSO_4$ followed by a perfusion with 400 nM Bafilomycin. The selected images illustrate the ratiometric changes in the fluorescence emission of SL-326 prior to and upon perfusion with 100 µM $ZnSO_4$ and 400 nM Bafilomycin.

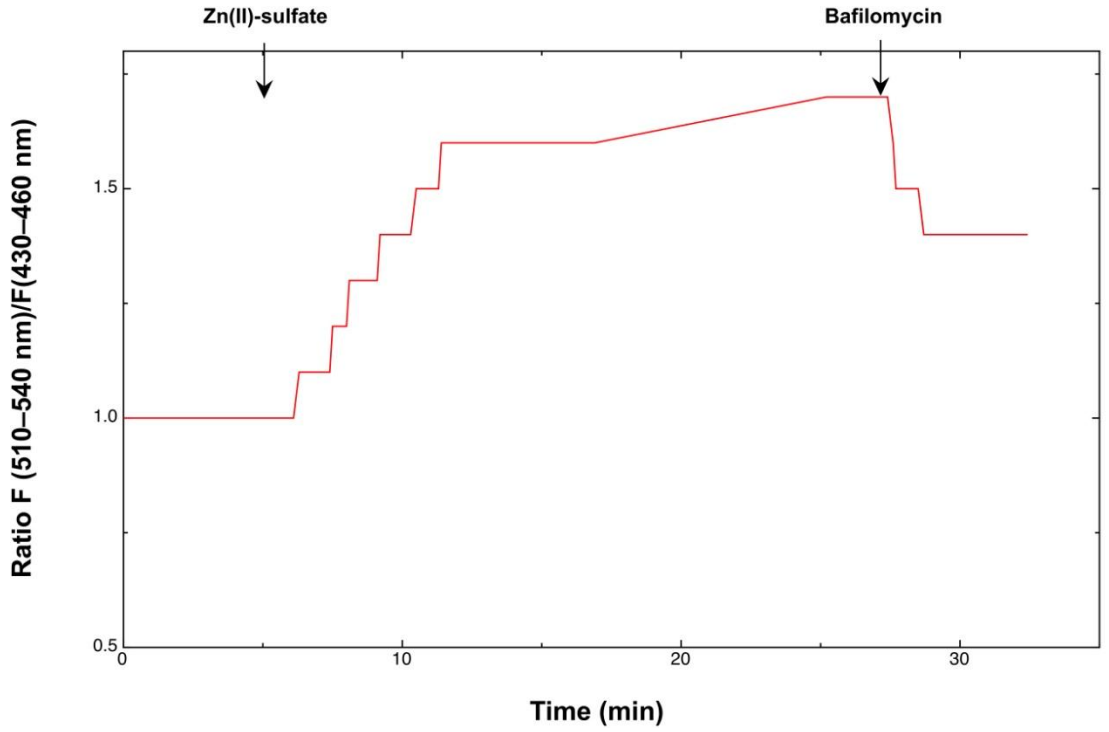

Figure 3.14: Time course dynamics of 10 µM SL-326 in NIH 3T3 mouse fibroblasts. Cells were perfused with 100 µM $ZnSO_4$ followed by a perfusion with 400 nM Bafilomycin. The graph illustrates the relative changes in the fluorescence ratio of SL-326 prior to and upon perfusion with 100 µM $ZnSO_4$ and 400 nM Bafilomycin.

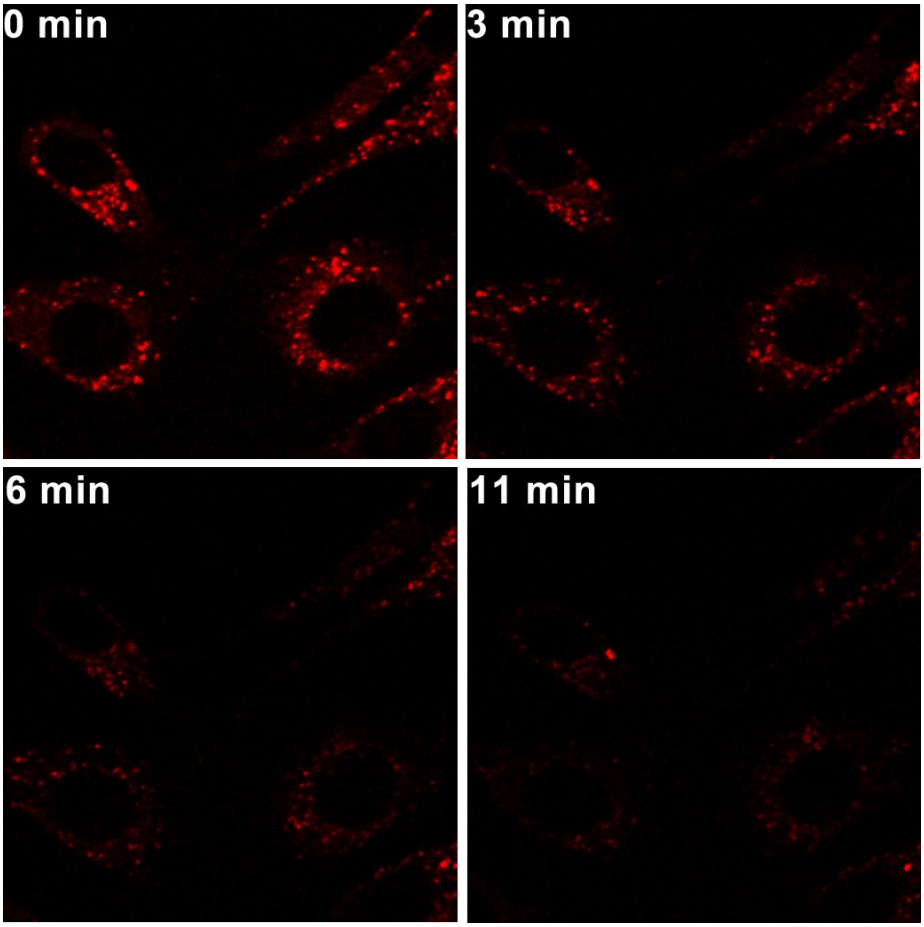

Figure 3.15: Time lapse images of 60 nM LTR in NIH 3T3 mouse fibroblasts. Cells were perfused with 100 µM $ZnSO_4$ followed by a perfusion with 400 nM Bafilomycin. The selected images illustrate the changes in the fluorescence emission intensity of LTR prior to and upon perfusion with 100 µM $ZnSO_4$ and 400 nM Bafilomycin.

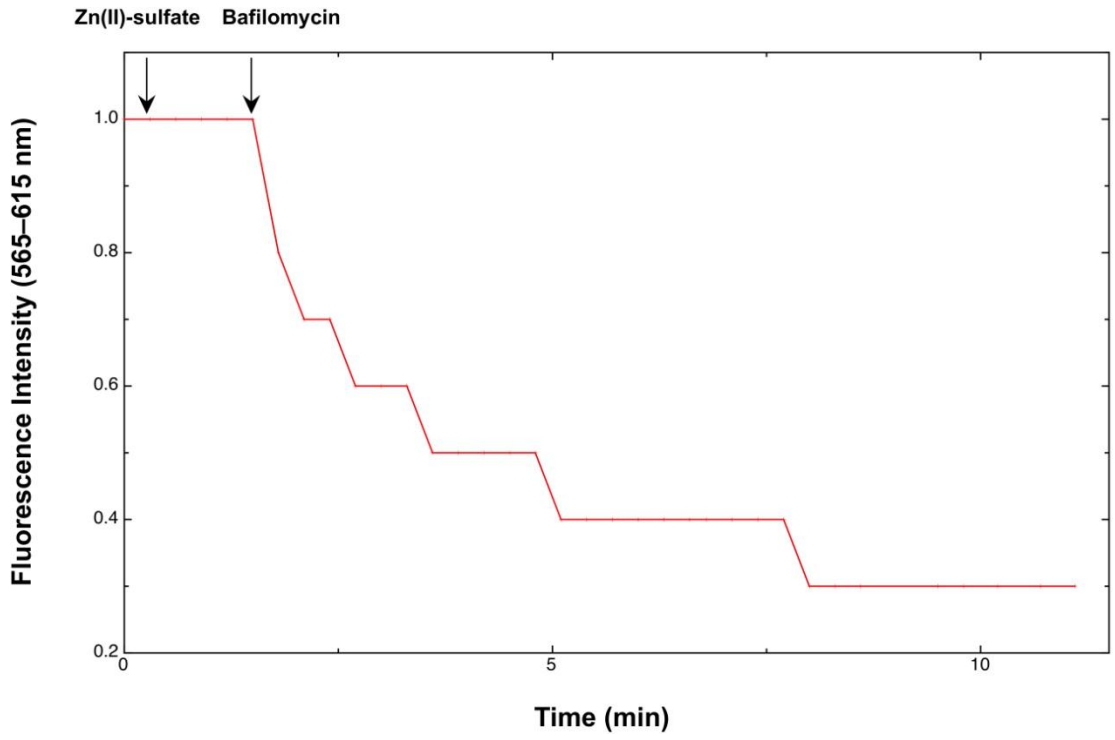

Figure 3.16: Time course dynamics of 60 nM LTR in NIH 3T3 mouse fibroblasts. Cells were perfused with 100 µM $ZnSO_4$ followed by a perfusion with 400 nM Bafilomycin. The graph illustrates the relative changes in the fluorescence emission intensity of LTR prior to and upon perfusion with 100 µM $ZnSO_4$ and 400 nM Bafilomycin.

3.6 Correlative Optical Fluorescence and X-ray Fluorescence Imaging

Preliminary experiments revealed that the fluorescence ratio of SL-326 correlates directly with the availability of Zn(II) in the growth media or with the mobilization of Zn(II) from intracellular storage sites. To determine if the observed increase in the fluorescence ratio was undeniably due to alterations in the intracellular Zn(II) distribution, a series of SXRF scans were performed at the 2-ID-D beam line of the Advanced Photon Source (APS) located at Argonne National Laboratory (ANL).

NIH 3T3 mouse fibroblasts were grown on an electron microscopy (EM) silicon nitride (Si_3N_4) window that was pre-coated with poly-lysine in basal growth media, incubated with 10 μM SL-326 for 10 minutes, washed quickly with 1X-PBS, and fixed for 5 minutes with pre-warmed 3.7% paraformaldehyde (PFA). Following treatment with SL-326 and fixation, cells were imaged by two-photon excitation microscopy (TPEM), air-dried, and shipped to ANL for SXRF imaging. The degree of co-localization between the fluorescence distribution of SL-326 and the SXRF Zn(II) topography was then evaluated for cells grown under basal growth conditions. The TPE images of SL-326 were obtained using an excitation of 850 nm, a wavelength at which the brightness of the free ligand is substantially lower than that of the ligand bound to Zn(II) (*see section **3.3***).

Although a minor distortion of the cellular morphology occurred as a result of the drying step required for SXRF analysis, careful examination of the fluorescence micrographs revealed a substantial amount of co-localization between SL-326 fluorescence and the SXRF Zn(II) distribution (Figure 3.17). Notable co-localization occurred in the perinuclear region and within structurally defined regions in the cytoplasm (Figure 3.17).

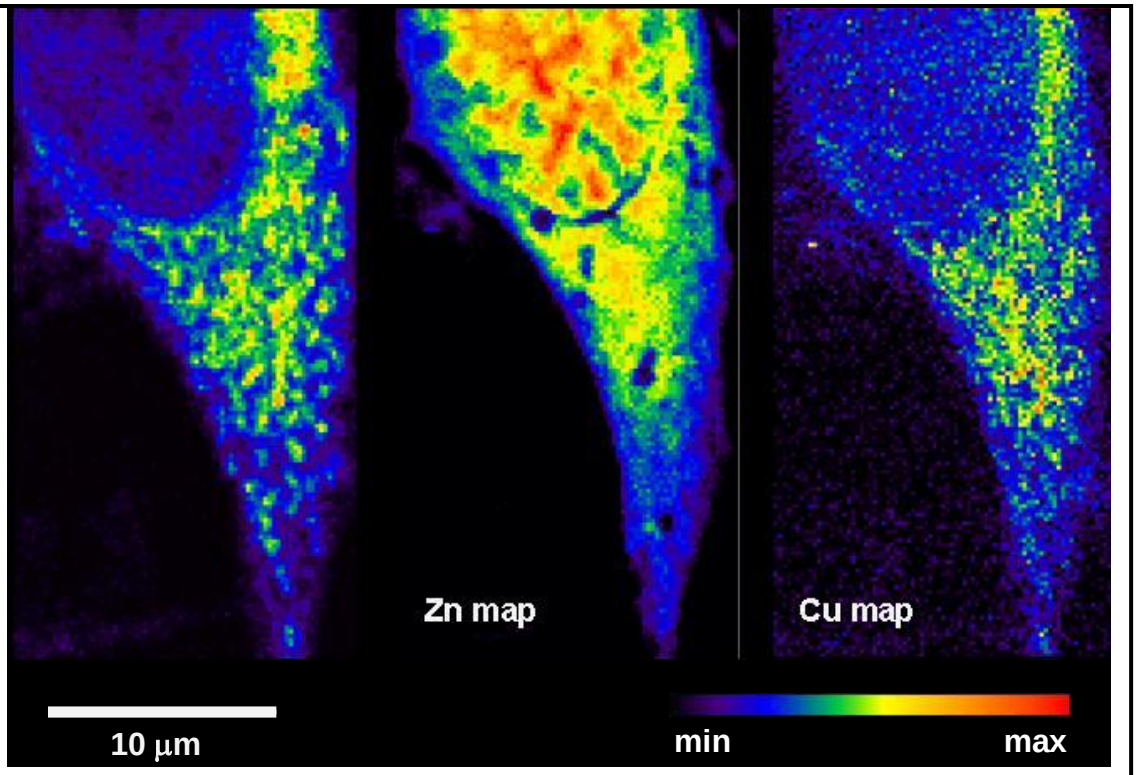

Figure 3.17: False-color micrographs of a single cell grown in basal media and treated with SL-326. (Left) Epifluorescence image acquired with an excitation wavelength of 850 nm. (Center) XRF Zn(II) map. (Right) XRF copper map. The relative intensities increase from blue to red.

Interestingly, comparison of the SL-326 fluorescence pattern with the SXRF copper map revealed striking similarities between the two fluorescence micrographs suggesting that areas of intracellular labile Zn^{2+} pools may also be characterized by the presence of copper pools or copper-bound proteins.

3.7 Investigating Intracellular Probe Localization

In an effort to assess the intracellular localization of SL-326 and consequently reveal information regarding the location of labile Zn(II) pools, a series of co-localization studies were performed with several labels for intracellular organelles and structures.

SL-326 produced a strong fluorescence pattern, which was structural in nature, throughout the cell cytoplasm.

Given the known distribution of the mitochondria throughout the cell cytoplasm (Figure 3.18, center), co-localization of SL-326 and this intracellular organelle, which was labeled with Mito-AcGFP, was performed. Results illustrated a substantial degree of overlap between SL-326 and Mito-AcGFP (Figure 3.18).

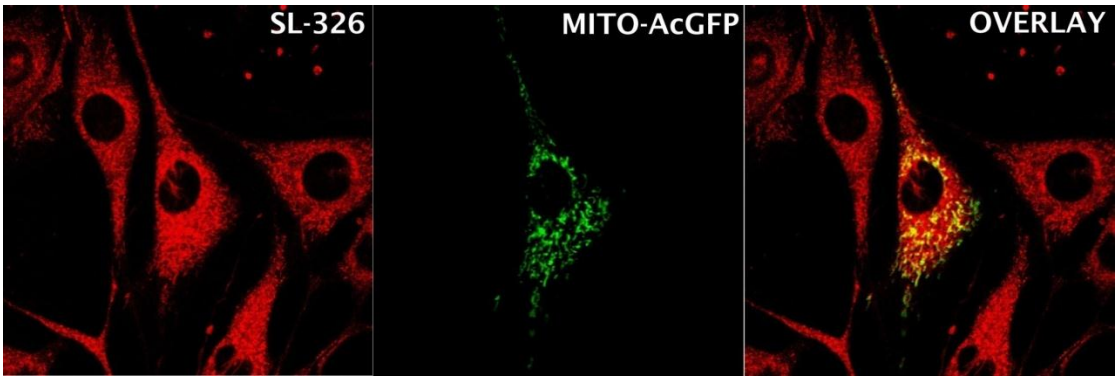

Figure 3.18: Co-localization of SL-326 with the mitochondria in NIH 3T3 mouse fibroblasts grown in basal media. (Left) Epifluorescence image of SL-326 excited at 850 nm using a multiphoton confocal laser. (Center) Epifluorescence image of the mitochondria labeled with Mito-AcGFP using an excitation of 488 nm. (Right) Overlay image indicating the amount of co-localization between SL-326 and Mito-AcGFP.

Given these studies were performed on cells grown under basal conditions, this observation provides support for the existence of labile Zn^{2+} pools in the mitochondria under normal cellular physiology. Evidence for mitochondrial stores of labile Zn(II) was previously provided studies in yeast cells [50] as well as neuronal mitochondria [51], also performed under basal growth conditions.

Since a considerable amount of the probe fluorescence was in areas clearly distinct from regions with mitochondria, another co-localization study was performed between SL-326 and the Endoplasmic Reticulum (ER), which is also localized throughout the cell cytoplasm (Figure 3.19, center). In this experiment, the fluorescence from SL-326 was correlated with fluorescence from a cell-permeable dye, ER-Tracker Green, designed for specifically labeling the ER in cells. Similar to the mitochondria, SL-326 fluorescence correlated well with areas containing ER structures as indicated by the yellow color in the overlay image (Figure 3.19), thereby alsosuggesting the existence of labile Zn(II) pools within the endoplasmic reticulum.

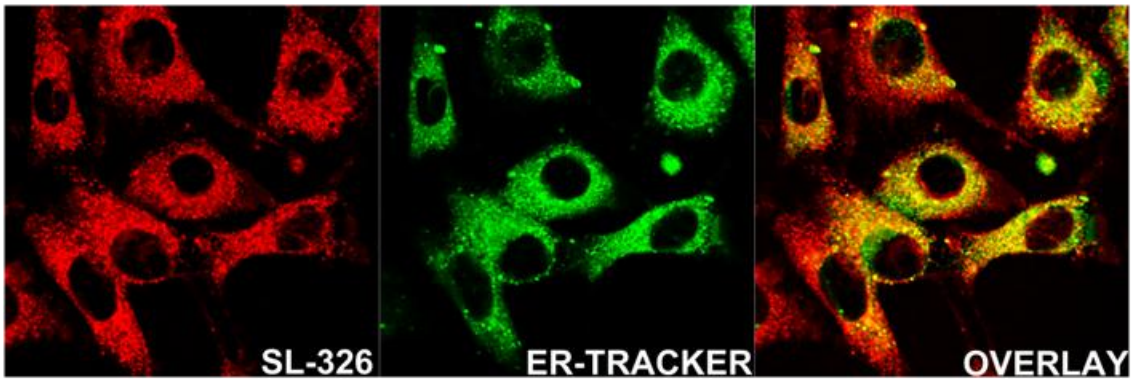

Figure 3.19: Co-localization of SL-326 with the endoplasmic reticulum (ER) in NIH 3T3 mouse fibroblasts grown in basal media. (Left) Epifluorescence image of SL-326 excited at 850 nm using a multiphoton confocal laser. (Center) Epifluorescence image of the mitochondria labeled with ER-Tracker Green using an excitation of 488 nm. (Right) Overlay image indicating the amount of co-localization between SL-326 and ER-Tracker Green.

The presence of labile Zn(II) within the ER was previously reported in a study illustrating a growth factor stimulated release of Zn^{2+} from the ER in mast cells [52] as well as in a report suggesting a role for the Zn(II) transporter, ZIP7, in releasing Zn^{2+} from the ER in MCF-7 breast cancer cells [19].

In another study, SL-326 co-localized slightly with Rab5 associated endosomes labeled with Rab5-mRFP (Figure 3.20).

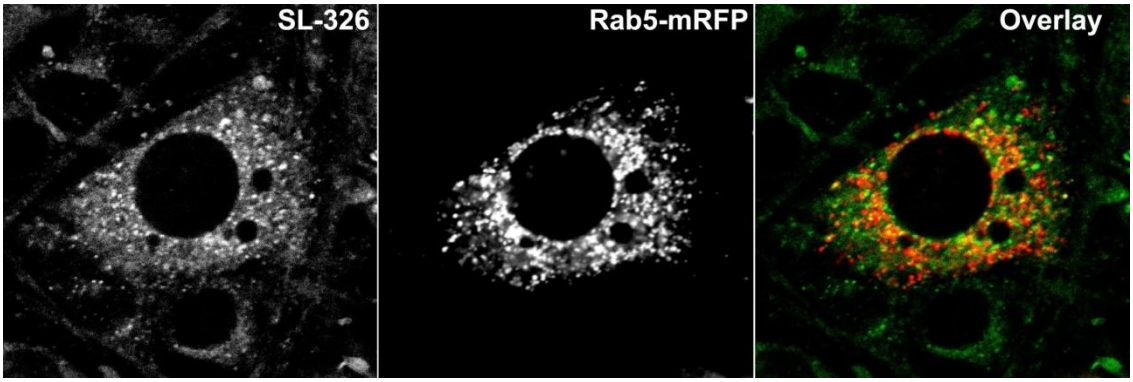

Figure 3.20: Co-localization of SL-326 with the Rab5 vesicles in NIH 3T3 mouse fibroblasts grown in basal media. (Left) Epifluorescence image of SL-326 excited at 850 nm using a multiphoton confocal laser. (Center) Epifluorescence image of the Rab5 vesicles labeled with Rab5-mRFP using an excitation of 543 nm. (Right) Overlay image indicating the amount of co-localization between SL-326 and Rab5-mRFP.

Although labile Zn(II) pools have not previously been directly linked with Rab5 containing vesicles, Zn(II) was previously reported to be essential for the fusion of endosomes, an event required for the transport of molecules along the endocytic and secretory pathways [53].

3.8 Dynamic Imaging of Intracellular Labile Zinc

Intracellular oxidative or nitrosative stress conditions are known to cause disturbances in normal intracellular Zn(II) homeostatic pathways. For instance, treatment of cells with low levels (< 500 μM) hydrogen peroxide (H_2O_2) was found to induce a cytoplasmic release of labile Zn^{2+} ions, while high levels of H_2O_2 (1 mM) led to labile Zn^{2+} release from the nucleus [54-56]. Moreover, another study reported an H_2O_2

stimulated release of Zn^{2+} intracellular metallothionein (MT) ligands [57]. Given the aforementioned reports of H_2O_2 induced alterations in intracellular Zn2+ homeostasis, dynamic imaging was employed for following the ratiometric fluorescence change(s) for SL-326 in NIH 3T3 mouse cells perfused with 100 µM H_2O_2.

In these experiments, cells were pre-loaded with 10 µM SL-326 and mounted into the perfusion chamber for time lapse imaging. Following an initial time-lapse image acquisition series of SL-326, NIH 3T3 mouse fibroblasts were perfused with 100 µM H_2O_2 for approximately five minutes. Similar to perfusion studies with 100 µM Zn^{2+}, ratio images almost instantaneously showed a dramatic increase in the fluorescence emission ratio upon exposing the cells to H_2O_2. The fluorescence ratio continued to increase until the full amount of H_2O_2 solution was perfused after which the fluorescence ratio eventually reached a maximum of about 2.0 (Figure 3.21 and Figure 3.22).

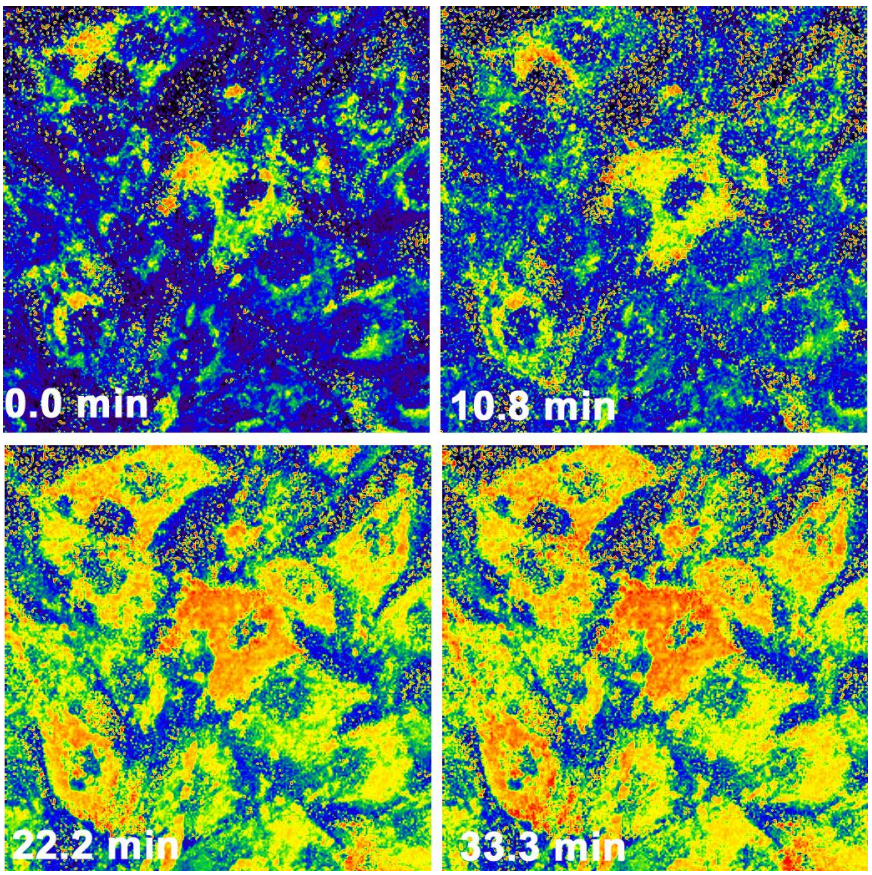

Figure 3.21: Time lapse fluorescence ratio images of 10 µM SL-326 in NIH 3T3 mouse fibroblasts. Cells were perfused with 100 µM H_2O_2 for approximately 5 minutes. The selected images illustrate the ratiometric changes in the fluorescence emission of SL-326 prior to and upon exposing the cells to 100 µM H_2O_2.

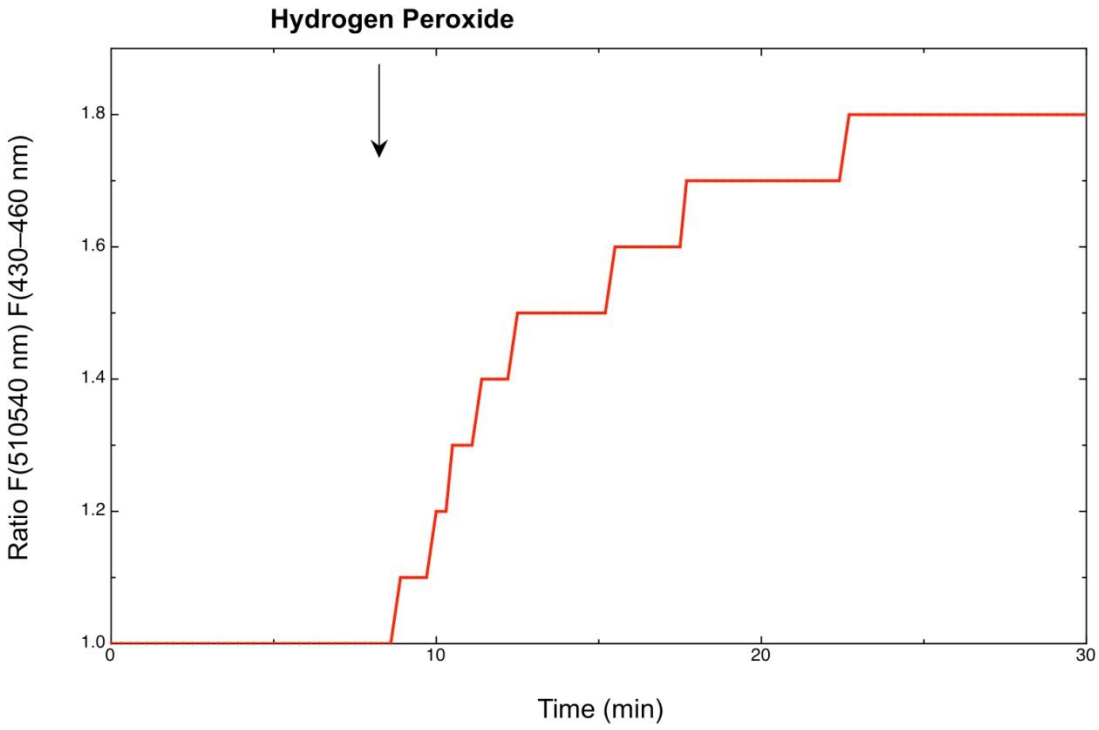

Figure 3.22: Time course dynamics of 10 µM SL-326 in NIH 3T3 mouse fibroblasts. Cells were perfused with 100 µM H_2O_2. The graph illustrates the relative changes in the fluorescence ratio prior to and upon perfusion with 100 µM H_2O_2.

The observed increase in the fluorescence ratio of SL-326 is consistent with previous reports, which revealed that exposure of cells to low levels (<500 µM) of H_2O_2 stimulated a mobilization of Zn^{2+} ions from cytoplasmic storage sites [54-56]. Thus, the present data provide additional evidence for the existence of cytoplasmic stores containing exchangeable Zn^{2+} ions.

3.9 Summary and Conclusions

A Zn(II)-selective, ratiometric fluorescent probe was used to assess the intracellular localization and dynamic behavior of labile Zn(II) pools. Co-localization experiments revealed the presence of labile Zn(II) pools within the mitochondria, ER, and

associated with Rab5 vesicles. SXRF imaging revealed a strong correlation between the intracellular XRF Zn(II) distribution and the probe fluorescence, thus confirming the integrity of the probe. Additionally, dynamic imaging with SL-326 revealed a significant increase in the fluorescence ratio emission upon addition of Zn(II) to the extracellular environment and upon perturbation of the cellular redox status by the addition of H_2O_2 to the growth media.

3.10 Materials and Methods

Cell Culture and Reagents

NIH 3T3 mouse cells were cultured in Dulbecco's modified Eagle's medium (DMEM) containing 10% bovine serum and supplemented with 200 μM L-glutamine. The ratiometric fluorescent probe for Zn(II), SL-326, was synthesized and characterized in vitro by Dr. S. Sumalekshmy [*unpublished results*].

In Situ Characterization of SL-326 and Two-Photon Excitation Microscopy (TPEM)

For the intracellular, optical characterization of SL-326, NIH 3T3 mouse cells were grown on coverslips to 50-70% confluency, incubated with 10 μM SL-326 in growth media for 10 min at 37˚C in a 5% CO_2 atmosphere, washed with PBS, and either received no additional treatment or were supplemented with media containing 100 μM ZnSO4:10 μM pyrithione for 10 min at 37˚C in a 5% CO_2 atmosphere and washed with PBS. The Zn(II) supplemented samples either received no additional treatment or were

treated with 50 μM TPEN (N,N,N',N'-tetrakis-(2-pyridylmethyl)-ethylenediamine), a cell-permeable transition metal chelator. Following their designated treatment, samples were fixed with a pre-warmed 3.7% paraformaldehyde (PFA) solution for 5 min prior to mounting the coverslips onto slides with ProLong Antifade (Invitrogen) mounting medium.

The Meta detector of a Zeiss LSM Confocal/NLO 510 microscope equipped with Argon 488, Krypton 568, HeNe 633, and NLO/UV 800 lasers and fitted with a 64X oil immersion objective was used to collect a lamba fluorescence emission scan in separate emission channels at 20 nm intervals from 415-587 nm. The NLO/UV laser was tuned to a wavelength of 750 nm for excitation of SL-326 in cells either grown under basal conditions or cells additionally treated with 100 μM ZnSO4:10 μM pyrithione (pyr) following pre-loading with 10 μM SL-326 for 10 minutes at 37˚C.

Time-Lapse Microscopy

For live cell imaging experiments, NIH 3T3 mouse fibroblasts seeded onto 60 mm round coverslips (Bioptechs) were pre-incubated with 10 μM SL-326 for 10 min at 37˚C, washed one time with pre-warmed 1X-PBS, and mounted into an F2 flow chamber (Bioptechs), which was subsequently filled with approximately 1 mL of pre-warmed HEPES (25 mM) buffered DMEM without sodium pyruvate. A system controller for FCS2 and FCS3 closed chambers (Bioptechs) was used to maintain the cells at 37˚C and an objective heater controller was used to maintain the objective temperature at 37˚C.

For two-photon excitation microscopy (TPEM), image acquisition was performed with a Zeiss LSM Confocal/NLO 510 inverted microscope equipped with a

64X oil immersion objective. A TPE wavelength of 750 nm was used for excitation of SL-326 and emission was collected using the META detector with two separate emission channels of 415-437 nm (free SL-326) and 480-501 nm (Zn(II)-bound SL-326). Images were collected at a pixel resolution of 1024x1024, a pixel dwell time of 1.6 µs, a four-fold frame averaging, and a 12-bit pixel depth.

SL-326 Resoponse to Cellular Uptake of Zn(II)

For time-lapse imaging of SL-326 in a varying Zn(II) environment, an initial image sequence was acquired with intervals of five seconds, which was not changed over the course of the experiment. Cells were perfused with 100 µM $ZnSO_4$:10 µM pyrithione (pyr) in HEPES (25 mM) buffered DMEM without sodium pyruvate over a period of 10 min and images were acquired until the fluorescence ratio emission reached a maximum and plateaued. Cells were subsequently perfused with 50 µM TPEN (N,N,N',N'-tetrakis-(2-pyridylmethyl)-ethylenediamine), a cell-permeable transition metal chelator, in HEPES (25 mM) buffered DMEM without sodium pyruvate over a ten minute period and finally perfused again with 100 µM $ZnSO_4$:10 µM pyr over ten minutes.

Bafilomycin Treatment

For time-lapse imaging of SL-326 prior to and upon perfusion with bafilomycin, an initial image sequence was acquired. Cells were then perfused with 100 µM $ZnSO_4$ over a period of 10 min and images were acquired until the fluorescence ratio emission reached a maximum and plateaued. Cells were subsequently perfused with 400 nM bafilomycin in HEPES (25 mM) buffered DMEM without sodium pyruvate over a ten

minute period and images were acquired for approximately 20 min. The same time lapse experiment was performed with 60 nM LysoTracker-Red, which was pre-loaded into NIH 3T3 mouse fibroblasts for 20 min.

H_2O_2 Stimulation

For time-lapse imaging of SL-326 prior to and upon perfusion with H_2O_2, an initial image sequence was acquired. Cells were then perfused with 100 µM H_2O_2 in HEPES (25 mM) buffered DMEM without sodium pyruvate over a period of 10 min and images were acquired until the fluorescence ratio emission reached a steady maximum.

Image Processing

Time-lapse imaging sequences were processed with the SOARS (Statistical Optimization for the Analysis of Ratiometric Signals, Version 1.1) [38, 39] using Matlab (Mathworks; http://www.engr.uga.edu/research/groups/atslab/software.html). The quantitative image analysis software package, Image J [58], was used to analyze the change in the fluorescence emission ratio of SL-326 over time, and the ratio values and their respective time points were imported into ProFit for graphing the data set.

Synchrotron X-ray Fluorescence (SXRF)

For sample preparation, cells were cultured directly onto a silicon nitride electron microscopy (EM) window, which was placed into an individual well of a 6-well plate and pre-coated with a 0.01% poly-L-lysine solution (Sigma-Aldrich) for 15 min. Following a

10 min incubation with 10 µM SL-326 as described above, cells were quickly washed with 1X-PBS, fixed with 3.7% PFA for 5 min, washed thoroughly, and imaged with TPEM using an excitation of 850 nm in order to predominantly highlight the localization of the Zn(II)-bound ligand. Immediately after fluorescence imaging, samples were prepared for SXRF analysis as previously described [59]. Briefly, the samples were washed quickly with 1X-PBS, rinsed twice with sterile dH2O, and washed quickly isotonic ammonium acetate (Sigma-Aldrich, 0.1 M solution in sterile dH2O) two times. Finally, samples were air-dried overnight in a covered, sterile cell culture dish.

Synchrotron-based x-ray fluorescence (SXRF) microscopy was performed at beamline 2-ID-D of the Advanced Photon Source at the Argonne National Laboratory. Incident x-rays of 10 keV (1 eV + 1.602 x 1019 J) energy were chosen to excite elements from P to Zn. A Fresnel zone plate focused the x-ray beam to a spot size of 0.2 x 0.2 µm2 on the specimen, which was raster-scanned. XRF from the specimen was captured with an energy dispersive Ge detector. Spectral analysis of the fluorescence spectrum of each raster pixel then provided spatial images for each element. As mentioned earlier, at the hard x-ray regime, biological cells do not cause significant absorption or beam spreading, hence no specimen thinning is required, and the fluorescence image represents a two-dimensional projection of the volumetric distribution for each element.

Localization Studies

The pMito-AcGFP plasmid was purchased from Clontech while pLamp1-EYFP (Addgene plasmid 1816) [60] and pRab5-mRFP (Addgene plasmid 14437) [61] were acquired through Addgene. NIH 3T3 mouse fibroblasts were seeded onto glass

coverslips in individual wells of a 6-well culture dish and upon reaching a confluency of roughly 40-50%, cells were transfected with 1 µg/mL of an individual plasmid using the Turbofect (Fermentas) transfection reagent at ratio of 3:1 with the plasmid DNA. Maximum expression was achieved approximately 24-36 h post-transfection at which point the samples were loaded with 10 µM SL-326 for 5 min at 37˚C or left un-treated for imaging controls. After a thorough wash with pre-warmed 1X-PBS, samples were subsequently fixed with pre-warmed 3.7% PFA for 5 min, washed with 1X-PBS, and mounted onto slides with ProLong Antifade (Invitrogen) mounting medium.

For co-localization of SL-326 with fluorescent probes, cells were incubated with 10 µM SL-326 in basal growth media for 10 minutes at 37˚C, washed with pre-warmed 1X-PBS, and incubated with either 60 nM LysoTracker Red (Invitrogen) for 10 min or 5 µM ER-Tracker Green (Invitrogen) for 25 min at 37˚C. After incubations with the specified fluorescent probe, cells were thoroughly washed with pre-warmed 1X-PBS and coverslips were mounted onto slides with pre-warmed Fluoromount-G (SouthernBiotech) prior to imaging.

Images were acquired using a Zeiss LSM Confocal/NLO 510 microscope equipped with Argon 488, Krypton 568, HeNe 633, and NLO/UV 800 lasers and fitted with a 64X oil immersion objective. For multichannel imaging, individual fluorophores were imaged sequentially to eliminate crosstalk between channels and images were acquired at a 1024 x 1024 pixel resolution with a frame averaging of four. Images were subsequently processed with Adobe Photoshop CS2.

3.11 Literature Cited

1. Vahrenkamp, H. (2007) Why does nature use zinc - a personal view. *Dalton Trans.*, 4751-4759.

2. Maret, W., & Li, Y. (2009) Coordination dynamics of zinc in proteins. *Chem. Rev.* **109**, 4682-4707.

3. Cousins, R. J., Liuzzi, J. P., & Lichten, L. A. (2006) Mammalian zinc transport, trafficking, and signals. *J. Biol. Chem.* **281**, 24085-24089.

4. Maret, W. (2009) Molecular aspects of human cellular zinc homeostasis: Redox control of zinc potentials and zinc signals. *Biometals* **22**, 149-157.

5. Murakami, M., & Hirano, T. (2008) Intracellular zinc homeostasis and zinc signaling. *Cancer Sci.* **99**, 1515-1522.

6. Prasad, T., & Kundu, M. S. (1995) Serum igg and igm responses to sheep red blood cells (srbc) in weaned calves fed milk supplemented with zn and cu. *Nutrition* **11**, 712-715.

7. Truong-Tran, A. Q., Ho, L. H., Chai, F., & Zalewski, P. D. (2000) Cellular zinc fluxes and the regulation of apoptosis/gene-directed cell death. *J. Nutr.* **130**, 1459S-1466S.

8. Truong-Tran, A. Q., Carter, J., Ruffin, R. E., & Zalewski, P. D. (2001) The role of zinc in caspase activation and apoptotic cell death. *Biometals* **14**, 315-330.

9. Beyersmann, D., & Haase, H. (2001) Functions of zinc in signaling, proliferation and differentiation of mammalian cells. *Biometals* **14**, 331-341.

10. Haase, H., & Maret, W. (2003) Intracellular zinc fluctuations modulate protein tyrosine phosphatase activity in insulin/insulin-like growth factor-1 signaling. *Exp. Cell Res.* **291**, 289-298.

11. Haase, H., & Rink, L. (2007) Signal transduction in monocytes: The role of zinc ions. *Biometals* **20**, 579-585.

12. Haase, H., & Rink, L. (2009) Functional significance of zinc-related signaling pathways in immune cells. *Annu. Rev. Nutr.* **29**, 133-152.

13. Takeda, A., & Tamano, H. (2009) Insight into zinc signaling from dietary zinc deficiency. *Brain Res. Rev.* **62**, 33-44.

14. Tuerk, M. J., & Fazel, N. (2009) Zinc deficiency. *Curr. Opin. Gastroenterol.* **25**, 136-143.

15. Jansen, J., Karges, W., & Rink, L. (2009) Zinc and diabetes - clinical links and molecular mechanisms. *J. Nutr. Biochem.* **20**, 399-417.

16. Mocchegiani, E., Giacconi, R., & Malavolta, M. (2008) Zinc signalling and subcellular distribution: Emerging targets in type 2 diabetes. *Trends Mol. Med* **14**, 419-428.

17. Kambe, T., Yamaguchi-Iwai, Y., Sasaki, R., & Nagao, M. (2004) Overview of mammalian zinc transporters. *Cell. Mol. Life Sci.* **61**, 49-68.

18. Lichten, L. A., & Cousins, R. J. (2009) Mammalian zinc transporters: Nutritional and physiologic regulation. *Annu. Rev. Nutr.* **29**, 153-176.

19. Hogstrand, C., Kille, P., Nicholson, R. I., & Taylor, K. M. (2009) Zinc transporters and cancer: A potential role for zip7 as a hub for tyrosine kinase activation. *Trends Mol. Med* **15**, 101-111.

20. Sekler, I., Sensi, S. L., Hershfinkel, M., & Silverman, W. F. (2007) Mechanism and regulation of cellular zinc transport. *Mol. Med.* **13**, 337-343.

21. Mcmahon, R. J., & Cousins, R. J. (1998) Mammalian zinc transporters. *J. Nutr.* **128**, 667-670.

22. Eide, D. J. (2006) Zinc transporters and the cellular trafficking of zinc. *Biochim. Biophys. Acta-Mol. Cell Res.* **1763**, 711-722.

23. Krezel, A., & Maret, W. (2007) Dual nanomolar and picomolar zn(ii) binding properties of metallothionein. *J. Am. Chem. Soc.* **129**, 10911-10921.

24. Kikuchi, K., Komatsu, K., & Nagano, T. (2004) Zinc sensing for cellular application. *Curr. Opin. Chem. Biol.* **8**, 182-191.

25. Dittmer, P. J., Miranda, J. G., Gorski, J. A., & Palmer, A. E. (2009) Genetically encoded sensors to elucidate spatial distribution of cellular zinc. *J. Biol. Chem.* **284**, 16289-16297.

26. Vinkenborg, J. L., Nicolson, T. J., Bellomo, E. A., Koay, M. S., Rutter, G. A., & Merkx, M. (2009) Genetically encoded fret sensors to monitor intracellular zn2+ homeostasis. *Nat. Methods* **6**, 737-U710.

27. Dunn, K. W., Mayor, S., Myers, J. N., & Maxfield, F. R. (1994) Applications of ratio fluorescence microscopy in the study of cell physiology. *Faseb J.* **8**, 573-582.

28. Grynkiewicz, G., Poenie, M., & Tsien, R. Y. (1985) A new generation of ca-2+ indicators with greatly improved fluorescence properties. *J. Biol. Chem.* **260**, 3440-3450.

29. Fahrni, C. J. (2009) Fluorescent probes and labels for cellular imaging. *Chimia* **63**, 714-720.

30. Tsien, R. Y., & Poenie, M. (1986) Fluorescence ratio imaging - a new window into intracellular ionic signaling. *Trends Biochem.Sci.* **11**, 450-455.

31. Kim, H. M., & Cho, B. R. (2009) Two-photon probes for intracellular free metal ions, acidic vesicles, and lipid rafts in live tissues. *Accounts Chem. Res.* **42**, 863-872.

32. Zipfel, W. R., Williams, R. M., & Webb, W. W. (2003) Nonlinear magic: Multiphoton microscopy in the biosciences. *Nat. Biotechnol.* **21**, 1368-1376.

33. Niggli, E., & Egger, M. (2004) Applications of multi-photon microscopy in cell physiology. *Front. Biosci.* **9**, 1598-1610.

34. Helmchen, F., & Denk, W. (2005) Deep tissue two-photon microscopy. *Nat. Methods* **2**, 932-940.

35. Kerr, J. N. D., & Denk, W. (2008) Imaging in vivo: Watching the brain in action. *Nat. Rev. Neurosci.* **9**, 195-205.

36. Pawlicki, M., Collins, H. A., Denning, R. G., & Anderson, H. L. (2009) Two-photon absorption and the design of two-photon dyes. *Angew. Chem.-Int. Edit.* **48**, 3244-3266.

37. Sumalekshmy, S., Henary, M. M., Siegel, N., Lawson, P. V., Wu, Y., Schmidt, K., et al. (2007) Design of emission ratiometric metal-ion sensors with enhanced two-photon cross section and brightness. *J. Am. Chem. Soc.* **129**, 11888-+.

38. Broder, J., Majumder, A., Porter, E., Srinivasamoorthy, G., Keith, C., Lauderdale, J., et al. (2007) Estimating weak ratiometric signals in imaging data. I. Dual-channel data. *J. Opt. Soc. Am. A-Opt. Image Sci. Vis.* **24**, 2921-2931.

39. Fan, X., Majumder, A., Reagin, S. S., Porter, E. L., Sornborger, A. T., Keith, C. H., et al. (2007) New statistical methods enhance imaging of cameleon fluorescence resonance energy transfer in cultured zebrafish spinal neurons. *J. Biomed. Opt.* **12**, 7.

40. Xu, J., Sornborger, A. T., Lee, J. K., & Shen, P. (2008) Drosophila trpa channel modulates sugar-stimulated neural excitation, avoidance and social response. *Nat. Neurosci.* **11**, 676-682.

41. Bainton, D. F. (1981) The discovery of lysosomes. *J. Cell Biol.* **91**, S66-S76.

42. Deduve, C. (1983) Lysosomes revisited. *Eur. J. Biochem.* **137**, 391-397.

43. Haller, T., Dietl, P., Deetjen, P., & Volkl, H. (1996) The lysosomal compartment as intracellular calcium store in mdck cells: A possible involvement in insp(3)-mediated ca2+ release. *Cell Calcium* **19**, 157-165.

44. Palmiter, R. D., Cole, T. B., & Findley, S. D. (1996) Znt-2, a mammalian protein that confers resistance to zinc by facilitating vesicular sequestration. *Embo J.* **15**, 1784-1791.

45. Muylle, F. A. R., Adriaensen, D., De Coen, W., Timmermans, J. P., & Blust, R. (2006) Tracing of labile zinc in live fish hepatocytes using fluozin-3. *Biometals* **19**, 437-450.

46. Hwang, J. J., Lee, S. J., Kim, T. Y., Cho, J. H., & Koh, J. Y. (2008) Zinc and 4-hydroxy-2-nonenal mediate lysosomal membrane permeabilization induced by h2o2 in cultured hippocampal neurons. *J. Neurosci.* **28**, 3114-3122.

47. Chung, H., Yoon, Y. H., Hwang, J. J., Cho, K. S., Koh, J. Y., & Kim, J. G. (2009) Ethambutol-induced toxicity is mediated by zinc and lysosomal membrane permeabilization in cultured retinal cells. *Toxicol. Appl. Pharmacol.* **235**, 163-170.

48. Chen, J. W., Pan, W., Dsouza, M. P., & August, J. T. (1985) Lysosome-associated membrane-proteins - characterization of lamp-1 of macrophage-p388 and mouse embryo 3t3 cultured-cells. *Arch. Biochem. Biophys.* **239**, 574-586.

49. Yoshimori, T., Yamamoto, A., Moriyama, Y., Futai, M., & Tashiro, Y. (1991) Bafilomycin-a1, a specific inhibitor of vacuolar-type h+-atpase, inhibits acidification and protein-degradation in lysosomes of cultured-cells. *J. Biol. Chem.* **266**, 17707-17712.

50. Pierrel, F., Cobine, P. A., & Winge, D. R. (2007) Metal ion availability in mitochondria. *Biometals* **20**, 675-682.

51. Sensi, S. L., Ton-That, D., Sullivan, P. G., Jonas, E. A., Gee, K. R., Kaczmarek, L. K., et al. (2003) Modulation of mitochondrial function by endogenous zn2+ pools. *Proc. Natl. Acad. Sci. U. S. A.* **100**, 6157-6162.

52. Yamasaki, S., Sakata-Sogawa, K., Hasegawa, A., Suzuki, T., Kabu, K., Sato, E., et al. (2007) Zinc is a novel intracellular second messenger. *J. Cell Biol.* **177**, 637-645.

53. Aballay, A., Sarrouf, M. N., Colombo, M. I., Stahl, P. D., & Mayorga, L. S. (1995) Zn2+ depletion blocks endosome fusion. *Biochem. J.* **312**, 919-923.

54. Korichneva, I., Hoyos, B., Chua, R., Levi, E., & Hammerling, U. (2002) Zinc release from protein kinase c as the common event during activation by lipid second messenger or reactive oxygen. *J. Biol. Chem.* **277**, 44327-44331.

55. Wiseman, D. A., Wells, S. M., Hubbard, M., Welker, J. E., & Black, S. M. (2007) Alterations in zinc homeostasis underlie endothelial cell death induced by oxidative stress

from acute exposure to hydrogen peroxide. *Am. J. Physiol.-Lung Cell. Mol. Physiol.* **292**, L165-L177.

56. Kroncke, K. D. (2007) Cellular stress and intracellular zinc dyshomeostasis. *Arch. Biochem. Biophys.* **463**, 183-187.

57. Quesada, A. R., Byrnes, R. W., Krezoski, S. O., & Petering, D. H. (1996) Direct reaction of h2o2 with sulfhydryl groups in hl-60 cells: Zinc-metallothionein and other sites. *Arch. Biochem. Biophys.* **334**, 241-250.

58. Ringkob, T. P., Swartz, D. R., & Greaser, M. L. (2004) Light microscopy and image analysis of thin filament lengths utilizing dual probes on beef, chicken, and rabbit myofibrils. *J. Anim. Sci.* **82**, 1445-1453.

59. Mcrae, R., Lai, B., Vogt, S., & Fahrni, C. J. (2006) Correlative microxrf and optical immunofluorescence microscopy of adherent cells labeled with ultrasmall gold particles. *J. Struct. Biol.* **155**, 22-29.

60. Sherer, N. M., Lehmann, M. J., Jimenez-Soto, L. F., Ingmundson, A., Horner, S. M., Cicchetti, G., et al. (2003) Visualization of retroviral replication in living cells reveals budding into multivesicular bodies. *Traffic* **4**, 785-801.

61. Vonderheit, A., & Helenius, A. (2005) Rab7 associates with early endosomes to mediate sorting and transport of semliki forest virus to late endosomes. *PLoS. Biol.* **3**, 1225-1238.

CHAPTER 4
CORRELATIVE OPTICAL FLUORESCENCE AND SXRF MICROSCOPY

4.1 Correlative Microscopy

The uptake, intracellular distribution, and storage of transition metal cations are tightly regulated processes in all forms of life. Over the past decade an increasing number of diseases have been identified that are associated with impaired metal transport and regulation, including Parkinson's disease [1], Alzheimer's disease [2], Menkes' disease [3-5], and Wilson's disease [3-5]. To elucidate changes in the sub-cellular distribution of trace metals, rigorous and highly sensitive analytical techniques are required. Electron probe X-ray microanalysis (EPXMA) has been used for more than 30 years to obtain information regarding the distribution of elements in cells and tissues. This technique permits the simultaneous detection of any element heavier than C (or Na depending on the detector used) with a resolution limit of about 40 nm and sensitivity of 10–18 g [6]. However, electrons are strongly scattered within thick specimens, resulting in interaction volumes of up to 10 μm and thus a much lower resolution [7]. Consequently, 2D elemental imaging of whole cells with satisfactory subcellular resolution is an unsurmountable task. More recently, synchrotron radiation based X-ray fluorescence microscopy (SXRF) has arisen as a promising gateway into the realm of whole cell elemental imaging [8-11]. By using Fresnel zone plates to focus the incident high-energy X-ray beam, submicrometer spatial resolution may be readily achieved even

on biological specimens with 10-30 μm thickness [8-11]. Similar to the electron microprobe, raster scanning of the specimen allows one to acquire quantitative topographical maps for most biologically relevant elements [8-11]. The detection limit for trace metals has been estimated to range between 5.0×10^{-20} and 3.9×10^{-19} mol μm^{-2} [12], corresponding to a few thousand atoms within the irradiated section of the sample.

Given the high sensitivity combined with 0.2 μm spatial resolution, SXRF is not only well suited for studying the elemental topography of whole cells, but may also be used to discern the trace metal composition of individual organelles such as the mitochondria, Golgi apparatus, endoplasmatic reticulum, or nucleus. A method that would allow for the unequivocal identification of the intracellular organelles or vesicles acting as copper or zinc storage sites in cells defective in copper homeostasis would provide a wealth of information about the major players involved and hence contribute to the understanding of the diseases associated with their dyshomoestasis.

To identify the location of these structures within the cellular context, a suitable biological marker, such as an organelle-specific antibody, requires a xenobiotic elemental label for SXRF microscopy. Furthermore, to achieve the best possible image quality and definition of sub-cellular structures, the cells should be directly grown on a substrate; presently, however, SXRF imaging of single cells has been mostly carried out by depositing cells from suspension. Compared to adherent cells, samples prepared by this method are not only thicker but are also significantly smaller (less spread out), hence resulting in unsatisfactory resolution of sub-cellular structures. In this study the suitability of commercially available, XRF-compatible substrates for growing NIH 3T3 adherent mouse fibroblast cells was explored [13]. Furthermore, the application of

ultrasmall gold-clusters as xenobiotic labels for the colocalization of organelles and elemental maps is reported [13]. More specifically, commercially available secondary antibodies conjugated to FluoroNanogold^{TM}, a dual-label that combines a 1.4 nm gold-cluster with a fluorescent tag (Alexa 488), were utilized for evaluating the sensitivity of SXRF for gold by means of correlative optical fluorescence and SXRF microscopy [13].

4.2 SXRF Imaging of Adherent Cells

Although the widespread application of SXRF for investigating the elemental topography of suspension cells has recently exploded, its use for identifying the elemental distribution in adherent cells has thus far only been sparsely reported. Hence, the sample preparation for adherent cells imparts novel challenges. Previously, mammalian cells have been grown directly on gold or titanium electron microscopy grids coated with a formvar-carbon thin film, a material that is appropriate for the quantitative imaging of trace elements by means of electron probe X-ray microanalysis [14, 15]. Formvar-carbon films are only 50-100 nm thick, are optically transparent, and maintain only low levels of trace metal impurities. Moreover, the physiology and morphology of cells cultured on these substrates remain relatively unaltered thereby illustrating the potential use of gold grids as a support material for cell culture experiments [14-16].

In order to assess their suitability for microXRF experiments, formvar-coated gold grids were used to culture NIH 3T3 fibroblasts (adherent cells), which were then fixed with 3.7% paraformaldehyde (PFA) in isotonic phosphate-buffered saline, and washed with ammonium acetate (0.1 M) to avoid the formation of residual salt crystals that might increase background X-ray fluorescence [13]. For SXRF imaging, the cells

should be dried either via freezing in liquid ethane followed by freeze-drying, or via drying at room temperature under ambient atmosphere. In this study, samples were simply air-dried in order to minimize the amount of contamination potentially introduced into the samples by using extra chemicals required for methods such as freeze-drying [13]. As illustrated by the differential interference contrast (DIC) micrograph shown in Figure 4.1a, simple in-air drying preserved the overall morphology of the cell quite well [13]. Raster scanning of this cell with an incident X-ray energy of 10 keV provided topographical maps with sub-cellular resolution for most biologically relevant elements (Figure 4.1b) [13]. Additionally, the described washing procedure appeared to suffice for avoiding contamination by salt crystals often introduced by buffer washes alone.

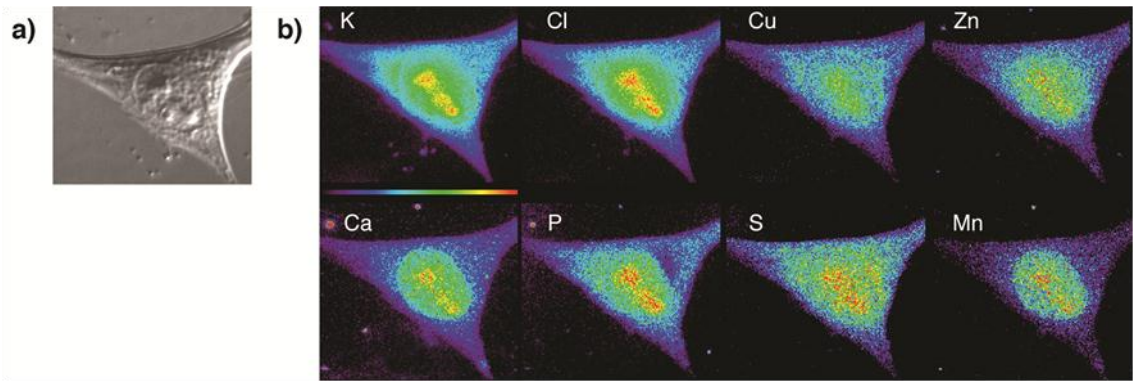

Figure 4.1: Mouse fibroblast cells grown on 200 mesh EM gold grids coated with a formvar-carbon thin film. a) DIC image of in-air dried cell; b) Raster scanned micro-XRF topographical maps for selected elements (excitation at 10 keV, pixel size 0.3 mm, integration time 1 s/pixel).

4.3 Correlative Imaging

Antibodies conjugated to colloidal gold particles have been used extensively as labels in electron microscopy [17] and in principle should be well suited as xenobiotic markers for SXRF imaging by taking advantage of the characteristic Au X-ray fluorescence. However, colloidal gold particles that are greater than 5 nm are too large to penetrate the plasma membrane of cells that are only pretreated with a detergent as used in standard immunofluorescence protocols. Thus, in most cases, the particles are only apt for post-embedding immunolabeling of resin sections, ultrathin cryosections, or freeze-fracture preparations, all of which are procedures that remove the interfering plasma membrane. Because transmission electron microscopy inherently requires very thin specimen sections, colloidal gold particles are well suited as immunolabels for this application. Nevertheless, because smaller gold particles lead to improved labeling efficiencies even in thin sections, new labeling reagents based on ultrasmall gold clusters of approximately 1.4 nm size have been developed [18, 19]. Unfortunately, such small gold clusters are difficult to detect, and for practical applications the particles are better converted to a larger size, typically by means of silver or gold enhancement [20, 21]. Double-labeled secondary anti-bodies that are simultaneously conjugated to an ultrasmall gold cluster and a fluorophore [22] recently became commercially available (FluoroNanogold^{TM}; Nanoprobes, USA), rendering them a potentially attractive solution for correlative optical immunofluorescence and SXRF imaging studies.

Specimen Preparation

Despite being a viable support material for SXRF studies, formvar-carbon coated gold grids are not an ideal choice for immunolabeling experiments with fluoronanogold (FNG). Not only would the gold support grid interfere by means of a strongly increased background fluorescence from scattering of the incident X-ray beam on the specimen, the gold (or silver) enhancement procedure would primarily result in metal deposition onto the grid rather than on the label to increase its size.

To avoid the problems associated with gold-based grids, we explored the suitability of silicon nitride (Si_3N_4) windows, which have been previously used in soft X-ray microscopy as specimen support [23, 24]. Viability tests of cells grown on this ceramics material showed neither cytotoxic effects nor morphological changes according to propidium iodine staining and scanning electron microscopy studies, respectively [25]. To improve cell adherence, commercially available silicon nitride windows were pre-treated with 0.01% poly-lysine solution [13]. Cells were typically grown to 50% confluency and treated according to a standard immunohistochemical protocol [26].

Labeling of the Mitochondria

In a first experiment we labeled mitochondria with a commercially available monoclonal anti-body (mouse IgG_1) that is specific for the ATPase inhibitor protein (IP) associated with complex V of the mitochondrial oxidative phosphorylation system [27], followed by the FluoronanoGold double-labeled secondary Fab' antibody. The sub-cellular distribution of the labeled mitochondria was first visualized in phosphate buffered saline (PBS) by means of fluorescence microscopy with excitation at 488 nm

and using a standard FITC filter set (Figure 4.2a) [13]. As described above for the specimen preparation on EM gold grids, cells were thoroughly washed with ammonium acetate to avoid precipitation of salt residues that might increase the background fluorescence in the SXRF analysis [13]. After in-air drying for 24 hours, the previously imaged cells were located again on the silicon nitride window and then raster scanned with an incident X-ray energy of 11.95 keV [13]. Pixel-by-pixel spectral analysis of the Au Lα emission provided a topographical map of the intracellular distribution of the gold label (Figure 4.2b, left) [13]. Although the contrast and overall resolution of the optical fluorescence micrograph is significantly better, the sensitivity of SXRF is sufficient to detect the ultrasmall 1.4 nm gold-cluster labels without gold-enhancement [21] and also to provide a two-dimensional SXRF-map for the sub-cellular distribution of the mitochondria.

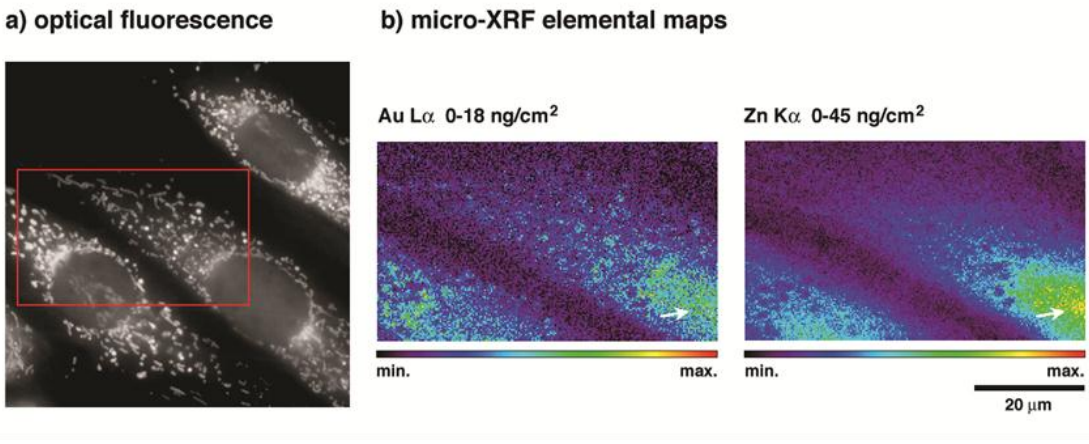

Figure 4.2: Correlative optical and micro-XRF micrographs of FluoroNanogold-labeled mitochondria (adherent mouse fibroblast cells on Si_3N_4 grids). a) Optical fluorescence micrograph (standard FITC filter set). b) micro-XRF elemental maps for Au (La emission) and zinc (Ka emission) of the area marked with red in the optical fluorescence micrograph. The white arrows indicate the nuclear region with high Zn content. The numerical range indicated next to each element refers to the minium and maximum values of the LUT shown at the bottom of each scan.

From the micro-XRF Au map shown in Figure 4.2b (left) it is evident that the emission intensity in the nuclear region, particularly for the cell to the right (white arrow), is surprisingly strong compared with the fluorescence observed in mitochondrial locations [13]. A thorough look at the X-ray emission spectrum reveals that this artifact might be due to the proximity of the Zn Kβ and Au Lα emission bands (Figure 4.3a) [13]. A quantitative map of the Zn distribution based on the Zn Kα emission at 8.64 keV indeed revealed a high Zn content in the nuclear area (Figure 4.2b, right) [13]. Furthermore, a direct comparison of the average emission spectra for two different region-of-interests (ROI) shows that the Zn/Au ratio within the nucleus (ROI 1) is significantly greater compared with the perinuclear region (ROI 2) or the cytoplasm [13]. Consequently, a quantitatively reliable Au map in regions of high Zn can only be obtained by deconvolution of the overlapping Zn Kβ and Au Lα emission bands. Assuming that the ratio of the integrated Zn Kα and Zn Kβ emission remains constant, the actual Au Lα signal intensities can be obtained from the raw single-pixel spectra by means of non-linear least-squares fitting with a set of gaussian functions [13]. As illustrated for ROI 1, spectral deconvolution of the emission band centered around 9.6 keV yielded the individual contributions of the Zn Kβ and Au Lα emissions [13]. A two-dimensional map based on the deconvoluted Au intensities now shows a substantially reduced Au content in the nuclear region compared with the raw data (Figure 4.3b, right) [13]. The remaining Au fluorescence within the nuclear region of the cells is presumably the result of substantial non-specific binding of the FluoroNanogold secondary antibody (vide infra).

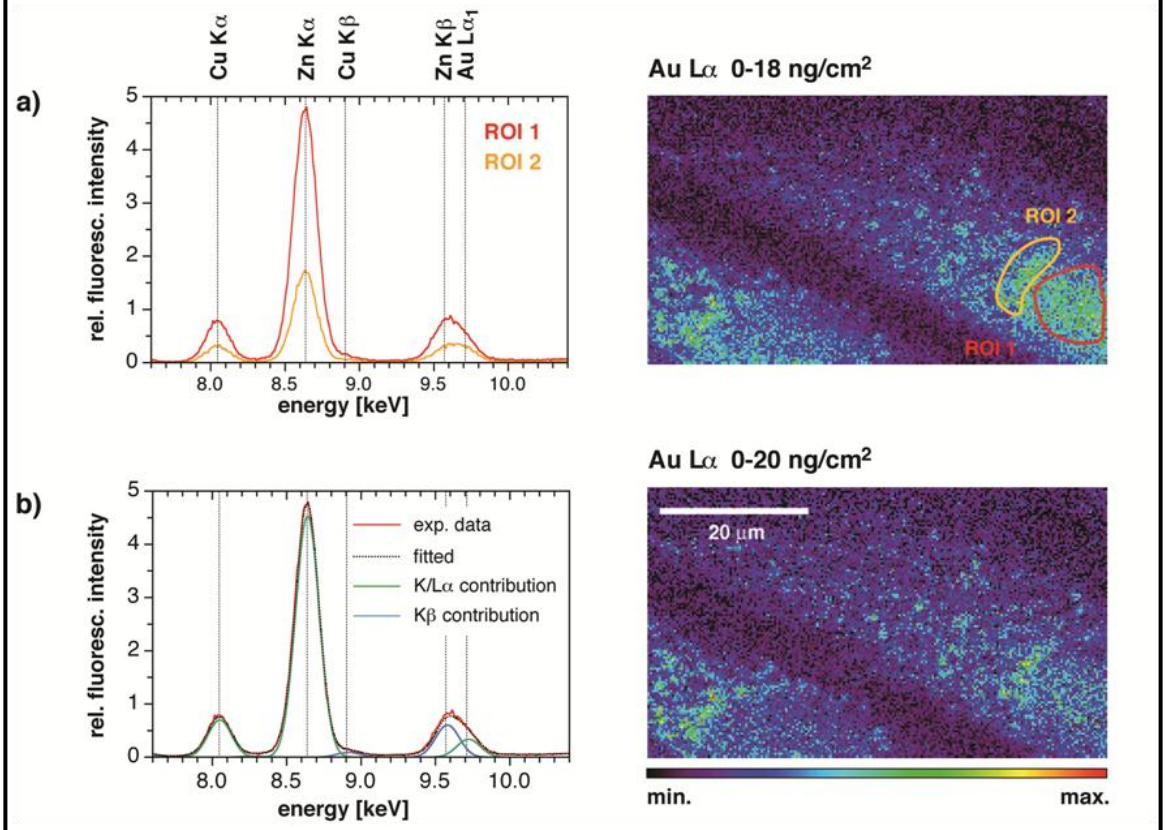

Figure 4.3: a) Average X-ray fluorescence emission spectra (left) for two region of interests (ROIs). Only the energy range between 7.5-10.5 keV is shown. The location of the two ROIs are indicated in the Au La map (raw data) shown to the right. b) Deconvolution by means of least-squares fitting with a set of gaussian functions of the emission band centered around 9.6 keV providing the individual contributions of the Au La (green) and Zn Kb (blue) emissions, respectively. The false-color map to the right shows the Au La emission intensity upon pixel-by-pixel deconvolution of the raw map.

Labeling of the Golgi Apparatus

We performed a second labeling study with commercially available mouse anti-GS28 (Stressgen) as the primary antibody [13]. This monoclonal antibody, also known as p28 or GS28, is a 28 kDa integral membrane protein located on the surface of the Golgi apparatus [28]. The specimen was prepared following steps analogous to those outlined above for the mitochondrial labeling experiment. As shown in Figure 4.4a (right), the optical fluorescence micrograph acquired in PBS buffer solution revealed the

location and morphological details of the Golgi apparatus in close proximity to the nuclear membrane, while the overall background fluorescence remained relatively low throughout the cytoplasm [13]. However, as already observed in the case of the mitochondrial labeling experiment, the area enclosed by the nuclear membrane exhibits a distinctly higher background fluorescence [13]. Principally, this increased background can be caused through non-specific binding of either the primary or secondary antibody. In order to distinguish between these two possibilities we used GS28 in combination with Alexa Fluor 546 anti-mouse IgG, a commonly used secondary antibody that is labeled only with an inconspicuously small, low molecular weight organic fluorophore. As illustrated by the micrograph in Figure 4.4a (left), the nuclear background fluorescence is significantly weaker compared to Figure 4.4a (right) and even lies below the cytoplasmic background [13]. Conclusively, the increased nuclear background appears to be the result of non-specific binding of the FluoroNanogold secondary antibody with nuclear proteins, lipids, nucleic acids, or other bio-molecules, most likely mediated through the attached gold-cluster label. Non-specific binding of the FluoroNanogold secondary antibody in the nuclear area was also apparent in the micro-XRF Au map of the dried cells (Figure 4.4b) [13]. Nevertheless, the XRF Au map reproduced the sub-cellular location and structural details of the Golgi apparatus rather well, as illustrated by the two high-resolution raster scans in Figure 4.4b [13].

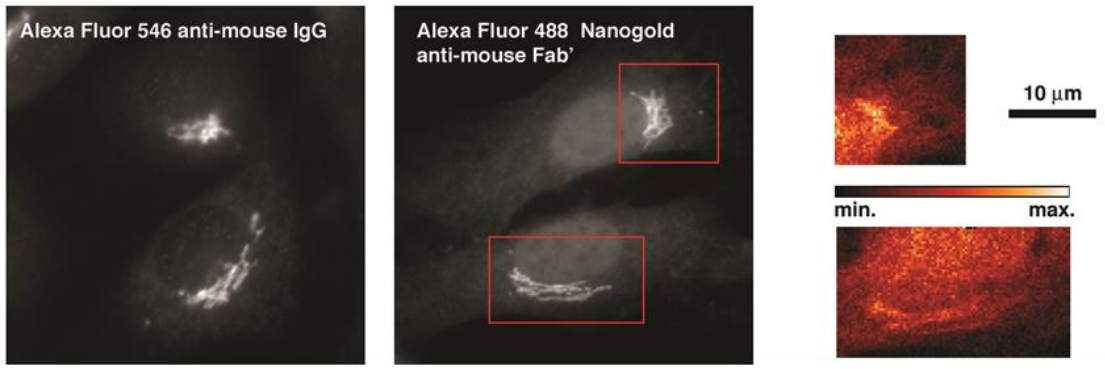

Figure 4.4: Correlative optical and micro-XRF micrographs with Golgi marker anti-GS28 (adherent mouse fibroblast cells on Si_3N_4 grids). a) Optical fluorescence micrograph in PBS as mounting medium. Visualization of GS28 with Alexa Fluor 546 anti-mouse IgG secondary antibody (left, control experiment), and with Alexa Fluor 488 Nanogold double-labeled anti-mouse Fab' secondary antibody (right). b) Two-dimensional micro-XRF elemental maps for Au (La emission) after in-air-drying for the two areas marked with red in the optical fluorescence micrograph

Co-localization of Au-Labeled Structures and Elemental Topography

A wide range of biologically relevant elements can be quantitatively imaged along with the xenobiotic Au elemental label with excitation at 11.95 keV; however, compared with excitation at 10 keV as in Figure 4.1, the sensitivity is reduced by approximately 40% for these elements [13]. Figure 4.5 displays a selection of two-dimensional quantitative elemental maps that were acquired simultaneously with the high-resolution Au map highlighting the Golgi-labeled region shown in Figure 4.4b (bottom) [13]. As indicated by the white arrows, the elemental maps for Zn and Cu (Figure 4.5) show partial colocalization with sub-regions of the Golgi apparatus [13]. Interestingly, the scanned region showed a substantially lower Fe content thus suggesting iron does not accumulate significantly within the Golgi network [13].

When studying the subcellular distribution of diffusable anions or metal cations, it is important to carefully consider how the specimen preparation might affect the intracellular concentration of these elements. While the majority of Zn and Cu is presumably tightly bound to endogenous ligands, either proteins or small molecules, the concentration of Ca or K would be expected to change significantly upon cell membrane permeabilization and extensive washing of the specimen, as required in standard immunohistochemical protocols. This concern is clearly validated by the comparatively low Ca content of the two-dimensional map shown in Figure 4.5 compared with Figure 4.1, for which the specimen preparation included only fixation without further permeabilization or extensive washing [13].

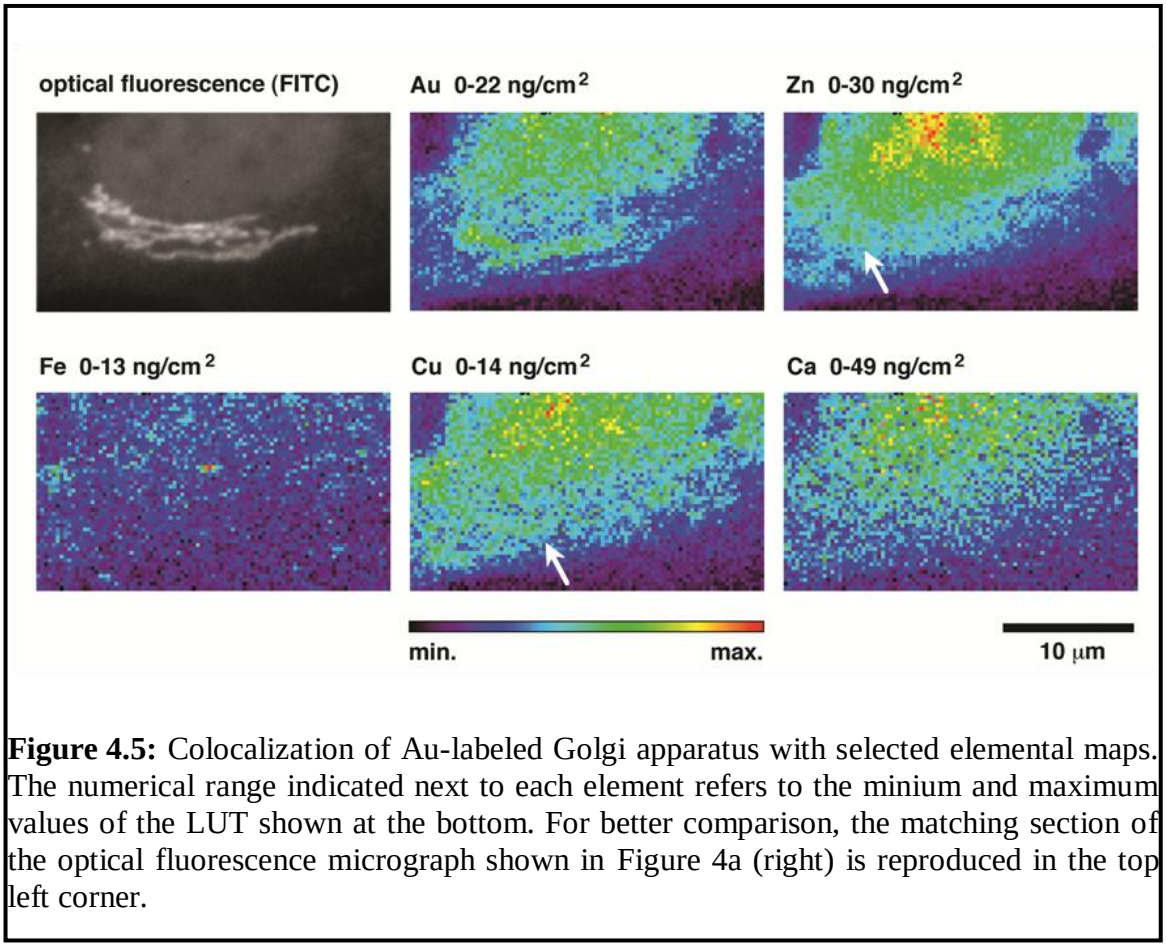

Figure 4.5: Colocalization of Au-labeled Golgi apparatus with selected elemental maps. The numerical range indicated next to each element refers to the minium and maximum values of the LUT shown at the bottom. For better comparison, the matching section of the optical fluorescence micrograph shown in Figure 4a (right) is reproduced in the top left corner.

4.4 Conclusions

The exquisite sensitivity combined with a submicron spatial resolution renders synchrotron X-ray fluorescence microscopy as a powerful technique for acquiring two-dimensional elemental distributions in mammalian cells. By using ultrasmall gold-clusters as xenobiotic elemental labels, we were able to identify, based on the characteristic Au XRF elemental map, the sub-cellular location of individual organelles in adherent mouse fibroblast cells. Although we found a significant degree of non-specific binding in the nuclear area, presumably mediated through the gold-cluster label, the technique should be well suited to specifically label sub-cellular structures within the cytoplasm, and thus to study the elemental composition of organelles in single cells. SXRF imaging complements existing techniques, notably electron microscopy and optical fluorescence microscopy, in a synergistic fashion. By applying dual-labeled markers that contain a fluorescence reporter in combination with the ultrasmall gold-cluster, the three methods can be combined through correlative microscopy. Therefore, this method combination via correlative imaging provides a very powerful methodology to address a wide range of questions concerning elemental speciation in bio-inorganic chemistry, biochemistry, and cellular biology.

Despite the overall successful application of the fluoronanogold labels for correlative imaging in this study, the label produced a substantial amount of background fluorescence in both the optical fluorescence and SXRF images. Future studies with thus involve testing additional available xenobiotic labels in an effort to reduce and ideally eliminate this undesired background fluorescence. After optimization, the above described correlative imaging method will be employed for investigating the copper and

zinc content of cellular organelles and to monitor any alterations present in respective disease-model cell lines or tissue sections.

4.5 Materials and Methods

Cell Culture and Antibodies

NIH 3T3 mouse cells were cultured in Dulbecco's modified Eagle's medium (DMEM) containing 10% bovine serum and supplemented with 200 mM L-glutamine. Mouse anti-GS28 IgG1 (cis-Golgi marker) and mouse anti-OxPhos complex V IgG1 (mitochondrial marker) were purchased from StressGen Biotechnologies (Victoria, Canada) and Molecular Probes (USA), respectively. Additionally, goat anti-mouse Alexa Fluor 488 FluoroNanogold (FNG) was used as a secondary antibody and purchased from Nanoprobes, Inc. (USA).

Immunofluorescence

Mouse 3T3 cells were grown to 50-80% confluency either on formvar-carbon coated 200 mesh gold-grids (EM Sciences, USA) or on silicon nitride windows (Silson Ltd., UK) that were pre-treated for 30 min with 0.01% poly-L-lysine solution (Sigma-Aldrich). Cells were fixed at room temperature for 30 min with pre-warmed (37°C) 3.7% paraformaldehyde (PFA) freshly prepared in phosphate buffered saline (PBS, pH 7.2). The cells were subsequently permeabilized with 0.2% Triton X-100 in PBS (pH 7.2) for 10 min and incubated for 1 h in blocking buffer (Pierce Superblock). Cells were then

incubated with either anti-GS28 (1:300 dilution) or anti-OxPhos complex V (1:300 dilution) for 1 h, washed thoroughly with 0.05% Tween20 in PBS to remove unbound antibodies, and incubated with the Alexa Fluor 488 FluoroNanogold labeled anti-mouse secondary antibody (1:10 dilution) for 1 h. Cells were again washed with Tween20 to remove unbound antibodies. To acquire optical fluorescence micrographs, the silicon nitride windows were mounted onto slides using PBS as mounting medium and imaged with an inverted fluorescence microscope (Zeiss Axiovert) equipped with a standard filter set (FITC).

Synchrotron X-ray Fluorescence Microscopy (micro-XRF)

Cells were treated as described above, and, immediately following fluorescence imaging, rinsed quickly with PBS, then twice with isotonic ammonium acetate (0.1 M) prepared in Milli-Q water, and finally dried in air overnight. Scanning X-ray fluorescence microscopy was performed at the 2-ID-D beamline of the Advanced Photon Source located at Argonne National Laboratory (IL, USA). The grids were placed onto a kinematic specimen holder suitable for both optical and X-ray fluorescence microscopy. The holder was then mounted on a light microscope (Leica DMXRE) and target cells imaged previously by standard fluorescence microscopy were located on the grid relative to a reference point using a high spatial resolution motorized x/y stage (Ludl Bioprecision). Coordinates were determined and used to precisely locate the target cell once the grid was transferred to the microprobe. A Fresnel zone plate was used to focus the monochromatic X-ray beam from an undulator source to a spot size of 0.2x0.2 μm2 on the specimen. An incident photon energy of 11.95 keV was chosen to ensure

excitation of the Lα line of Au, and the sample was raster scanned through the beam at 298K under a helium atmosphere. The pixel step size was set to 0.2 μm and the entire X-ray spectrum was recorded at each pixel using an energy dispersive germanium detector (Canberra LEGe detector).

Spectral Analysis

Elemental maps were created by spectral filtering, using spectral regions of interest matched to characteristic X-ray emission lines to determine the fluorescence signal for each element. Additionally, for improved accuracy, and in particular to reduce crosstalk between overlapping fluorescence lines such as the Zn Kβ (E = 9572 ev) and the Au Lα1,2 (E1 = 9713 eV, E2 = 9628 eV), we fitted the spectra acquired at every single pixel individually, using an adapted version of the SNIP algorithm [29] for background estimation, and modified gaussians for peak fitting [30]. Calibration to elemental area densities (μg/cm2) was done by comparison of X-ray fluorescence signal strength from the sample to fluorescence from thin film standards NBS-1832 and NBS-1833 from the National Bureau of Standards (NBS/NIST, Gaithersburg, MD) using MAPS software [31]. Elemental content was calculated by fitting of the integrated spectra of the acquired fluorescence datasets, and comparing fitted fluorescence signal strength to that resulting from fitting of NBS 1832/33 standard spectra.

4.6 Literature Cited

1. Sayre, L. M., Perry, G., Atwood, C. S., & Smith, M. A. (2000) The role of metals in neurodegenerative diseases. *Cell. Mol. Biol.* **46**, 731-741.

2. Bush, A. I. (2003) Copper, zinc, and the metallobiology of Alzheimer disease. *Alzheimer Dis. Assoc. Dis.* **17**, 147-150.

3. Huffman, D. L., Kwak, J., & O'Halloran, T. V. (2001) Copper delivery from the metallochaperone HAH1 to the Wilsons disease protein. *J. Inorg. Biochem.* **86**, 272-272.

4. Mercer, J. F. B. (2001) The molecular basis of copper-transport diseases. *Trends Mol. Med* **7**, 64-69.

5. Waggoner, D. J., Bartnikas, T. B., & Gitlin, J. D. (1999) The role of copper in neurodegenerative disease. *Neurobiol. Dis.* **6**, 221-230.

6. Roomans, G. M., & Mork, A. C. (1996) X-ray microanalysis applied to the study of salivary glands. *Eur. J. Morphol.* **34**, 203-208.

7. Roomans, G. M. (1988) Introduction to X-Ray-Microanalysis in Biology. *J Electron Micr Tech*
J Electron Micr Tech **9**, 3-17.

8. Dillon, C. T., Kennedy, B. J., Lay, P. A., Lai, B., Cai, Z., Stampfl, A. P. J., et al. (2003) Implementation of X-ray microscopy and micro-XANES analysis for investigations of the cellular uptake and cellular metabolism of transition metals. *J. Phys. IV* **104**, 293-296.

9. Kemner, K. M., Kelly, S. D., Lai, B., Maser, J., O'Loughlin, E. J., Sholto-Douglas, D., et al. (2004) Elemental and redox analysis of single bacterial cells by X-ray microbeam analysis. *Science* **306**, 686-687.

10. Paunesku, T., Rajh, T., Wiederrecht, G., Maser, J., Vogt, S., Stojicevic, N., et al. (2003) Biology of TiO2-oligonucleotide nanocomposites. *Nat. Mater.* **2**, 343-346.

11. Twining, B. S., Baines, S. B., Fisher, N. S., Maser, J., Vogt, S., Jacobsen, C., et al. (2003) Quantifying trace elements in individual aquatic protist cells with a synchrotron X-ray fluorescence microprobe. *Anal. Chem.* **75**, 3806-3816.

12. Twining, B. S., Baines, S. B., Fisher, N. S., Jacobsen, C., & Maser, J. (2003) Quantification and localization of trace metals in natural plankton cells using a synchrotron X-ray fluorescence microprobe. *J. Phys. IV* **104**, 435-438.

13. McRae, R., Lai, B., Vogt, S., Fahrni, C.J. (2006) Correlative microXRF and optical immunofluorescence microscopy of adherent cells labeled with ultrasmall gold particles. **155**, 22-29.

14. Roomans, G. M., Voneuler, A., Mork, A. C., Palsgard, E., & Vonsteyern, C. V. (1993) X-Ray-microanalysis of epithelial-cells in culture. **31**, 21-25.

15. Von Euler, A., Wroblewski, R., & Roomans, G. M. (1992) Correction for extraneous background in X-ray-microanalysis of cell-cultures. **6**, 451-456.

16. Halgunset, J., Tvedt, K. E., & Kopstad, G. (1992) Cellular-Differentiation In Prostatic Explant Cultures - Assessed By Electron-Microscopy And X-Ray-Microanalysis. **21**, 41-51.

17. Bendayan, M. (2001) Worth its weight in gold. *Science* **291**, 1363-+.

18. Robinson, J. M., Takizawa, T., & Vandre, D. D. (2000) Applications of gold cluster compounds in immunocytochemistry and correlative microscopy: comparison with colloidal gold. *J. Microsc.-Oxf.* **199**, 163-179.

19. Robinson, J. M., Takizawa, T., Vandre, D. D., & Burry, R. W. (1998) Ultrasmall immunogold particles: Important probes for immunocytochemistry. *Microsc. Res. Tech.* **42**, 13-23.

20. Hainfeld, J. F. (1995) GOLD, ELECTRON-MICROSCOPY, AND CANCER-THERAPY. *Scanning Microsc.* **9**, 239-256.

21. Weipoltshammer, K., Schofer, C., Almeder, M., & Wachtler, F. (2000) Signal enhancement at the electron microscopic level using Nanogold and gold-based autometallography. *Histochem. Cell Biol.* **114**, 489-495.

22. Takizawa, T., & Robinson, J. M. (2000) FluoroNanogold is a bifunctional immunoprobe for correlative fluorescence and electron microscopy. *J. Histochem. Cytochem.* **48**, 481-485.

23. Kirz, J., Jacobsen, C., & Howells, M. (1995) SOFT-X-RAY MICROSCOPES AND THEIR BIOLOGICAL APPLICATIONS. *Q. Rev. Biophys.* **28**, 33-130.

24. Pine, J., & Gilbert, J. (1992). Live cell specimens for X-ray microscopy. In A. G. Michette, G. R. Morrison & C. J. Buckley (Eds.), *X-ray Microscopy III* (Vol. 67, pp. 384-387). Berlin: Springer.

25. Neumann, A., Reske, T., Held, M., Jahnke, K., Ragoss, C., & Maier, H. R. (2004) Comparative investigation of the biocompatibility of various silicon nitride ceramic qualities in vitro. *J. Mater. Sci.-Mater. Med.* **15**, 1135-1140.

26. Freshney, R. I. (2000). *Culture of Animal Cells: A Manual of Basic Technique* (4th ed.). New York: Wiley-Liss.

27. Haugland, R. P. (2005). *The Handbook. A Guide to Fluorescent Probes and Labeling Technologies* (10th ed.). Eugene: Molecular Probes, Inc. .

28. Subramaniam, V. N., Peter, F., Philp, R., Wong, S. H., & Hong, W. J. (1996) GS28, a 28-kilodalton Golgi SNARE that participates in ER-Golgi transport. *Science* **272**, 1161-1163.

29. Ryan, C. G., Clayton, E., Griffin, W. L., Sie, S. H., & Cousens, D. R. (1988) SNIP, A STATISTICS-SENSITIVE BACKGROUND TREATMENT FOR THE QUANTITATIVE-ANALYSIS OF PIXE SPECTRA IN GEOSCIENCE APPLICATIONS. *Nucl. Instrum. Methods Phys. Res. Sect. B-Beam Interact. Mater. Atoms* **34**, 396-402.

30. Van Espen, P. (2002). Spectrum Evaluation. In R. Van Grieken & A. A. Markowicz (Eds.), *Handbook of X-ray Spectrometry* (Vol. 29, pp. 239-340). New York: Marcel Dekker.

31. Vogt, S., Maser, J., & Jacobsen, C. (2003) Data analysis for X-ray fluorescence imaging. *J. Phys. IV* **104**, 617-622.

CHAPTER 5
COPPER REDISTRIBUTION IN ATOX1-DEFICIENT CELLS

5.1 Implications of Copper Dyshomeostasis in Neurological Diseases

Copper (Cu) is a trace metal essential for the maintenance of human health. Serving as a cofactor for a number of enzymes, Cu plays an important role in a broad range of biological processes including cellular respiration, free radical defense, iron mobilization and uptake, formation of connective tissue, pigmentation, blood clotting, and the synthesis of neurotransmitters [1]. Conversely, cellular Cu accumulation to excessive levels is detrimental as it catalyzes the formation of reactive oxygen species (ROS) that may damage DNA, proteins, and other biomolecules, thus resulting in increased oxidative stress and ultimately cell death [2, 3]. Given this dualistic nature, cells have evolved an intricate machinery for the transport, storage and regulation of intracellular Cu, such that sufficient amounts are available to fulfill its essential roles while avoiding accumulation to potentially damaging levels [4-9]. Instances of Cu imbalance or homeostatic dysfunction have been directly associated with a number of neurological diseases, including Menkes disease [10, 11], Wilson's disease [12-14], Alzheimer's disease [15-19], Parkinson's disease [16-18], and amyotrophic lateral sclerosis [17, 20, 21], further underscoring the necessity for tightly controlled levels of intracellular Cu [22-24].

The discovery of genes coding for proteins involved in Cu-uptake, transport and regulation led to the identification of a host of proteins involved in Cu homeostasis. On a

cellular level, Cu is imported across the plasma membrane via the high affinity Cu transporter Ctr1, and subsequently partitioned into distinct trafficking pathways that involve specialized metallochaperones [25-29]. For example, the Cu chaperone Ccs is responsible to escort and incorporate Cu into cytoplasmic superoxide dismutase (SOD) [30, 31]. Likewise, the three chaperone proteins Cox17, Cox11, and Sco1 deliver Cu to mitochondrial cytochrome c oxidase [32-35], and the copper chaperone Atox1 is critical for transport of Cu to either the Menkes (ATP7a) or Wilson's (ATP7b) disease ATPases situated in the trans-Golgi network (TGN) [36-38], where it is delivered either to cuproenzymes such as ceruloplasmin and lysyl oxidase, or trafficked through the secretory pathway for extracellular release [39].

While significant progress has been made towards the mechanistic understanding of cellular Cu homeostasis at the molecular level, important questions remain regarding the maintenance of Cu at the cellular level. For instance, Cu uptake and release occur with a surprisingly rapid kinetics [40], suggesting that a portion of the total cellular Cu is present in a kinetically labile form and thus readily available for distribution and uptake into cuproenzymes; however, the nature of this labile pool, its sub-cellular localization, and potential alterations in diseases associated with defects in Cu trafficking are poorly understood. In view of the potential toxicity of Cu, a detailed understanding of the redistribution and mis-localization of labile Cu in these diseases is of particular importance.

Transgenic mouse models of copper chaperones have proven to be extremely beneficial for studying the physiological roles of these proteins [41] and thus represent an opportunity for investigating the potential Cu redistribution associated with defects in Cu

trafficking pathways. In this report, we focused on studying the sub-cellular Cu distribution in Atox1$^{-/-}$ fibroblasts [42], an embryonic mouse cell line that is deficient in the copper chaperone protein, Atox1, responsible for the trafficking of Cu to the TGN network [36]. The Atox1 protein was originally discovered through its yeast homologue Atx1, which showed a protective function against superoxide and peroxide toxicity [43]. The Atox1$^{-/-}$cell line was created by disruption of the Atox1 locus through gene-trap insertion of a β-galactosidase-neomycin marker in mouse embryonic stem cells [37]. Mice deficient for Atox1 display a severe phenotype characterized by growth retardation, perinatal mortality, and congenital malformations, much like the phenotype observed in Menkes' disease [37].

At the cellular level, significant differences in the Cu-mediated trafficking of the Menkes ATPase from the TGN to cytosolic vesicular compartments were observed between Atox1$^{+/+}$ and Atox1$^{-/-}$cells [36]. While Atox1$^{-/-}$ cells still showed a Cu-dependent translocation of the Menkes protein out of the TGN compartments, the movement was significantly impaired in a dose and time-dependent manner. Additionally, more recent results have implied that Atox1also functions as a Cu-dependent transcription factor that mediates Cu-induced cell proliferation [44]. In view of the essential role of Atox1 in the trafficking of cellular Cu and maintaining its overall homeostasis, the elucidation of differences in the sub-cellular Cu distribution between Atox1$^{+/+}$ and Atox1$^{-/-}$cells was of particular interest in this study.

To quantify the distribution of Cu at the sub-cellular level, highly sensitive microanalytical techniques are required. While the sensitivity of traditional methods, such as inductively coupled plasma mass spectrometry (ICP-MS), atomic emission

spectroscopy (AES), or electron probe x-ray fluorescence micro-analysis (EPXMA) is insufficient for analyzing the elemental contents of a single cell, several more recently developed techniques, notably secondary ion mass spectrometry (SIMS), nuclear microprobes (PIXE or PIGE), and synchrotron x-ray fluorescence microscopy (SXRF, SRIXE, or microXRF) do offer sufficient sensitivity to obtain spatially resolved elemental maps at the sub-cellular level [45-49]. These new imaging techniques have already provided important insights into the localization of Cu pools within individual cells. For example, an SXRF study of Cu-loaded NIH 3T3 cells yielded detailed topographical elemental maps and suggested the presence of a labile Cu pool in the TGN region and mitochondria [50]. In another report, high-resolution SXRF imaging of human microvascular endothelial cells revealed an intriguing re-localization of Cu from intracellular compartments towards the tips of filopodia, thus highlighting the importance of endogenous Cu during angiogenesis [51]. A similar Cu accumulation was recently described in thin neurites formed upon nerve growth factor (NGF) stimulated differentiation of rat pheochromocytoma (PC12) cells, which were used as an in vitro model of dopaminergic cells [52]. Given these early successes in imaging the sub-cellular distribution of Cu with great detail, SXRF imaging seemed ideally situated for studying the effects of Cu re-localization in cells with altered trafficking pathways, such as the cells deficient for Atox1 ($Atox1^{-/-}$ cells) [42].

5.2 SXRF Imaging of Atox1 Mouse Fibroblasts

Choosing the Appropriate Growth Conditions

To choose growth conditions that would maximize the differences in Cu distribution and thus best reveal the impact of altered Cu trafficking pathways, we utilized an earlier study on the Cu-dependent relocalization of the Menkes ATPase (ATP7a) as a guideline [36]. Specifically, the following findings were taken into consideration: (1) the Menkes protein localization and total cellular Cu were identical for both $Atox1^{-/-}$ and $Atox1^{+/+}$ (wildtype) cells under Cu-limiting conditions, where cells were grown in low-serum media supplemented with 200 μM batho-cuproin-sulfonic acid (BCS) as an extracellular Cu(I)-chelator; (2) differences in the Cu-mediated trafficking of ATP7a out of the TGN were most pronounced when the media was supplemented with 10 μM $CuCl_2$ following BCS treatment; and (3) the impaired Menkes protein trafficking in $Atox1^{-/-}$ cells could be rescued by supplementation with ≥ 100 μM $CuCl_2$ or upon extended incubation periods (> 4 h) [36]. Based on these data we anticipated that differences in the Cu distribution between $Atox1^{-/-}$ and wild-type cells would be most pronounced when cells were pretreated with 200 μM BCS for 48 hours followed by supplementation with 10 μM and less than 100 μM $CuCl_2$ in full media over a period of 4 hours. Although no data were provided for the intermediate concentration range, supplementation with 50 μM $CuCl_2$ appeared to strike the best balance between improving the signal-to-noise ratio for SXRF detection while still maintaining a marked difference in Menkes trafficking between $Atox1^{-/-}$ and $Atox1^{+/+}$ cells [42]. As a control, both cell lines were also cultured under basal conditions in full media without any additional supplementation [42].

Sample Preparation and Quantitative Analysis of SXRF Elemental Maps

Adherent cells were grown directly on an x-ray compatible substrate (silicon nitride), chemically fixed with paraformaldehyde, and air-dried overnight [42]. Individual cells were raster with a 0.5 μm step size scanned using an excitation of 10.0 keV, yielding 2D maps for all biologically relevant first row transition elements [42]. The considerable size of adherent fibroblast cells combined with the necessity to obtain elemental maps with high spatial resolution resulted in long data acquisition times (2-4 hours per cell), and therefore restricted the sample size to only three repetitions for each growth condition and cell type. Quantitative elemental maps for Cu, Zn, and Fe were analyzed in terms of the total cellular content as well as the nuclear and cytoplasmic portions (Table 5.1) [42]. To account for differences in cell size that might also contribute to differences in trace metal content, the data are listed as averaged densities in units of $pmol/cm^2$ [42]. For ease of comparison, the density data compiled in Table 5.1 are also illustrated in a set of three bar graphs (Figure 5.1) [42].

Table 5.1: Trace metal contents of Atox1$^{+/+}$ and Atox1$^{-/-}$ cells cultured in basal medium and medium supplemented with 50 mM $CuCl_2$ for 4 h.

	basal medium [a]		50 mM $CuCl_2$/4 h [b]	
metal/ROI [c]	Atox1$^{+/+}$	Atox1$^{-/-}$	Atox1$^{+/+}$	Atox1$^{-/-}$
Cu [pmol/cm^2] [d]				
whole cell	14 ± 1	24 ± 3	25 ± 3	26 ± 2
cytoplasm	14 ± 1	22 ± 3	23 ± 4	24 ± 1
nucleus	16 ± 1	31 ± 4	31 ± 4	39 ± 1
ratio [%] [e]	23 ± 6	29 ± 3	20 ± 3	22 ± 4
Fe [pmol/cm^2] [d]				
whole cell	27 ± 1	29 ± 1	22 ± 5	27 ± 1
cytoplasm	26 ± 1	30 ± 1	22 ± 5	27 ± 1
nucleus	27 ± 1	28 ± 1	23 ± 4	29 ± 1
ratio [%][e]	20 ± 4	21 ± 6	16 ± 4	15 ± 3
Zn [pmol/cm^2] [d]				
whole cell	78 ± 10	82 ± 4	55 ± 10	67 ± 6
cytoplasm	67 ± 8	70 ± 2	46 ± 9	55 ± 5
nucleus	122 ± 4	124 ± 21	108 ± 14	134 ± 17
ratio [%][e]	33 ± 7	33 ± 7	32 ± 6	30 ± 8

[a] DMEM, 10% bovine serum, 200 mM glutamine; [b] cells cultured basal medium and switched to medium supplemented with 50 mM $CuCl_2$ for 4 h. [c] ROI = region of interest indicated in each row. [d] average metal content based on three individual cells. [e] percent ratio of the integrated nuclear metal and total cellular metal content.

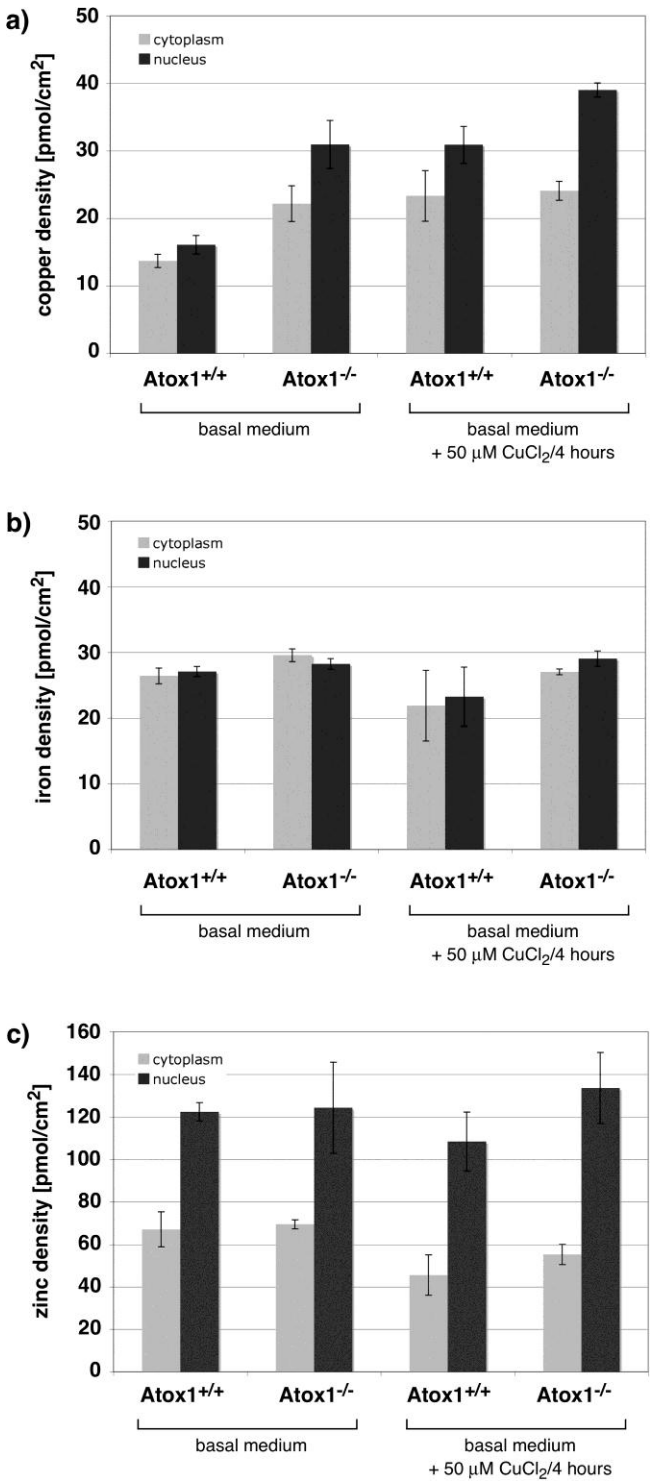

Figure 5.1: Trace metal contents of Atox1$^{+/+}$ and Atox1$^{-/-}$ cells cultured in basal media and media supplemented with 50 µM $CuCl_2$ for 4 h. The SXRF data were quantitatively analyzed for the content of Cu (a), Fe (b) and Zn (c). The corresponding numerical values are compiled in **Table 5.1**.

Metal Distribution under Basal Growth Conditions

Integration of the Cu signal in the nucleus compared to cytoplasm revealed significant differences between Atox1$^{-/-}$ and Atox1$^{+/+}$ wild-type control cells (Table 5.1) [42]. Consistent with previous findings based on atomic absorption spectroscopy of bulk samples [36], Atox1$^{-/-}$ cells significantly accumulated Cu due to impaired Cu efflux under these conditions [42]. Furthermore, a more recent study with a metallothionein (MT)-knockout cell line also showed increased intracellular Cu levels upon siRNA-mediated knockdown of Atox1 [53]. In the wild-type cells, approximately 23% of the total cellular Cu localized to the nuclear region (Table 5.1) [42]. Interestingly, Atox1$^{-/-}$ cells consistently showed an elevated nuclear Cu content compared with Atox1$^{+/+}$ cells. In contrast, the Zn and Fe content showed no significant variations between the two cell lines for neither the whole cell analysis nor the nuclear/cytoplasmic distribution ratios (Table 5.1 and Figure 5.1) [42].

Cells growing under normal growth conditions should exhibit only minor alterations in copper homeostasis and consequently the copper distribution if they are defective for a copper transporting protein. Consistent with this view, both cell lines showed a rather diffuse, nucleocytoplasmic Cu distribution under basal growth conditions (Figure 5.2), thus implying cells, with or without Atox1, grown under normal conditions experience no apparent difficulty in maintaining the appropriate intracellular copper distribution [42]. However, due to the low cellular Cu content of cells grown under basal growth conditions, the signal-to-noise ratios of the resulting SXRF maps were insufficient for drawing unequivocal conclusions concerning differences in the sub-cellular Cu distribution between the two cell lines. A comparison with the Zn elemental

maps obtained from the same set of cells showed no obvious differences in the zinc distribution between Atox1$^{-/-}$ and wild-type Atox1$^{+/+}$ cells (Figure 5.3) [42].

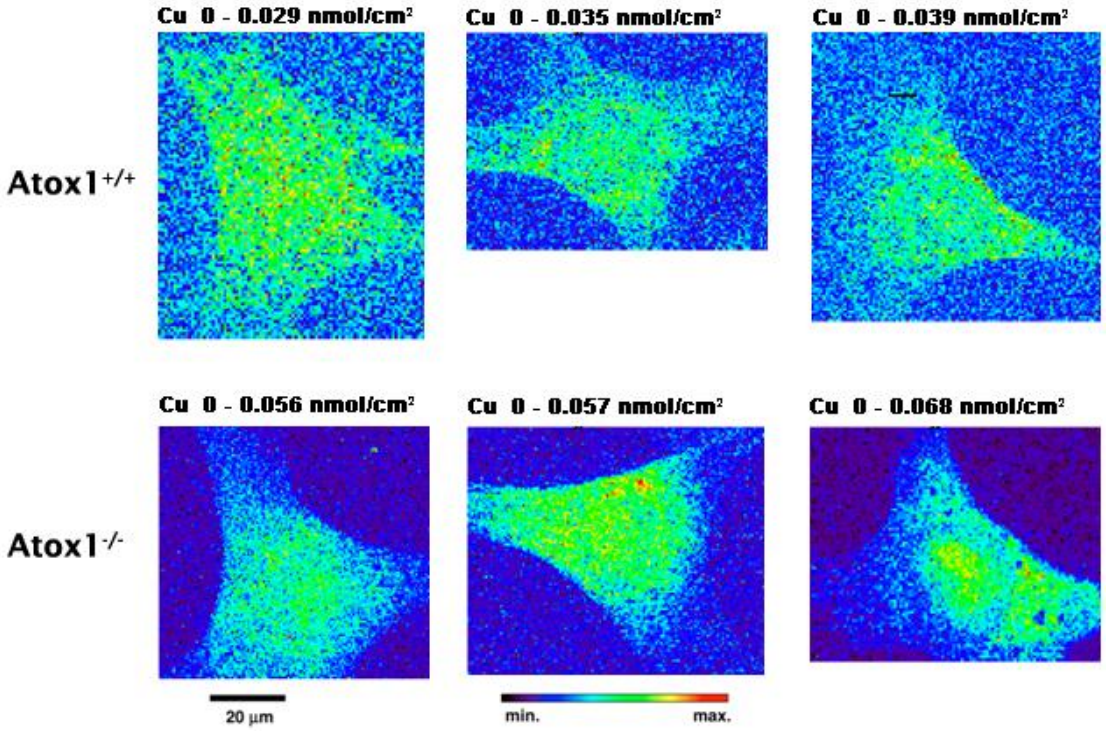

Figure 5.2: False-color micrographs showing the subcellular distribution of Cu in Atox1-deficient (Atox1$^{-/-}$) and wild-type (Atox1$^{+/+}$) cells visualized by SXRF microscopy. Cells were grown in basal media. The density interval indicated above each scan refers to the full dynamic range of the false-color scale depicted in the bottom row.

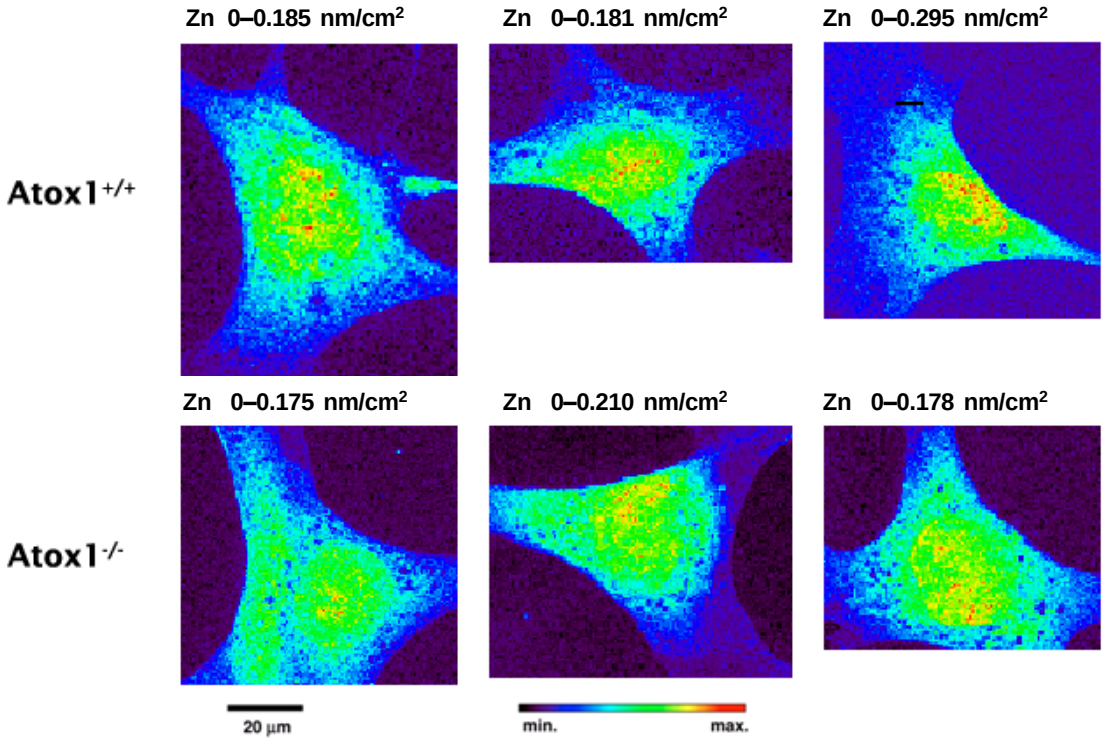

Figure 5.3: False-color micrographs showing the subcellular distribution of Zn in Atox1-deficient ($Atox1^{-/-}$) and wild-type ($Atox1^{+/+}$) cells visualized by SXRF microscopy. Cells were grown in basal media. The density interval indicated above each scan refers to the full dynamic range of the false-color scale depicted in the bottom row.

Effect of Copper Supplementation

Wild-type cells incubated with 50 µM $CuCl_2$ for 4 hours displayed a marked increase of the cellular Cu content (Table 5.1) [42]. Interestingly, $Atox1^{-/-}$ cells treated under the same conditions revealed a similar increase of intracellular Cu (Table 5.1) [36], thus contrasting the observations under basal growth conditions. Nevertheless, these findings are in agreement with the data on bulk samples reported in the literature [36]. While the impaired Cu efflux mechanism in $Atox1^{-/-}$ cells eventually leads to a substantial increase in the intracellular Cu content [37], at early time points the response

to elevated extracellular Cu(II) is indistinguishable compared to the wild-type cells. Likewise, the ratio of nuclear to total Cu was identical within experimental error for both cell lines and similar to wild-type cells grown under basal conditions (Figure 5.1) [42]. A comparison of the Fe content showed no apparent differences between the two cell lines in response to Cu(II) supplementation, although the ratio of nuclear Fe appeared to be reduced in both cases (Table 5.1 and Figure 5.1) [42]. Similarly, analysis of the Zn content and relative distribution between nucleus and cytoplasm showed no significant differences and appears to be independent of the cell type and growth conditions with Cu(II) supplementation (Table 5.1 and Figure 5.1) [42].

Despite the similarities of the total Cu content, the sub-cellular distribution, as revealed by the quantitative SXRF maps shown in Figure 5.4, showed striking differences between Atox1$^{-/-}$ and Atox1$^{+/+}$ cells [42]. The wild-type cell line consistently displayed a strong Cu localization in the perinuclear region with a slightly less pronounced abundance throughout the cytoplasm and within the cell nucleus (Figure 5.4, top row) [42]. Conversely, as observed under basal growth conditions (Figure 5.3, bottom row), the Cu distribution in Atox1$^{-/-}$ cells revealed no obvious compartmentalization or sub-cellular accumulation, but instead a relatively diffuse distribution throughout the entire cell body (Figure 5.4, bottom row) [42]. While both cell lines showed a similar ratio of nuclear to total cellular Cu, the distribution in Atox1$^{-/-}$ cells appeared entirely unstructured and lacked areas of localization as observed in the nucleus of wild-type cells (Figure 5.4). A comparison with the Zn elemental maps obtained from the same set of cells showed no marked differences between Atox1$^{-/-}$ and wild-type cells (Figure 5.5) [42].

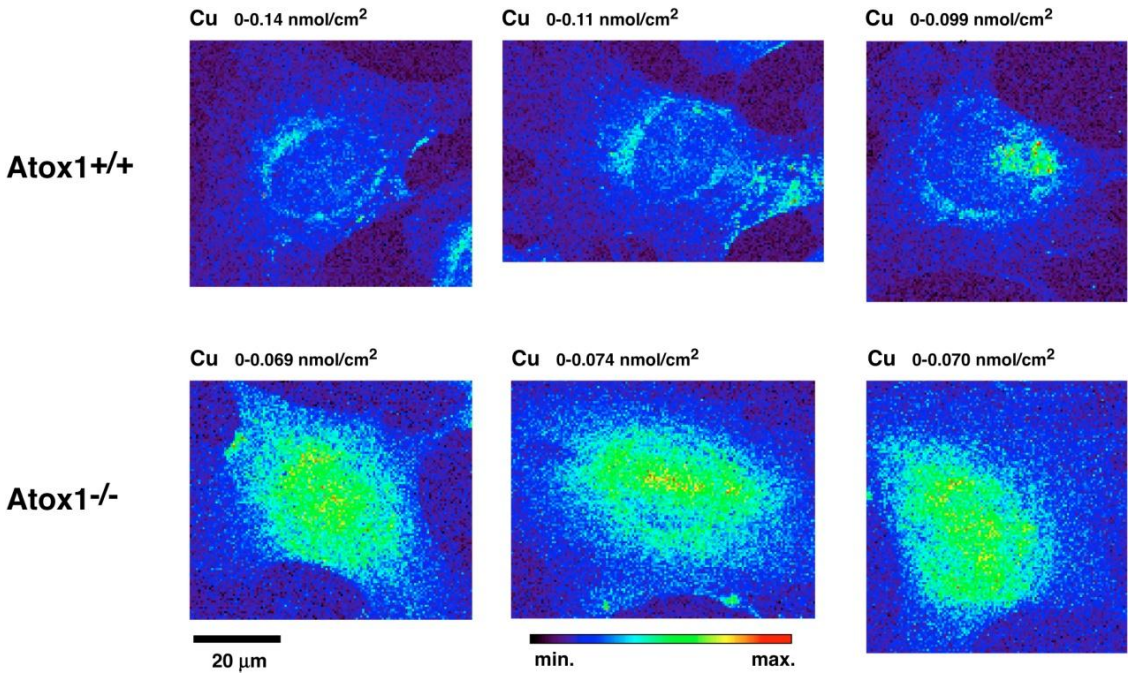

Figure 5.4: False-color micrographs showing the sub-cellular distribution of Cu in Atox1-deficeint ($Atox1^{-/-}$) and wild-type ($Atox1^{+/+}$) cells visualized by SXRF microscopy. Cells were grown in media supplemented with 50 μM $CuCl_2$ for 4 h after pretreatment with 200 μM BCS for 48 hours. The density interval indicated above each scan refers to the full dynamic range of the false-color scale depicted in the bottom row.

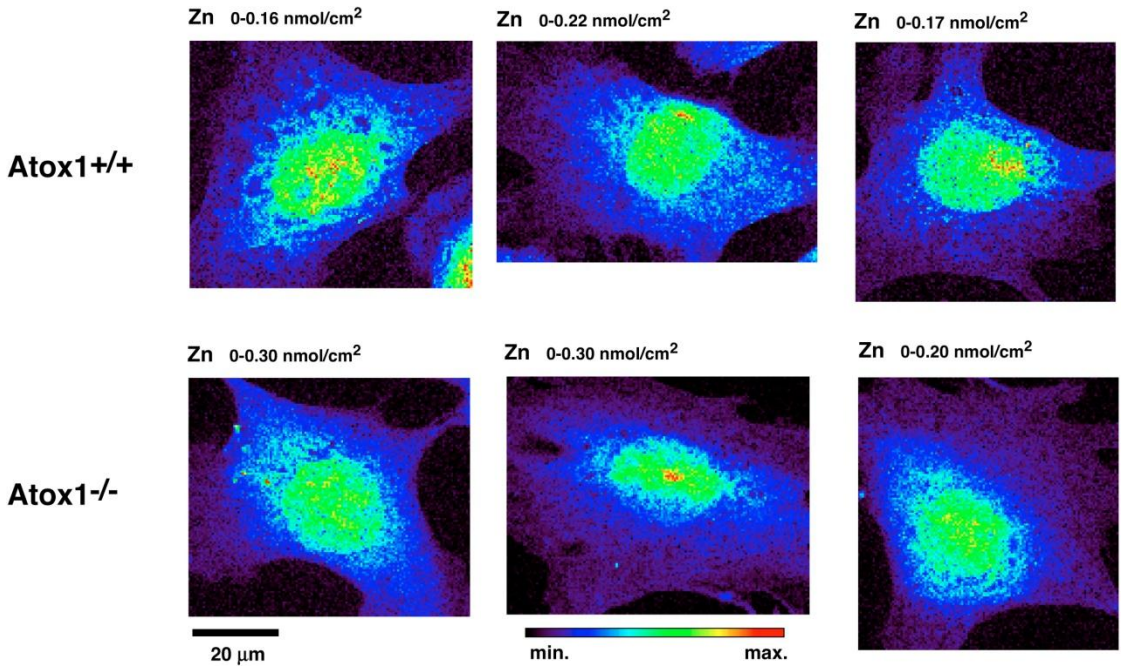

Figure 5.5: False-color micrographs showing the sub-cellular distribution of Zn in Atox1-deficeint ($Atox1^{-/-}$) and wild-type ($Atox1^{+/+}$) cells visualized by SXRF microscopy. Cells were grown in media supplemented with 50 μM $CuCl_2$ for 4 h after pretreatment with 200 μM BCS for 48 hours. The density interval indicated above each scan refers to the full dynamic range of the false-color scale depicted in the bottom row.

Previous studies demonstrated that supplementation with 100 μM $CuCl_2$ over a time period of 4 hours resulted in almost complete relocalization of the Menkes ATPase out of the TGN to cytoplasmic compartments [36]. Given the comparable incubation conditions and time course of our SXRF experiments, we can assume that a similar re-localization of the Menkes protein occurred; however, a significant fraction of Cu remained localized in the perinuclear region (Figure 5.4, top row) [42]. While the Cu-dependent trafficking of the Menkes protein out of the TGN is well established [36, 54], it still remains to be determined what fraction of cellular Cu is actually re-localized in this process. The SXRF data imply that Cu trafficking and distribution is not exclusively

linked with Menkes trafficking at early time points following stimulation with elevated extracellular Cu(II). Taking into account that the requirement for Atox1 in Cu-mediated trafficking of the Menkes protein can be bypassed with excess Cu [36], we cannot exclude the possibility that the diffuse Cu distribution in Atox1$^{-/-}$ cells is a consequence of Cu delivery to Menkes protein containing compartments, through Atox1-independent loading either prior to or after trafficking out of the TGN. Such a scenario would imply, however, that alternative Atox1-dependent trafficking pathways exist that lead to compartmentalization of Cu in the perinuclear region of the wild-type cells. Alternatively, the diffuse Cu distribution pattern in Atox1$^{-/-}$ cells might be the result of a random redistribution process owing to the absence of the regular trafficking pathway.

5.3 Summary

Spatially well-resolved SXRF elemental maps of individual adherent mouse fibroblast cells revealed intriguing differences in the Cu distribution of Atox1$^{-/-}$ cells compared to the corresponding wild-type cells. While the latter cells showed a well-defined perinculear Cu localization, the copper distribution in Atox1$^{-/-}$ cells was reproducibly unstructured and diffuse throughout the entire cell. Although the SXRF elemental maps cannot reveal the nature of the associated cellular structure or organelles in the absence of a xenobiotic label, the characteristic perinuclear Cu distribution pattern might point towards the involvement of the Golgi apparatus, late endosomes, or mitochondria, all of which are typically found in the vicinity of the nuclear envelope. Therefore, the data highlight the importance of Atox1, not only as a metallochaperone for

delivering Cu to essential cuproemzymes, but also as a key player in maintaining the proper distribution and organization of Cu at the cellular level.

5.4 Materials and Methods

Reagents and Materials

The wild-type Atox1$^{+/+}$ and Atox1$^{-/-}$ embryonic mouse fibroblast cell lines were a generous gift from Jonathan D. Gitlin [36]. The cells were cultured in Dulbecco's modified Eagle's medium (DMEM, GIBCO-BRL, Gaithersburg, USA) supplemented with 10% bovine serum (GIBCO), 200 mM L-glutamine (GIBCO), 250 µg/mL geneticin (GIBCO), penicillin (50 IU/mL) and streptomycin (50 mg/L) at 37°C under an atmosphere of humidified air containing 5% CO_2. The culture medium was sterilized by filtration through 0.2 µm filters.

Sample Preparation

Cells were grown to 50-80% confluency on silicon nitride windows (2 x 2 x 0.0005 mm, Silson Ltd., UK) that were pre-treated for 30 min with 0.01% poly-L-lysine solution (Sigma-Aldrich). For preparations in basal media, cells were seeded directly into 6-well culture plates containing the silicon nitride windows and were grown at 37°C/5% CO_2 for reaching their desired confluency. For experiments that involved supplementation of the culture medium with Cu(II), cells were first grown in basal media to 50% confluency as described above, then switched for 48 h to basal media containing 200 µM bathocuproine disulphonate (BCS, Sigma-Aldrich), thoroughly washed with 1X-

PBS (pH 7.2, pre-warmed to 37°C), and finally incubated in full growth media supplemented with 50 µM $CuCl_2$ (Sigma-Aldrich) for 4 h at 37°C.

Following the growth/incubation conditions described above, cells were further prepared for SXRF experiments as previously described [55]. Briefly, cells were washed with PBS (pre-warmed at 37°C), and fixed for 10 min at room temperature with 3.7% paraformaldehyde (Sigma-Aldrich, freshly prepared solution in PBS). After thoroughly washing with PBS, the samples were rinsed twice with sterile dH_2O followed by two brief washes with isotonic ammonium acetate (Sigma-Aldrich, 0.1 M solution in sterile dH_2O). Finally, samples were air-dried overnight in a covered sterile cell culture dish.

Synchrotron Radiation X-ray Fluorescence Microscopy (SXRF)

Synchrotron radiation x-ray fluorescence (SXRF) microscopy was performed at the 2-ID-D beamline of the Advanced Photon Source located at Argonne National Laboratory (IL, USA). The air-dried cells grown on silicon nitride windows were placed onto a kinematic specimen holder suitable for both optical and x-ray fluorescence microscopy. The holder was mounted on a light microscope (Leica DMXRE) and target cells were located on the grid relative to a pre-determined reference point using a motorized x/y stage (Ludl Bioprecision). Coordinates were recorded and used to precisely locate the target cell(s) once the grid was transferred to the microprobe. For XRF excitation, a monochromatic X-ray beam generated by an undulator source was focused to a spot size of 0.5x0.5 $\lceil m^2$ on the specimen by using a Fresnel zone plate. An excitation energy of 10 keV was chosen to ensure excitation of all first row transition elements as well as Ca and K, although to a lesser extent. The sample was subsequently raster scanned through the beam at 298K under a helium atmosphere. The pixel step size

was set to 0.5 μm and the entire X-ray spectrum was recorded for each pixel using an energy dispersive germanium detector (Canberra LEGe detector).

Data Analysis

Elemental maps were created by spectral filtering, using spectral regions of interest matched to characteristic x-ray emission lines to determine the fluorescence signal for each element. Calibration to elemental area densities ($\mu g/cm^2$) was done by comparison of x-ray fluorescence signal strength from the sample to fluorescence from thin film standards NBS-1832 and NBS-1833 from the National Bureau of Standards (NBS/NIST, Gaithersburg, MD) using MAPS software [56]. Elemental content was calculated by fitting of individual spectra of the acquired fluorescence datasets, and comparing fitted fluorescence signal strength to that resulting from fitting of NBS 1832/33 standard spectra.

Acknowledgment

We thank Jonathan Gitlin (Washington University, St. Louis, USA) for providing us with samples of the $Atox1^{-/-}$ and $Atox1^{+/+}$ cell lines. We also thank Stefan Vogt (Argonne National Laboratory) for providing support with the MAPS software. Financial support from the National Institutes of Health (R01GM067169) is gratefully acknowledged. Use of the Advanced Photon Source was supported by the U.S. Department of Energy, Office of Science, Office of Basic Energy Sciences, under Contract No. DE-AC02-06CH11357.

5.5 Literature Cited

1. Mocchegiani, E., Bertoni-Freddari, C., Marcellini, F., & Malavolta, M. (2005) Brain, Aging and Neurodegeneration: Role of Zinc Ion Availability. *Prog. Neurobiol.* **75**, 367-390.

2. Stohs, S. J., & Bagchi, D. (1995) Oxidative Mechanisms in the Toxicity of Metal-Ions. *Free Radic. Biol. Med.* **18**, 321-336.

3. Valko, M., Morris, H., & Cronin, M. T. D. (2005) Metals, Toxicity and Oxidative Stress. *Curr. Med. Chem.* **12**, 1161-1208.

4. Harris, E. D. (2000) Cellular Copper Transport and Metabolism. *Annu. Rev. Nutr.* **20**, 291-310.

5. Puig, S., & Thiele, D. J. (2002) Molecular Mechanisms of Copper Uptake and Distribution. **6**, 171-180.

6. Kim, B. E., Nevitt, T., & Thiele, D. J. (2008) Mechanisms for Copper Acquisition, Distribution and Regulation. *Nat. Chem. Biol.* **4**, 176-185.

7. Bertinato, J., & L'abbe, M. R. (2004) Maintaining Copper Homeostasis: Regulation of Copper-Trafficking Proteins in Response to Copper Deficiency or Overload. *J. Nutr. Biochem.* **15**, 316-322.

8. Lalioti, V., Muruais, G., Tsuchiya, Y., Pulido, D., & Sandoval, I. V. (2009) Molecular Mechanisms of Copper Homeostasis. *Front. Biosci.* **14**, 4878-4903.

9. Turski, M. L., & Thiele, D. J. (2009) New Roles for Copper Metabolism in Cell Proliferation, Signaling, and Disease. *J. Biol. Chem.* **284**, 717-721.

10. Andrews, N. C. (2002) Metal Transporters and Disease. *Curr. Opin. Chem. Biol.* **6**, 181-186.

11. De Bie, P., Muller, P., Wijmenga, C., & Klomp, L. W. J. (2007) Molecular Pathogenesis of Wilson and Menkes Disease: Correlation of Mutations with Molecular Defects and Disease Phenotypes. *J. Med. Genet.* **44**, 673-688.

12. Loudianos, G., & Gitlin, J. D. (2000) Wilson's Disease. *Semin. Liver Dis.* **20**, 353-364.

13. Gitlin, J. D. (2003) Wilson Disease. *Gastroenterology* **125**, 1868-1877.

14. Kitzberger, R., Madl, C., & Ferenci, P. (2005) Wilson Disease. *Metab. Brain Dis.* **20**, 295-302.

15. Bush, A. I. (2003) Copper, Zinc, and the Metallobiology of Alzheimer Disease. *Alzheimer Dis. Assoc. Dis.* **17**, 147-150.

16. Bush, A. I. (2000) Metals and Neuroscience. *Curr. Opin. Chem. Biol.* **4**, 184-191.

17. Gaggelli, E., Kozlowski, H., Valensin, D., & Valensin, G. (2006) Copper Homeostasis and Neurodegenerative Disorders (Alzheimer's, Prion, and Parkinson's Diseases and Amyotrophic Lateral Sclerosis). *Chem. Rev.* **106**, 1995-2044.

18. Barnham, K. J., & Bush, A. I. (2008) Metals in Alzheimer's and Parkinson's Diseases. *Curr. Opin. Chem. Biol.* **12**, 222-228.

19. Macreadie, I. G. (2008) Copper Transport and Alzheimer's Disease. *Eur. Biophys. J. Biophys. Lett.* **37**, 295-300.

20. Carri, M. T., Ferri, A., Cozzolino, M., Calabrese, L., & Rotilio, G. (2003) Neurodegeneration in Amyotrophic Lateral Sclerosis: The Role of Oxidative Stress and Altered Homeostasis of Metals. *Brain Res. Bull.* **61**, 365-374.

21. Wijesekera, L. C., & Leigh, P. N. (2009) Amyotrophic Lateral Sclerosis. *Orphanet J. Rare Dis.* **4**, 22.

22. Rae, T. D., Schmidt, P. J., Pufahl, R. A., Culotta, V. C., & O'halloran, T. V. (1999) Undetectable Intracellular Free Copper: The Requirement of a Copper Chaperone for Superoxide Dismutase. *Science* **284**, 805-808.

23. Finney, L. A., & O'halloran, T. V. (2003) Transition Metal Speciation in the Cell: Insights from the Chemistry of Metal Ion Receptors. *Science* **300**, 931-936.

24. Waldron, K. J., Rutherford, J. C., Ford, D., & Robinson, N. J. (2009) Metalloproteins and Metal Sensing. *Nature* **460**, 823-830.

25. Elam, J. S., Thomas, S. T., Holloway, S. P., Taylor, A. B., & Hart, P. J. (2002) Copper Chaperones. **60**, 151-219.

26. Rosenzweig, A. C. (2001) Copper Delivery by Metallochaperone Proteins. *Accounts Chem. Res.* **34**, 119-128.

27. Huffman, D. L., & O'halloran, T. V. (2001) Function, Structure, and Mechanism of Intracellular Copper Trafficking Proteins. *Annu. Rev. Biochem.* **70**, 677-701.

28. O'halloran, T. V., & Culotta, V. C. (2000) Metallochaperones, an Intracellular Shuttle Service for Metal Ions. **275**, 25057-25060.

29. Luk, E., Jensen, L. T., & Culotta, V. C. (2003) The Many Highways for Intracellular Trafficking of Metals. **8**, 803-809.

30. Culotta, V. C., Yang, M., & O'halloran, T. V. (2006) Activation of Superoxide Dismutases: Putting the Metal to the Pedal. *Biochim. Biophys. Acta-Mol. Cell Res.* **1763**, 747-758.

31. Rothstein, J. D., Becker, M., Hoberg, M. D., Culotta, V., Corson, L., Cleveland, D., et al. (1998) Ccs: A New Copper Chaperone Protein That May Contribute to Familial Amyotrophic Lateral Sclerosis. *Ann. Neurol.* **44**, 7.

32. Abajian, C., Yatsunyk, L. A., Ramirez, B. E., & Rosenzweig, A. C. (2004) Yeast Cox17 Solution Structure and Copper(I) Binding. *J. Biol. Chem.* **279**, 53584-53592.

33. Glerum, D. M., Shtanko, A., & Tzagoloff, A. (1996) Characterization of Cox17, a Yeast Gene Involved in Copper Metabolism and Assembly of Cytochrome Oxidase. *J. Biol. Chem.* **271**, 14504-14509.

34. Pierrel, F., Cobine, P. A., & Winge, D. R. (2007) Metal Ion Availability in Mitochondria. *Biometals* **20**, 675-682.

35. Horng, Y. C., Cobine, P. A., Maxfield, A. B., Carr, H. S., & Winge, D. R. (2004) Specific Copper Transfer from the Cox17 Metallochaperone to Both Sco1 and Cox11 in the Assembly of Yeast Cytochrome C Oxidase. *J. Biol. Chem.* **279**, 35334-35340.

36. Hamza, I., Prohaska, J., & Gitlin, J. D. (2003) Essential Role for Atox1 in the Copper-Mediated Intracellular Trafficking of the Menkes Atpase. *Proc. Natl. Acad. Sci. U. S. A.* **100**, 1215-1220.

37. Hamza, I., Faisst, A., Prohaska, J., Chen, J., Gruss, P., & Gitlin, J. D. (2001) The Metallochaperone Atox1 Plays a Critical Role in Perinatal Copper Homeostasis. *Proc. Natl. Acad. Sci. U. S. A.* **98**, 6848-6852.

38. Pufahl, R. A., Singer, C. P., Peariso, K. L., Lin, S. J., Schmidt, P. J., Fahrni, C. J., et al. (1997) Metal Ion Chaperone Function of the Soluble Cu(I) Receptor Atx1. **278**, 853-856.

39. Petris, M. J., Mercer, J. F. B., Culvenor, J. G., Lockhart, P., Gleeson, P. A., & Camakaris, J. (1996) Ligand-Regulated Transport of the Menkes Copper P-Type Atpase Efflux Pump from the Golgi Apparatus to the Plasma Membrane: A Novel Mechanism of Regulated Trafficking. *Embo J.* **15**, 6084-6095.

40. Herd, S. M., Camakaris, J., Christofferson, R., Wookey, P., & Danks, D. M. (1987) Uptake and Efflux of Copper-64 in Menkes-Disease and Normal Continuous Lymphoid-Cell Lines. *Biochem. J.* **247**, 341-347.

41. Vonk, W. I. M., Wijmenga, C., & Van De Sluis, B. (2008) Relevance of Animal Models for Understanding Mammalian Copper Homeostasis. *Am. J. Clin. Nutr.* **88**, 840S-845S.

42. Mcrae, R., Lai, B., & Fahrni, C. J. (2010) Copper Redistribution in Atox1-Deficient Mouse Fibroblast Cells. *J. Biol. Inorg. Chem.* **15**, 99-105.

43. Lin, S. J., & Culotta, V. C. (1995) The Atx1 Gene of Saccharomyces-Cerevisiae Encodes a Small Metal Homeostasis Factor That Protects Cells against Reactive Oxygen-Toxicity. *Proc. Natl. Acad. Sci. U. S. A.* **92**, 3784-3788.

44. Itoh, S., Kim, H. W., Nakagawa, O., Ozumi, K., Lessner, S. M., Aoki, H., et al. (2008) Novel Role of Antioxidant-1 (Atox1) as a Copper-Dependent Transcription Factor Involved in Cell Proliferation. *J. Biol. Chem.* **283**, 9157-9167.

45. Mcrae, R., Bagchi, P., Sumalekshmy, S., & Fahrni, C. J. (2009) In Situ Imaging of Metals in Cells and Tissues. *Chem. Rev.* **109**, 4780-4827.

46. Fahrni, C. J. (2007) Biological Applications of X-Ray Fluorescence Microscopy: Exploring the Subcellular Topography and Speciation of Transition Metals. *Curr. Opin. Chem. Biol.* **11**, 121-127.

47. Lobinski, R., Moulin, C., & Ortega, R. (2006) Imaging and Speciation of Trace Elements in Biological Environment. *Biochimie* **88**, 1591-1604.

48. Ortega, R., Deves, G., & Carmona, A. (2009) Bio-Metals Imaging and Speciation in Cells Using Proton and Synchrotron Radiation X-Ray Microspectroscopy. *J. R. Soc. Interface* **6**, S649-S658.

49. Paunesku, T., Vogt, S., Maser, J., Lai, B., & Woloschak, G. (2006) X-Ray Fluorescence Microprobe Imaging in Biology and Medicine. *J. Cell. Biochem.* **99**, 1489-1502.

50. Yang, L. C., Mcrae, R., Henary, M. M., Patel, R., Lai, B., Vogt, S., et al. (2005) Imaging of the Intracellular Topography of Copper with a Fluorescent Sensor and by Synchrotron X-Ray Fluorescence Microscopy. *Proc. Natl. Acad. Sci. U. S. A.* **102**, 11179-11184.

51. Finney, L., Mandava, S., Ursos, L., Zhang, W., Rodi, D., Vogt, S., et al. (2007) X-Ray Fluorescence Microscopy Reveals Large-Scale Relocalization and Extracellular Translocation of Cellular Copper During Angiogenesis. *Proc. Natl. Acad. Sci. U. S. A.* **104**, 2247-2252.

52. Carmona, A., Cloetens, P., Deves, G., Bohic, S., & Ortega, R. (2008) Nano-Imaging of Trace Metals by Synchrotron X-Ray Fluorescence into Dopaminergic Single Cells and Neurite-Like Processes. *J. Anal. At. Spectrom.* **23**, 1083-1088.

53. Miyayama, T., Suzuki, K. T., & Ogra, Y. (2009) Copper Accumulation and Compartmentalization in Mouse Fibroblast Lacking Metallothionein and Copper Chaperone, Atox1. *Toxicol. Appl. Pharmacol.* **237**, 205-213.

54. La Fontaine, S., & Mercer, J. F. B. (2007) Trafficking of the Copper-Atpases, Atp7a and Atp7b: Role in Copper Homeostasis. *Arch. Biochem. Biophys.* **463**, 149-167.

55. Mcrae, R., Lai, B., Vogt, S., & Fahrni, C. J. (2006) Correlative Microxrf and Optical Immunofluorescence Microscopy of Adherent Cells Labeled with Ultrasmall Gold Particles. *J. Struct. Biol.* **155**, 22-29.

56. Vogt, S., Maser, J., & Jacobsen, C. (2003) Data Analysis for X-Ray Fluorescence Imaging. *J. Phys. IV* **104**, 617-622.

CHAPTER 6
METAL REDISTRIBUTION DURING THE MAMMALIAN CELL CYCLE

6.1 Roles for Metal Ions in the Mammalian Cell Cycle

Copper and zinc are ubiquitous in nature and required for cellular vitality. Copper is quite different from zinc in that it is redox active while zinc is essentially chemically inert [1]. Despite this major difference, both transition metals play structural and/or functional roles in at least 1/3 of the proteins and enzymes in the mammalian proteome and are often coordinated by similar ligands [1]. Cells must maintain a homeostatic balance of intracellular copper and zinc at non-toxic levels in order to ensure they are available to fulfill their respective roles. The need for a homeostatic balance of copper and zinc by cells is indeed underscored by the established links existing between the intracellular dyshomeostasis of copper in the onset and progression of severe neurological diseases such as Menkes disease [2, 3] and Wilson's disease [4-6], zinc de-regulation in diabetes [7], and both copper and zinc dyshomoestasis in Alzheimer's disease [8-16] and Parkinson's disease [8, 10, 11, 13-16].

The replication of mammalian cells is tightly regulated by a complex interplay of biochemical signals which facilitate a well orchestrated series of events that ultimately lead to the duplication of cellular DNA and division of a cell into two daughter cells each with equal and accurate copies of the original genetic information [17]. Whereas cell proliferation is tightly controlled in normal tissues, it is a highly de-regulated process during the progression of diseases such as cancer [17]. Hence, the elucidation of the

precise factors and underlying mechanisms involved in cell cycle progression represents an area of intense research efforts.

The mammalian cell cycle may be divided into four distinct phases: Gap 1 (G1), Synthesis (S), Gap 2 (G2), and mitosis (M) [17]. Progression from one phase to the next is intricately regulated and has many "checkpoints" that serve to account for the current cellular status and existing environmental cues [17]. Despite the wealth of information already revealed through years of extensive research investigations, a vast array of questions regarding fundamental aspects of the mammalian cell cycle remain unanswered. Examples of such ambiguities include those concerning the precise mechanisms involved in governing chromatin condensation during mitosis for accurate segregation of duplicated chromosomes into daughter cells [18]. Another question involves elucidating the mechanisms responsible for the formation, organization, and movement of spatially distinct nuclear domains, including chromosome territories and interchromatin granule clusters, which are involved in key events such as DNA replication, transcription, and RNA processing [18]. The underlying mechanisms facilitating nuclear envelope breakdown and re-assembly, occurring at the beginning and end of mitosis, respectively [18] are not well understood. Another example of ambiguity encompasses the mechanisms by which a cell determines and controls the size, number, spatial positioning, and shape of its organelles [19].

Given the large number of roles already identified for copper and zinc, it is conceivable that these two metals may very well play fundamental roles facilitating the progression of mammalian cells through their complex cell cycle. Indeed a significant

number of reports have indicated that both copper and zinc play a critical role in the proliferation of both healthy cells and tumor cells. Adequate copper nutrition during pregnancy and lactation [20] as well as sufficient levels of maternal zinc [21] were recently shown to be critical for the normal development of offspring. Furthermore, an inadequate intake of nutritional zinc directly contributes to deficiencies in bone development [22] and was also shown to promote overall growth retardation in addition to the development of congenital malformations [23, 24].

At the cellular level, zinc deprivation was reported to lead to an inhibition of cell proliferation [25] through cell cycle arrest at G1 phase [26, 27], S phase [27, 28], or G2 phase [27, 29] with an ultimate global failure of cells to undergo mitosis, while zinc supplementation, not surprisingly, has been reported to promote the proliferation of healthy mouse cells [30]. Additionally, several reports have provided evidence of direct roles for zinc in DNA synthesis [30-33].

The formation of nascent vasculature (angiogenesis), a critical process in normal physiology, depends on the availability of copper [34-36]. Since angiogenesis is critical for tumor growth and metastasis [37], a number of copper chelating agents show an effective inhibition of tumor proliferation as well as the ability to induce necrosis or apoptosis [38-42]. Similarly, the addition of external zinc was demonstrated to stimulate growth and proliferation of tumor cells [43] while the application of zinc chelators inhibited proliferation and promoted the death of cancer cells [44]. Consequently, small molecule anti-tumor agents were specifically designed to chelate intracellular labile zinc and indeed showed potent anti-proliferation activity of tumor cells [45]. Additionally, the

process of wound healing, which also requires rapid cellular proliferation, depends on local levels of copper [46, 47] as well as zinc [48].

Despite the demonstrated importance of copper and zinc to cell proliferation, mechanisms related to their regulation, re-distribution, and ultimate partitioning into each daughter cell remain an enigma. Analytical methods such as inductively coupled plasma mass spectrometry (ICP-MS) permit quantitative analyses of metal concentration changes occurring in bulk samples [49]. However, ICP-MS cannot be used for the analysis of metal content within single cells and is consequently incapable of providing information regarding content changes occurring at specific stages of the cell cycle. Metal ion-selective fluorescent probes are commonly used for visualizing intracellular labile metal pools but unfortunately offer only an indirect way to visualize the metal of interest. Additionally, fluorescent probes rarely provide accurate quantitative information regarding changes in metal content and are often restricted to probing metal environments within cellular locations pre-determined by the inherent nature of their molecular architecture. Synchrotron radiation X-ray fluorescence (SXRF) microscopy offers the unique opportunity to quantitatively image elemental distributions of individual cells with submicron spatial resolution [50]. SXRF represents a powerful method for studying the speciation of trace elements without the need for isolation of cellular organelles or compartments, a strategy that is often plagued with artifacts due to metal re-distribution and sample contamination [50]. The present study takes advantage of the unique abilities of SXRF microscopy for investigating the quantitative changes occurring for elemental distributions as NIH 3T3 mouse fibroblast cells progress through the cell cycle.

6.2 Elemental Distributions and Correlations During the Mammalian Cell Cycle

Adherent cells were grown directly on an x-ray compatible substrate (silicon nitride), chemically fixed with paraformaldehyde, and air-dried overnight [50]. Individual cells were raster-scanned with a 0.2 μm step size using an excitation of 10.0 keV, yielding 2D maps for all biologically relevant first row transition elements [50]. The number of scans per cell cycle phase, however, was limited by lengthy acquisition times of around 4 h per cell.

Identifying the Cell Cycle Phase of Individual Cells

Prior to SXRF imaging, two fluorescence-based methods were utilized to identify cells in specific stages of the cell cycle. The Fluorescence Ubiquitination Cell Cycle Indicator (FUCCI), originally developed by Sakaue-Sawano and co-workers [51] was used to identify G1, G1/S, and G2 phase cells (Figure 6.1). The FUCCI sensor platform takes advantage of the complementary processes of production and degradation of two proteins, Cdt1 and geminin, throughout the mammalian cell cycle [51].

In this system, Cdt1 is tagged with an RFP reporter while geminin is tagged with a GFP reporter [51]. Geminin is broken down in the G1 phase of the cell cycle, leaving only Cdt1 tagged with RFP visible, while Cdt1 is degraded in the S, G2, and M phases thereby rendering only geminin tagged with GFP visible [51]. At the G1/S boundary, as Cdt1 levels are decreasing and geminin levels are increasing, both proteins are present allowing for the visualization of both green and red fluorescence, which yields yellow fluorescent nuclei upon overlay of the two fluorescent signals [51]. In the present study, the FUCCI sensor was successfully utilized to classify cells at the G1, G1/S, and G2

stages of the cell cycle (Figure 6.1) for comparison of their elemental distributions with SXRF imaging.

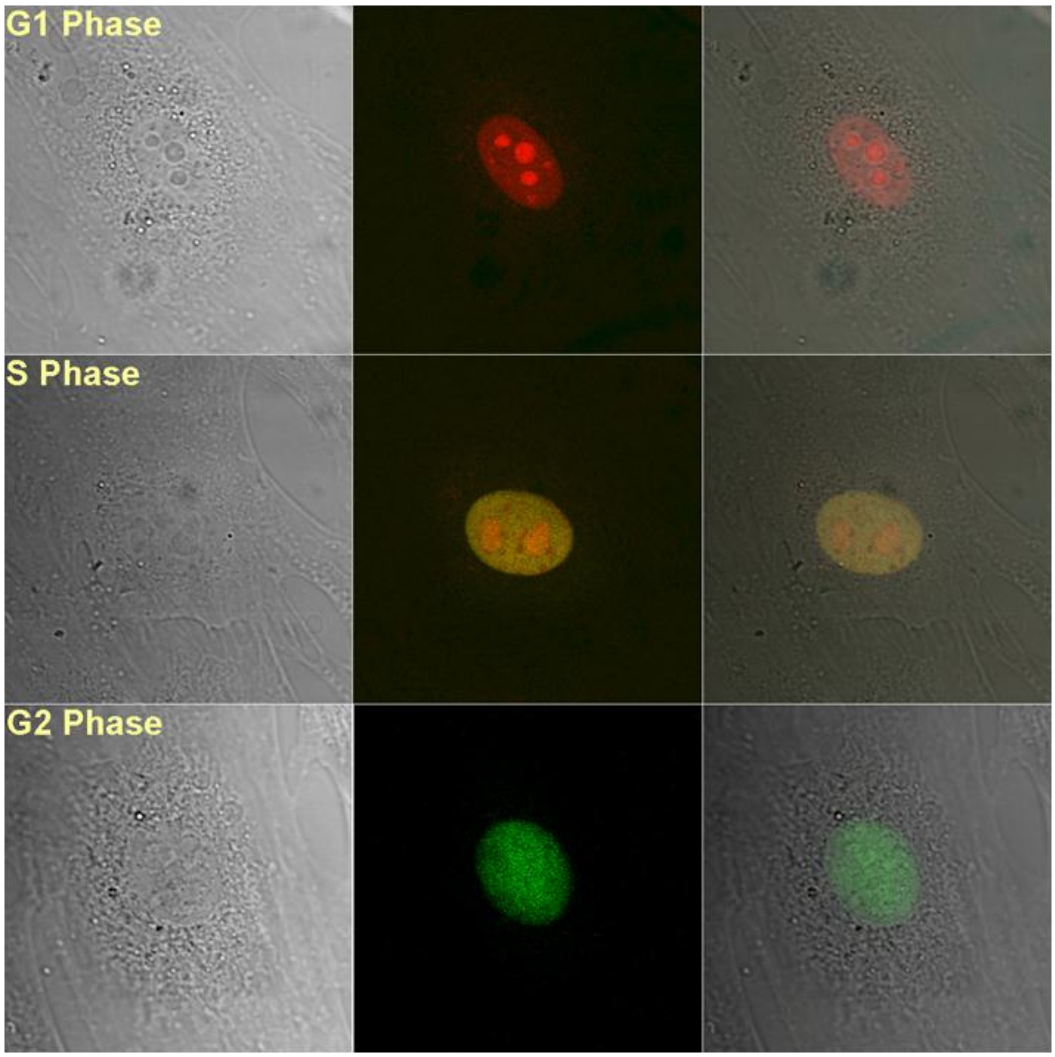

Figure 6.1: Cells labled with the FUCCI sensor for classification of their phase of interphase in the cell cycle. (left) DIC image of NIH 3T3 cell in interphase. (middle) Confocal fluorescence image of the FUCCI reporters for G1 phase (top; red), G1/S phase (middle; yellow), and G2 phase (bottom; green) cells. (right) Overlay image of the DIC and FUCCI sensor fluorescence.

A bis-benzimidazole dye, Hoechst 33258 [52-54], was used to identify cells at the individual stages of mitosis (Figure 6.2). Hoechst acts as a DNA intercalator and hence highlights the arrangement of a cell's chromosomes upon binding to DNA [52-54], which is morphologically distinct for each stage of mitosis. Based on the changes in chromosome morphology, single cells occurring in prophase, metaphase, anaphase, and telophase were identified (Figure 6.2).

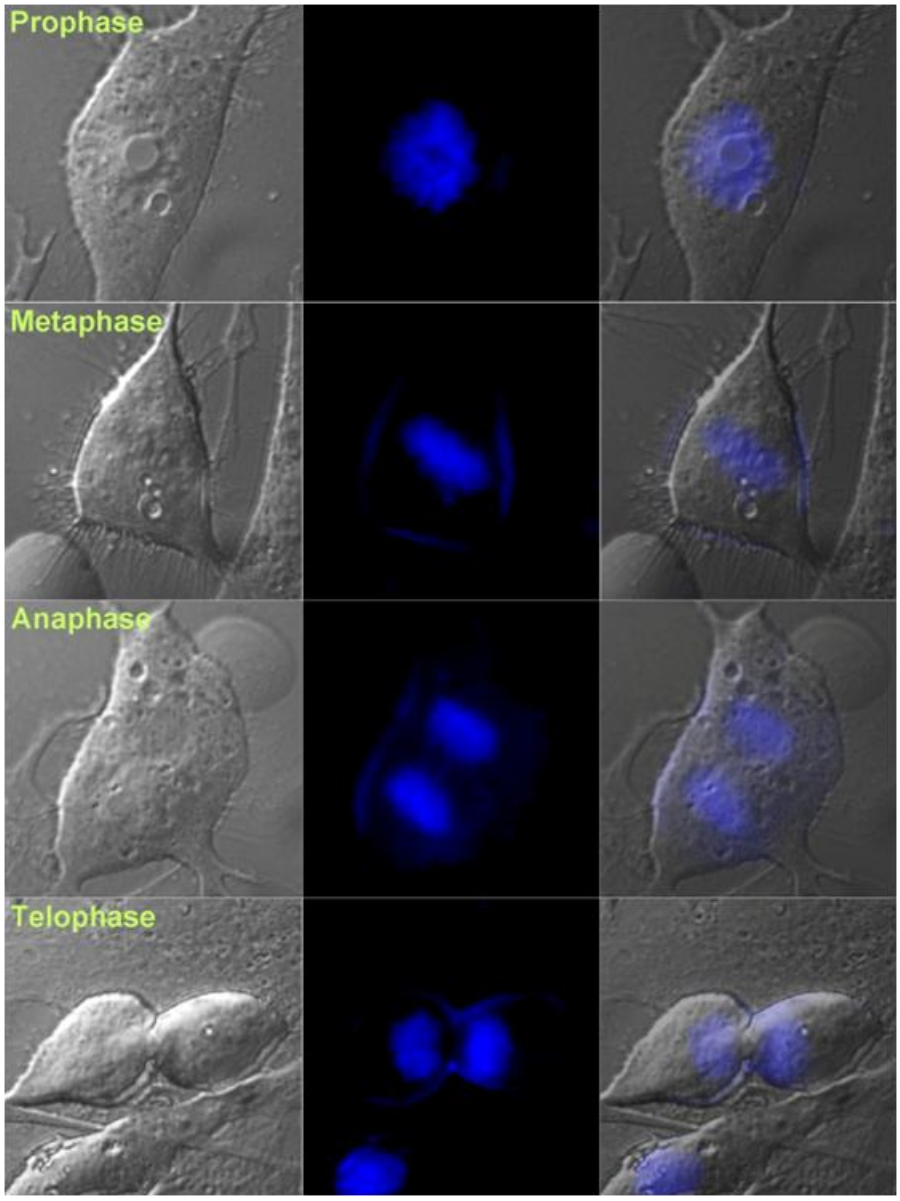

Figure 6.2: Identification of the mitotic phase of fixed NIH 3T3 mouse fibroblasts stained with Hoechst 33258 dye. (left) DIC image of air-dried NIH 3T3 cell in mitosis. (middle) Optical fluorescence image of the cell nucleus labeled with Hoechst 33258 illustrating the mitotic stage. (right) Overlay image of the DIC and Hoechst fluorescence.

Interphase

Following the identification of cells in specific stages of the cell cycle, the distributions of Cu, Zn, S, and P and the correlations in localization existing for elemental

pairs including Cu/S, Cu/P, Zn/S, and Zn/P were investigated with SXRF microscopy. Copper showed a rather homogenous distribution throughout the cell cytoplasm and nucleus with no obvious variations occurring between G1, G1/S, and G2 cells (Figure 6.3). Additionally, copper appeared slightly elevated in peri-nuclear regions, and it also concentrated in a few localized areas or "hot spots" within the nucleus (Figure 6.3), a distribution consistent with that observed in previous reports of SXRF copper distributions in mammalian cells [50, 55, 56].

Zinc, similar to both phosphorus and sulfur, also showed a homogenous intracellular distribution for G1, G1/S, and G2 cells and a notably higher fluorescence signal within the nucleus (Figure 6.3). This enhanced nuclear SXRF signal observed is not surprising given the large number of zinc-finger proteins localized within the cell nucleus [57, 58].

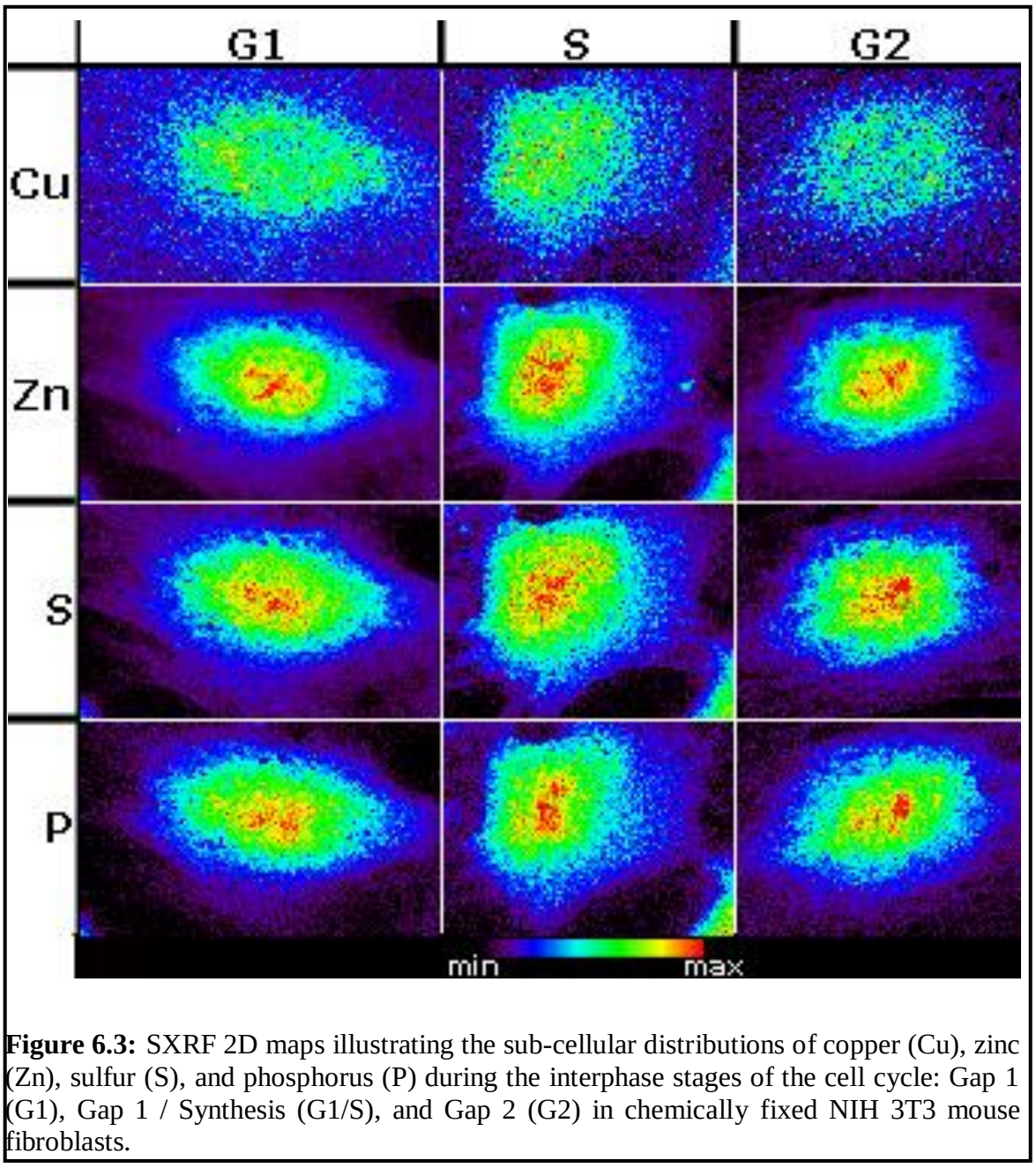

Figure 6.3: SXRF 2D maps illustrating the sub-cellular distributions of copper (Cu), zinc (Zn), sulfur (S), and phosphorus (P) during the interphase stages of the cell cycle: Gap 1 (G1), Gap 1 / Synthesis (G1/S), and Gap 2 (G2) in chemically fixed NIH 3T3 mouse fibroblasts.

In order to obtain a quantitative view of the degree of co-localization between different elements, a pixel-by-pixel correlation analysis of elemental positions with respect to one another was performed using the MAPS and PROFIT software packages. Correlation coefficients represent the statistical relationships existing between two or more observed data values that imply the possibility of causal or mechanistic

relationships existing between the data values. A high correlation coefficient denotes a strong relationship exists between the data values of interest.

Copper showed a rather modest correlation with both sulfur and phosphorus exhibiting correlation coefficients of around 0.78 and 0.76, respectively, both for G1 and G1/S phases and slightly lower coefficients of 0.72 and 0.69 for G2 phase cells (Figure 6.4). In contrast, the correlation for zinc with both sulfur and phosphorus was much stronger with an average correlation coefficient of approximately 0.9 for G1, G1/S, and G2 phases (Figure 6.4).

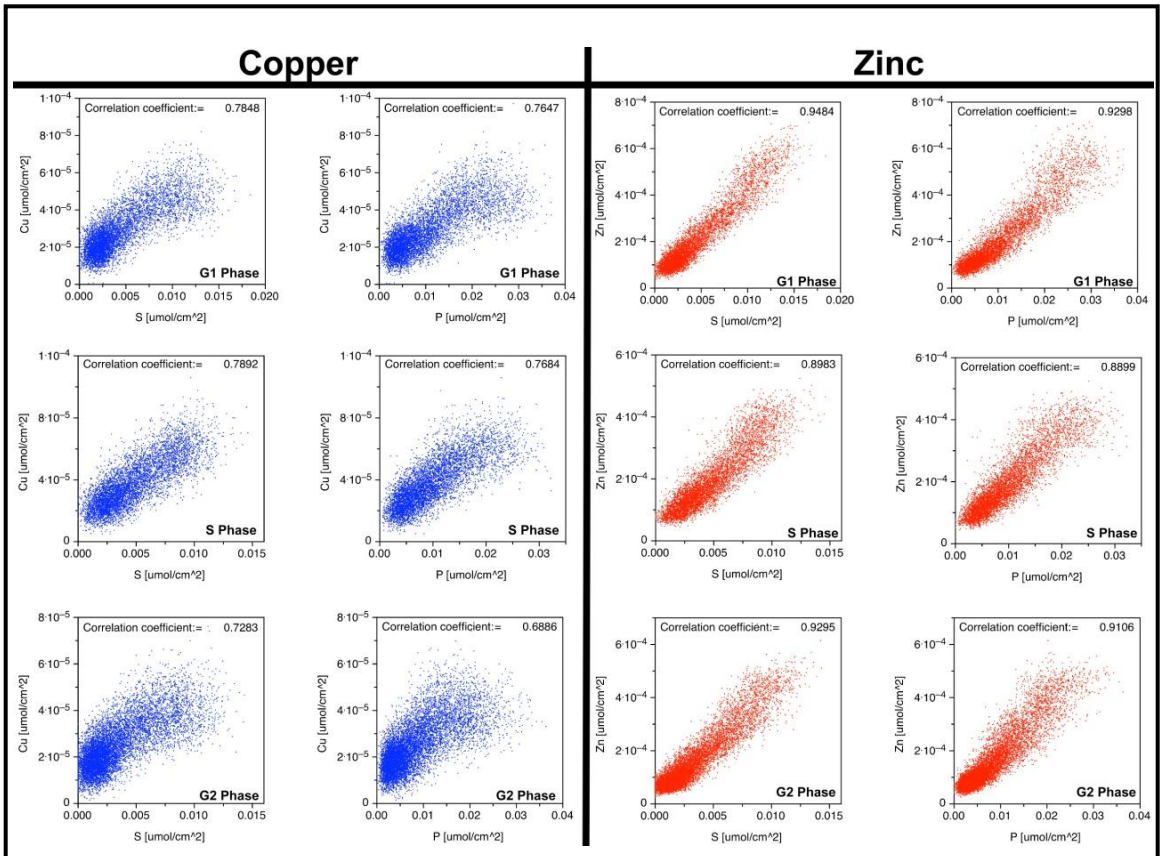

Figure 6.4: Plots illustrating the degree of correlation occurring between the intracellular localizations of individual elements during interphase. **(left)** Degree of correlation occurring for copper and sulfur (1st column) and for copper and phosphorus (2nd column) during G1 (top), G1/S (middle), and G2 (bottom). **(right)** Degree of correlation occurring for zinc and sulfur (1st column) and for zinc and phosphorus (2nd column) during G1 (top), G1/S (middle), and G2 (bottom).

This strong correlation is not surprising given the observed similarities in their distributions (Figure 6.3). Moreover, previous studies have revealed that zinc interacts directly with DNA to provide additional stability to the phosphate backbone [59, 60] and

is also bound to a large number of both phosphorus rich and sulfur rich proteins localized throughout the cell [58, 61, 62].

Mitosis

Compared with interphase cells, a striking re-distribution of copper and zinc occurred as cells progressed through mitosis (Figure 6.5). During prophase (Figure 6.5; 1st column), the phosphorus map reveals the chromatin has condensed thereby rendering the duplicated chromosomes visible as threadlike structures, which have begun to migrate towards the middle of the cell. Copper and zinc show extensive overlap with regions of elevated sulfur and to a slightly lesser degree, with regions of elevated phosphorus as well.

During metaphase (Figure 6.5; 2nd column), the chromosomes are aligned on the spindle equator as illustrated by the phosphorus map. Interestingly, there is an even more striking co-localization of copper and zinc with regions of concentrated sulfur, which directly complement those of elevated phosphorus, presumably representing the aligned chromosomes. The distribution observed for copper, zinc, and sulfur with respect to phosphorus is reminiscent of that observed for the positioning of the microtubule-based mitotic spindle with respect to the chromosomes, whose movement and distribution it directly facilitates during cell division [63].

During anaphase (Figure 6.5; 3rd column), the sister chromatids have separated and begun to migrate towards separate poles (P map). Both copper and zinc dramatically re-locate to the midzone of the dividing cell, while also simultaneously remaining in concentrated pools, although to a lesser extent, at each pole. As observed during

metaphase, each region of concentrated copper and zinc strongly co-localizes with regions of increased sulfur content again directly complementing regions of concentrated phosphorus.

Finally during telophase/cytokinesis (Figure 6.5; 4th column), the daughter chromosomes have arrived at opposite poles (P map) and the midzone pools of copper and zinc are re-distributed to the daughter cells. The twin pools of copper and zinc, which appeared during anaphase at opposite poles, are still visible in this cell at late telophase/early cytokinesis.

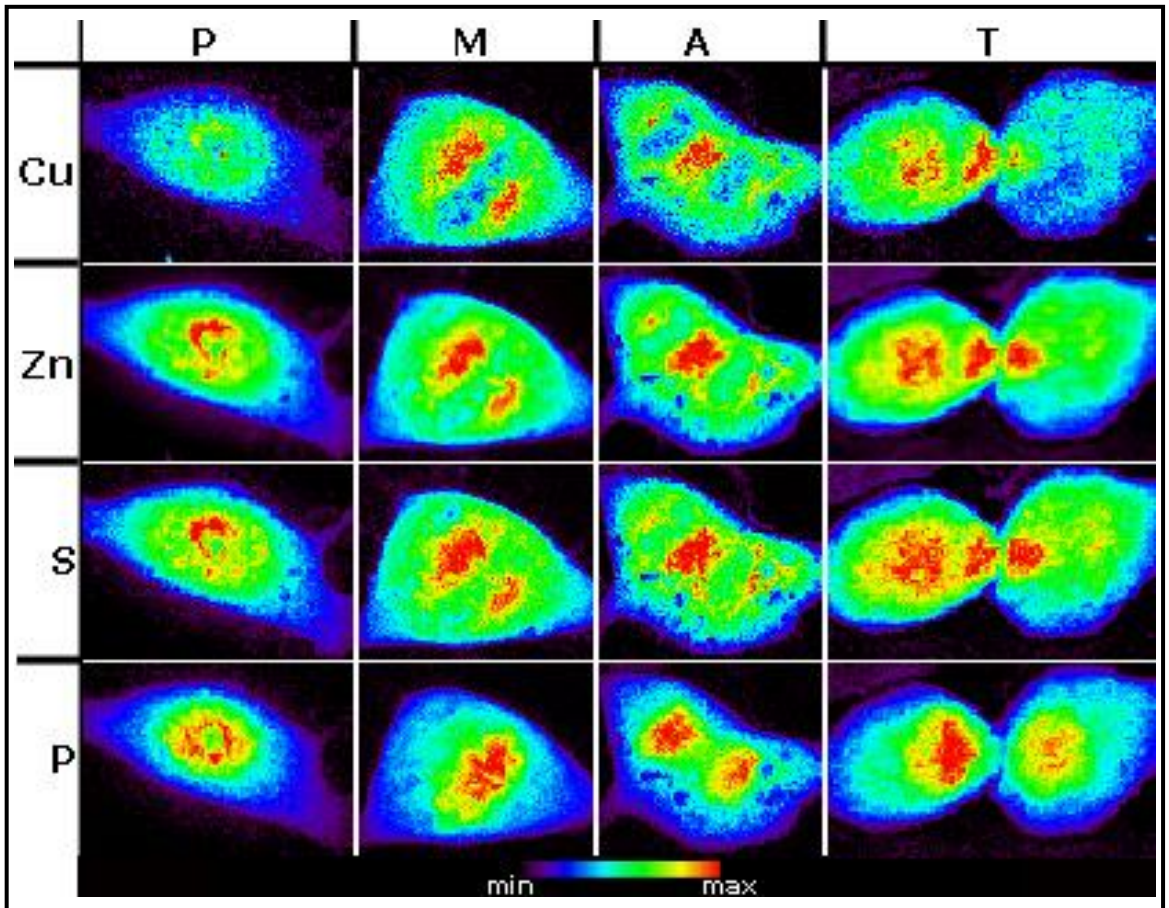

Figure 6.5: SXRF 2D maps showing the sub-cellular distributions of copper (Cu), zinc (Zn), sulfur (S), and phosphorus (P) during the stages of mitosis: prophase (P), metaphase (M), anaphase (A), and telophase (T) in chemically fixed NIH 3T3 mouse fibroblasts.

A similar morphogenesis was observed for the inheritance of the Golgi apparatus in an earlier report that employed a combination of live cell imaging and high-resolution electron microscopy methods to reveal that Golgi re-assembly at the end of mitosis is preceded by the formation of four co-linear clusters at telophase, two per daughter cell [64]. Within each daughter, the smaller cluster near the midbody gradually migrates to re-join the major cluster on the far side of the nucleus and asymmetrically reconstitutes a single Golgi apparatus [64]. The above observations of metal pools localized in regions analogous to those observed for the Golgi twins appearing in late anaphase and early telophase suggest a potential role for copper and zinc in Golgi inheritance late in cell division.

Pixel-by-pixel correlation data revealed significantly stronger correlations for copper and sulfur (correlation coefficient ≈ 0.9) and for zinc and sulfur (correlation coefficient > 0.95) throughout mitosis (Figure 6.6) compared with analogous correlations reported above for cells in interphase (Figure 6.4). As indicated by the XRF distribution images (Figure 6.5), a major decrease in correlation occurred for Cu and P as well as Zn and P (Figure 6.6). For both copper and zinc, the trend showed a major drop in the degree of correlation of these metals with phosphorus from prophase to metaphase and a gradual increase from metaphase to telophase, although never reaching their initial level of correlation observed during prophase (Figure 6.6).

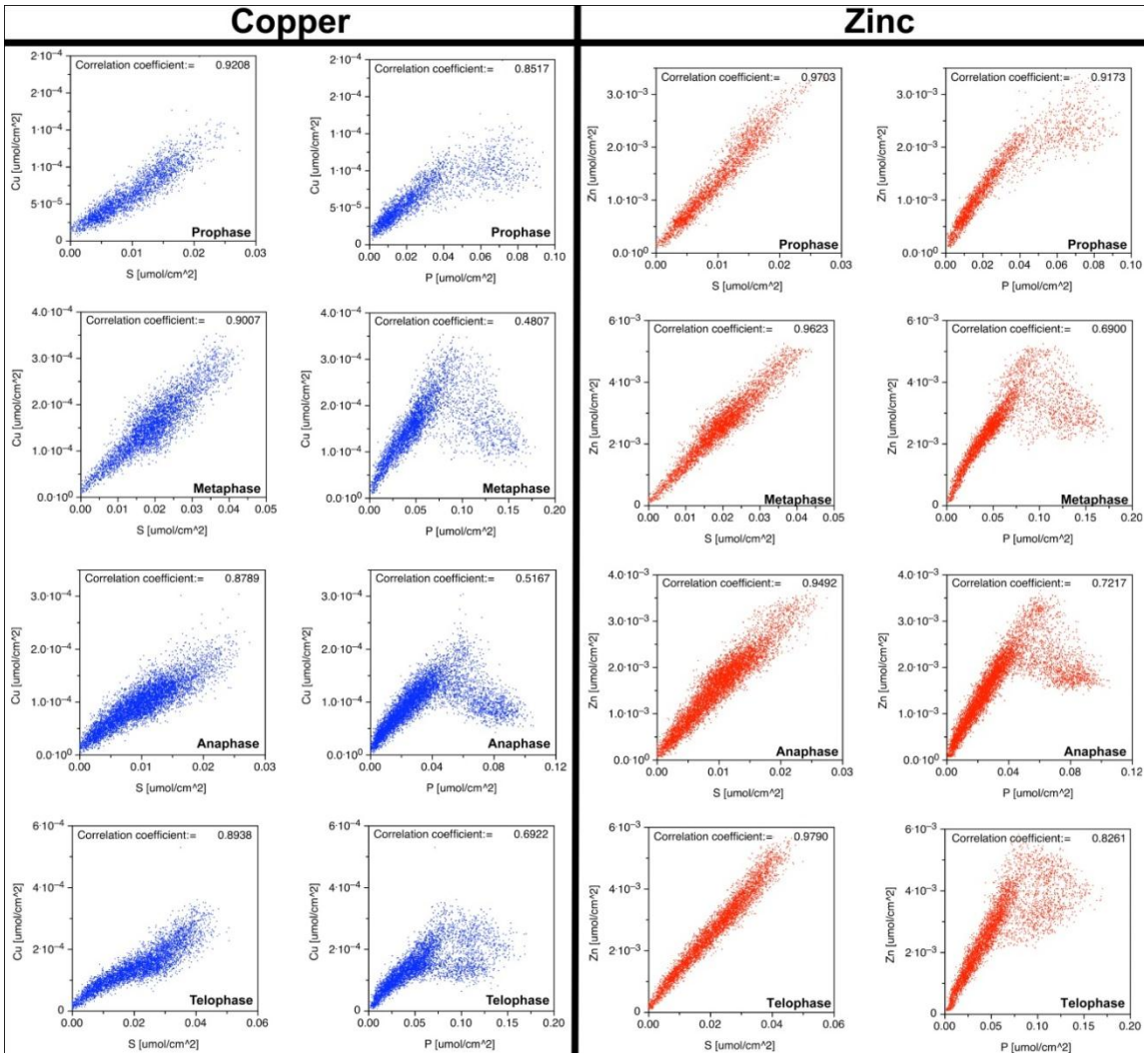

Figure 6.6: Plots illustrating the degree of correlation occurring between the intracellular localizations of individual elements during mitosis. **(left)** Degree of correlation occurring for copper and sulfur (1st column) and for copper and phosphorus (2nd column) during prophase (1st row), metaphase (2nd row), anaphase (3rd row) and telophase (4th row). **(right)** Degree of correlation occurring for zinc and sulfur (1st column) and for zinc and phosphorus (2nd column) during prophase (1st row), metaphase (2nd row), anaphase (3rd row) and telophase (4th row).

This strongly implies a movement towards an environment rich in sulfur ligands compared with an environment equally rich in both sulfur and phosphorus ligands for zinc and copper during cell division.

6.3 Mass Balance of Elements Throughout the Cell Cycle

The considerable size of adherent fibroblast cells combined with the necessity to obtain elemental distribution maps with high spatial resolution (200 nm x 200 nm) resulted in long data acquisition times of about 4 h per cell and hence limited the sample size to only 3-5 repeats for each cell cycle phase. To account for differences in cell thickness that may potentially contribute to differences in elemental content, all quantitative data described here are presented as the total number of femtomoles (fmol) for individual elements in the region of interest (ROI) analyzed.

Changes in Total Content and Elemental Ratios

Quantitative analysis of the total copper content as cells progress through the cell cycle revealed a relatively unaltered amount of total copper for each stage (Figure 6.7; middle). Phosphorus showed a modest increase in content from G1 to mitotic cells (Figure 6.8; top), while sulfur showed a very slight decrease, if at all, in total levels (Figure 6.8; bottom).

In marked contrast to the observations for copper, phosphorus, and sulfur, zinc showed a striking 3-fold increase in total content, compared with G1 phase cells, during mitosis peaking at metaphase (Figure 6.7; top).

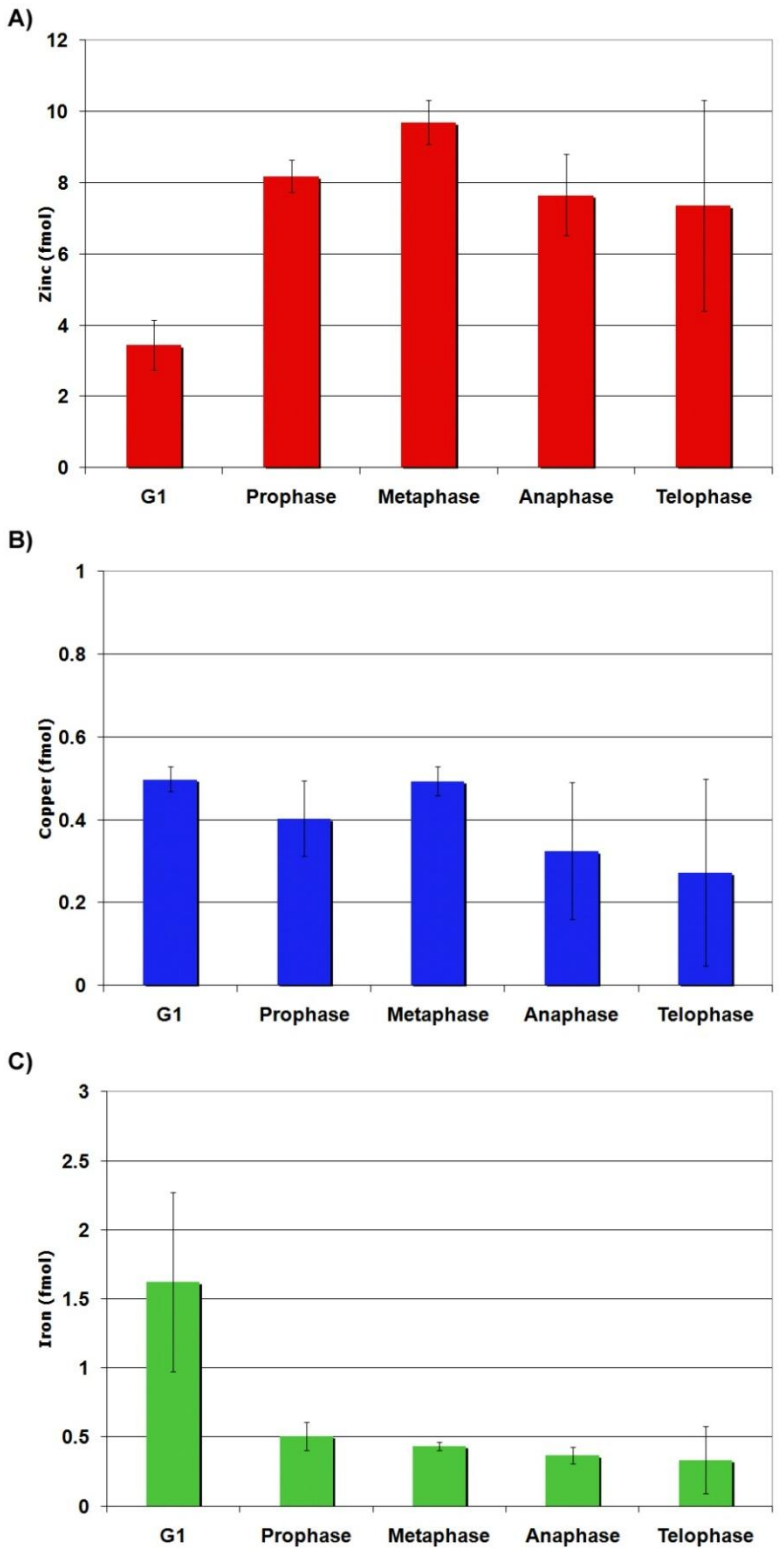

Figure 6.7: Trace metal contents of NIH 3T3 cells cultured in basal media and at different stages of the cell cycle. The synchrotron X-ray fluorescence (SXRF) data were quantitatively analyzed for the content of Zn **(a)**, Cu **(b)**, and Fe **(c)**.

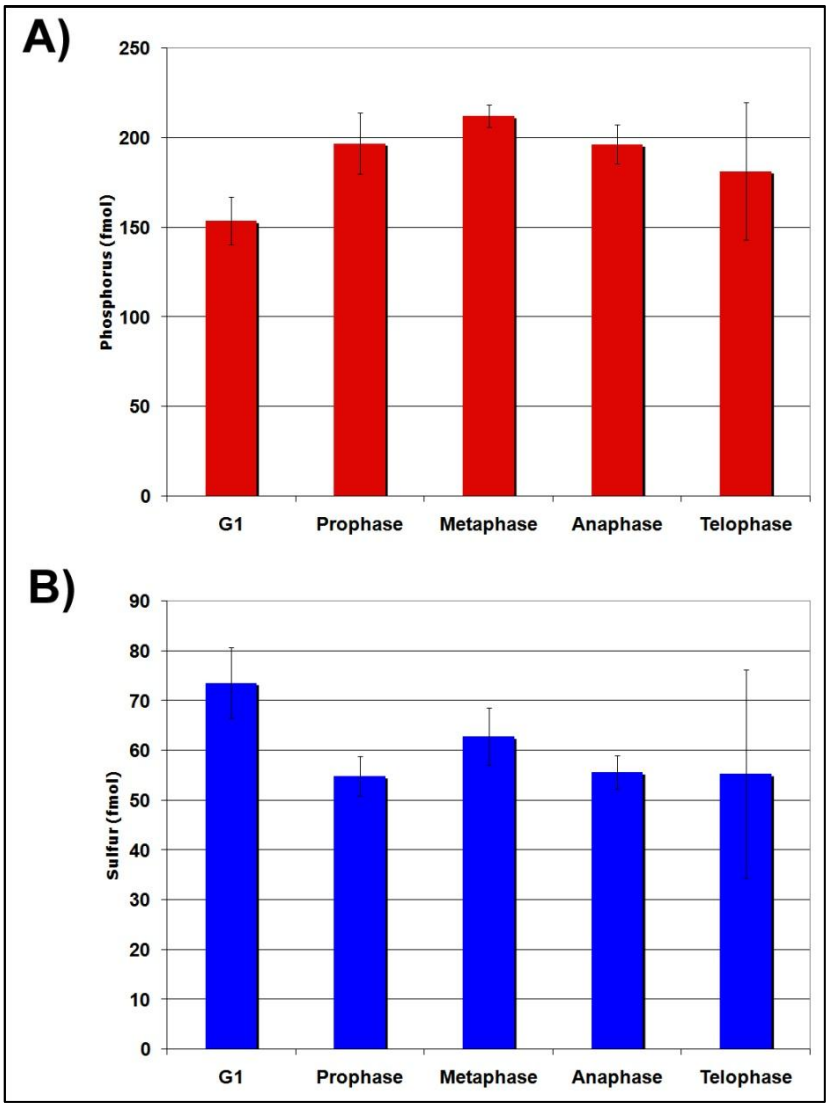

Figure 6.8: Content of elements in NIH 3T3 cells cultured in basal media and at different stages of the cell cycle. The synchrotron X-ray fluorescence (SXRF) data were quantitatively analyzed for the content of phosphorus **(a)** and sulfur **(b)**.

The strong increase in overall content together with the major re-distribution observed for zinc strongly imply the existence of specific roles for this metal during cell division. Similar effects have been observed for calcium during mitosis, albeit at the later stages [65-67]. These earlier studies, using a calcium-selective fluorescent probe,

illustrated the presence of required transient and localized spikes of calcium signals within the midbody for the proper completion by cells of late telophase and cytokinesis [65-67]. Although identical effects for zinc are yet to be reported in the literature, the suggestion of calcium playing critical roles during mitosis provides further support for the possibility that other metals such as zinc and copper may also serve vital functions during cell division.

Inspection of the S/Zn ratio (Figure 6.9; top) revealed a remarkable decrease from a value of approximately 20 for G1 phase cells to a ratio value of about six for mitotic cells. Given the observed 3-fold increase in total zinc content (Figure 6.7) and effectively unchanged sulfur content (Figure 6.8) for G1 versus mitotic cells, the striking decrease in the ratio of the number of moles of S to the number of moles of Zn strongly suggests a predominantly S-rich coordination environment for Zn during mitosis.

Alternatively, the S/Cu ratio (Figure 6.9; middle) showed a slight increase in mitotic cells compared with G1 phase cells, potentially suggesting a decreased coordination of copper by sulfur-rich ligands, despite the observed increase in correlation for their intracellular localizations (Figure 6.6), during mitosis.

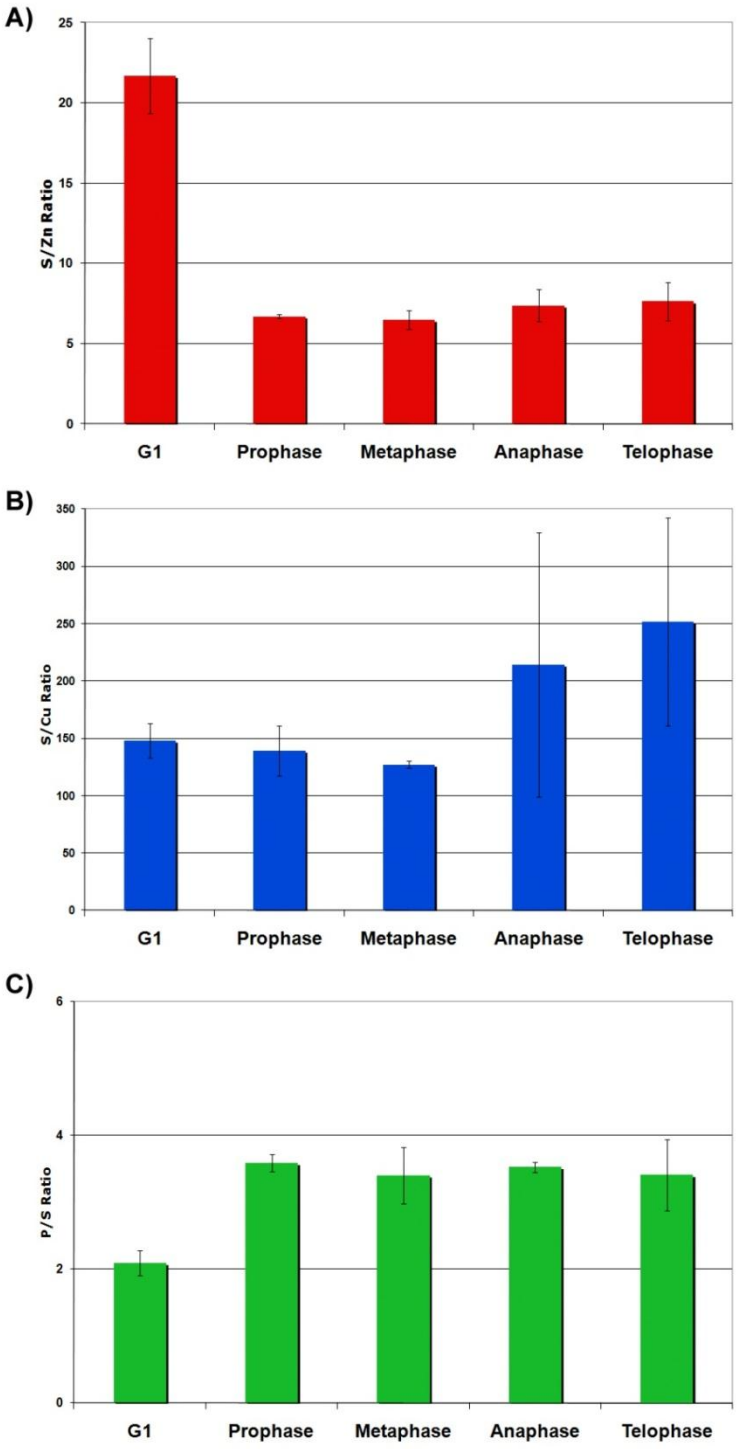

Figure 6.9: Elemental contents expressed as the ratio of elemental pairs in NIH 3T3 cells cultured in basal media and at different stages of the cell cycle. The synchrotron X-ray fluorescence (SXRF) data were quantitatively analyzed for the content ratios: S/Zn **(A)**, S/Cu **(B)**, and P/S **(C)**.

The major re-distribution and striking influx of zinc during mitosis combined with the aforementioned parallel between zinc and calcium increases during mitosis prompted a closer inspection of the zinc distribution compared with that of calcium during telophase/cytokinesis. SXRF 2D elemental maps of a late telophase/early cytokinesis cell demonstrated a rather homologous distribution for calcium and zinc (Figure 6.10) in which both metals concentrated within a small region at the middle of the cell's ingression (Figure 6.10; white arrows), which is presumably the midbody compartment.

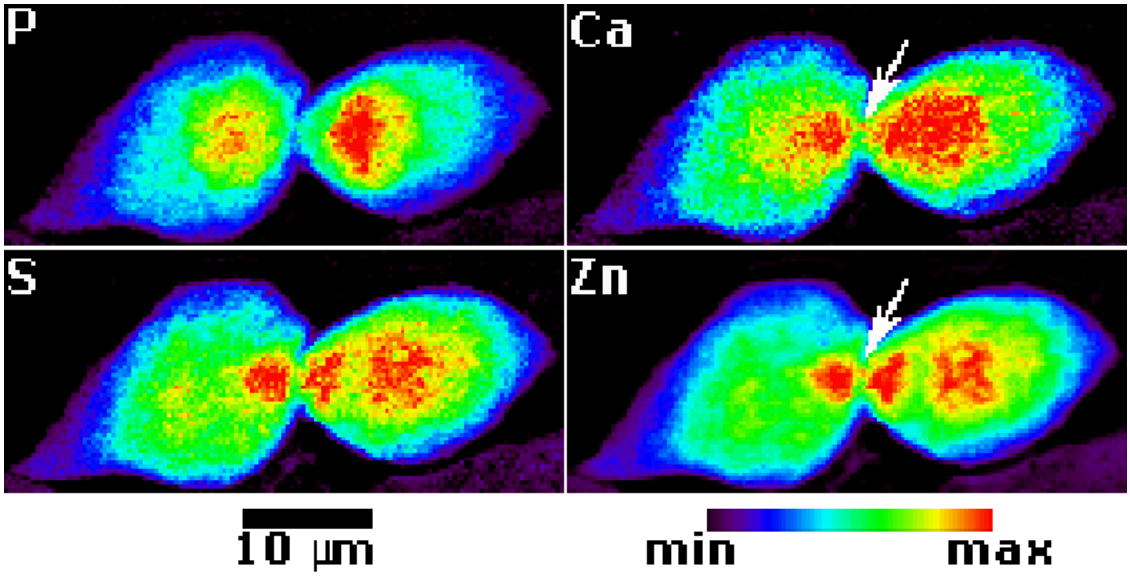

Figure 6.10: SXRF 2D maps showing the sub-cellular distributions of phosphorus (P), sulfur (S), calcium (Ca), and zinc (Zn) in a chemically fixed NIH 3T3 mouse fibroblast cell in late telophase/cytokinesis.

The mammalian midbody is a dense structure containing microtubules originating from the spindle midzone tightly bundled by the cytokinetic or cleavage furrow [68]. Despite the ambiguity associated with the exact function of the midbody, it is known to contain proteins indispensable for cytokinesis, asymmetric cell division, and chromosome

segregation [69-71]. The co-localization of zinc and calcium in the presumed midbody structure, where calcium has been previously suggested to serve important functions for the appropriate completion of cytokinesis [65-67], provides compelling evidence supporting a significant role for zinc as well during the late stages of cell division.

Previous literature reports of calcium spikes occurring at the midzone of dividing cells only during late telophase and cytokinesis [65-67], prompted a direct comparison of the zinc and calcium SXRF maps for a cell in late anaphase. Although some calcium is present in the midzone (Figure 6.11; white arrows), a majority remains concentrated in areas overlapping with phosphorus regions. Zinc, on the other hand, appears to be already quite concentrated in the midzone (white arrows), thus implying the roles for zinc during cell division may already be present long before calcium begins to serve its functions.

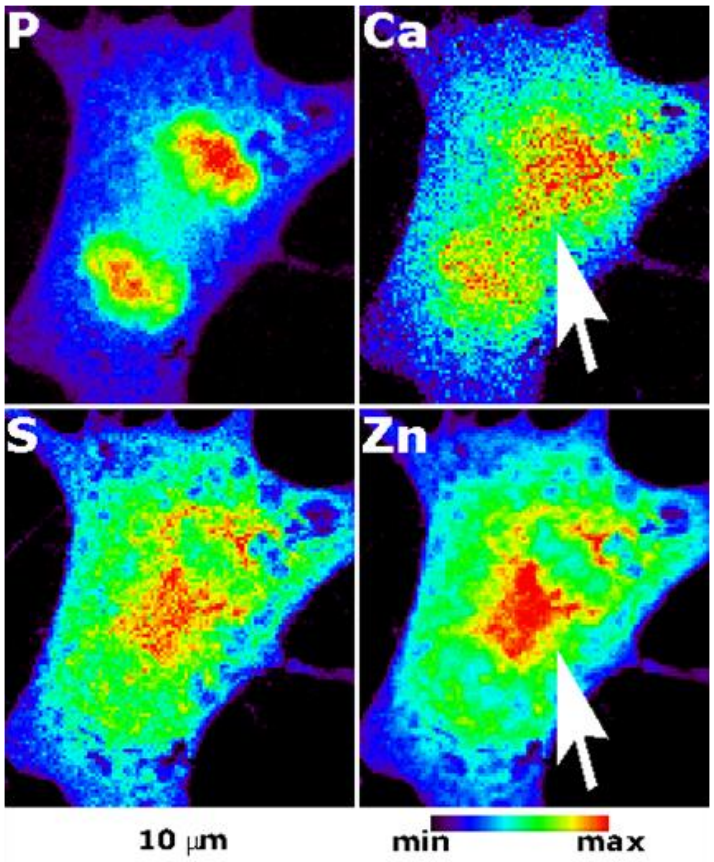

Figure 6.11: SXRF 2D maps showing the sub-cellular distributions of phosphorus (P), sulfur (S), calcium (Ca), and zinc (Zn) in a chemically fixed NIH 3T3 mouse fibroblast cell in mid-anaphase/late-anaphase.

Individual Daughter Cells vs. Interphase Cells

ROI's of individual daughter cells were drawn and quantitatively analyzed in order to compare the average elemental content of individual daughter cells with interphase cells. Interestingly, the average total amount of zinc observed for interphase cells was effectively the same as that of the individual daughters of cells in telophase/cytokinesis (Figure 6.12). On the contrary, the total amount of Cu, P, and S per daughter cell was approximately 1/5 of the average levels observed for interphase cells (Figure 6.12).

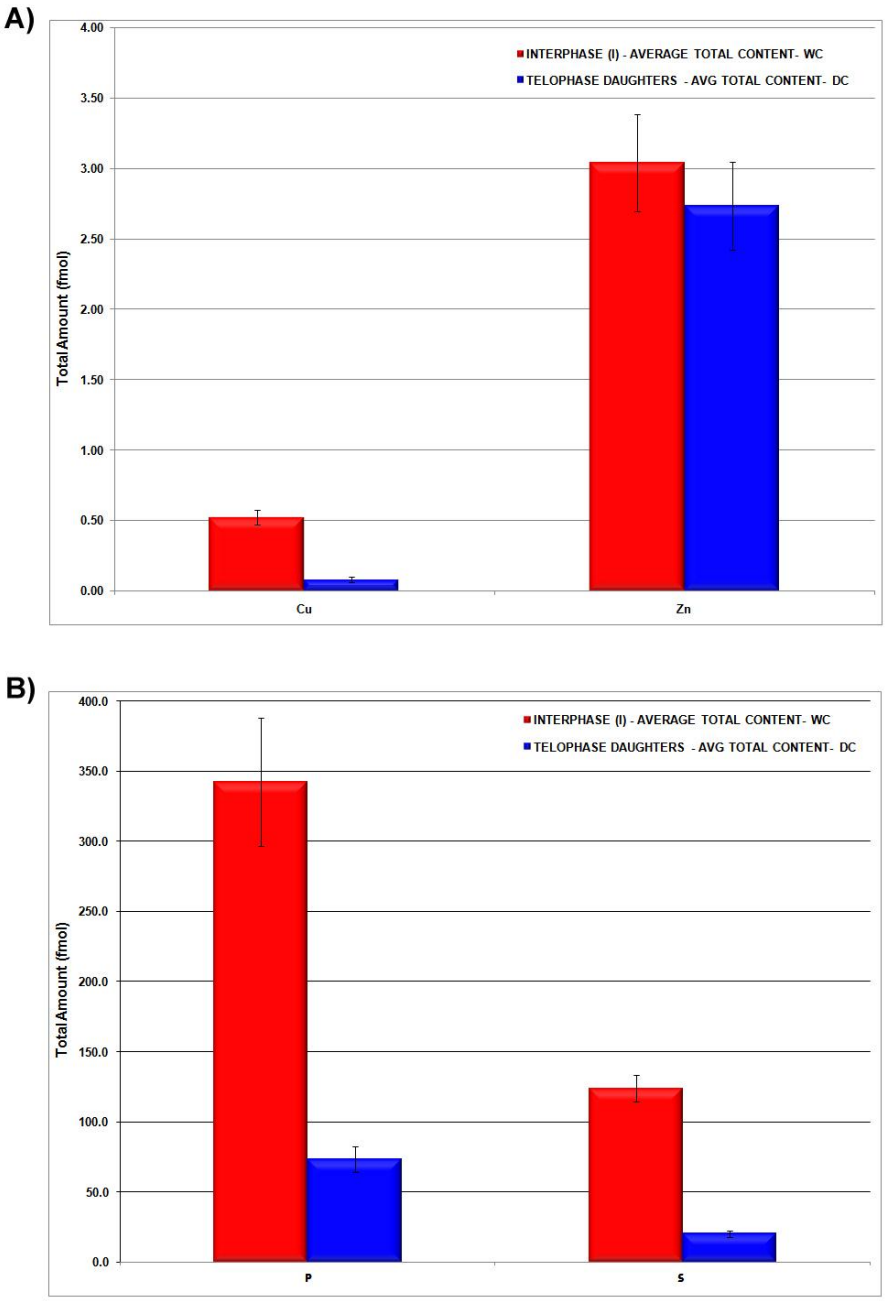

Figure 6.12: Content of elements in NIH 3T3 cells cultured in basal media and at different stages of the cell cycle. The synchrotron X-ray fluorescence (SXRF) data were quantitatively analyzed for: **(top)** the content of copper (Cu) and zinc (Zn) and **(bottom)** the content of phosphorus (P) and sulfur (S) for interphase cells (red) and indivudal daughters (blue) of cells in telophase/cytokinesis.

These data suggest that cells acquire their required amount of zinc during mitosis, while the acquisition of sufficient levels of Cu, P, and S is achieved at stages of the cell cycle other than mitosis.

6.4 Conclusions

Spatially well-resolved SXRF elemental maps of single, adherent mouse cells revealed remarkable changes in the distributions of both zinc and copper as the cells progressed through the cell cycle. Zinc and copper showed relatively homogenous nucleocytoplasmic distributions concentrating in regions of elevated sulfur as well as phosphorus for each stage of interphase. Conversely, upon the entry of cells into mitosis, zinc and copper moved from areas of significant phosphorus content to regions predominantly overlapping with sulfur. Furthermore, zinc showed an approximate 3-fold increase in its overall content upon the transition of cells from interphase into mitosis. Although SXRF, in the absence of a xenobiotic label, is unable to provide information regarding the nature of the cellular structures and/or organelles associated with copper and zinc, evidence strongly points toward their localization within the mitotic spindle. Moreover, the data strongly point towards an association with the Golgi apparatus, particularly for zinc, given the overall similarity between their distributions during cell division. Taken together, the data highlight the potential importance of zinc as well as copper for the appropriate progression of cells through mitosis, a previously unconsidered notion in reports investigating the mechanistic details underscoring the progression of mammalian cells through the cell cycle.

6.5 Materials and Methods

Cell Culture and Reagents

NIH 3T3 mouse fibroblasts were cultured in Dulbecco's Modified Eagle's Medium (DMEM, GIBCO-BRL, Gaithersburg, USA) supplemented with 10% bovine serum (GIBCO), 200 mM L-glutamine (GIBCO), penicillin (50 IU/mL) and streptomycin (50 mg/L) at 37°C under an atmosphere of humidified air containing 5% CO2. The culture media was sterilized by filtration through 0.2 µm filters.

Sample Preparation

Cells were cultured directly onto a 5x5 mm silicon nitride electron microscopy (EM) window (Silson Ltd., UK), which was placed into an individual well of a 6-well plate and pre-coated with a 0.01% poly-L-lysine solution (Sigma-Aldrich) for 15 min. Upon reaching an optimal confluency, one set of cells was washed with 1X-PBS, fixed with 3.7% PFA for 5 min, washed thoroughly, and further incubated with 5 µM Hoechst 33258 (Acros Organics) for 30 minutes in the dark at room temperature. The other samples were labeled with the Premo FUCCI Cell Cycle Sensor (Invitrogen) according to the manufacturer's instructions. When optimal expression of the sensor was achieved, approximately 24 h following viral transduction, cells were quickly washed with 1X-PBS, fixed with 3.7% PFA for 5 min, washed thoroughly, and mounted onto microscopy slides in 1X-PBS to prevent cells from drying. Images were subsequently acquired using a Zeiss LSM Confocal/NLO 510 microscope equipped with Argon 488, Krypton 568, HeNe 633, and NLO/UV 800 lasers and fitted with a 64X oil immersion objective.

Immediately after Hoechst incubation or fluorescence imaging, samples were prepared for SXRF analysis as previously described [56]. Briefly, cells were thoroughly washed with PBS, rinsed twice with sterile dH2O followed by two brief washes with isotonic ammonium acetate (Sigma-Aldrich, 0.1 M solution in sterile dH2O). Finally, samples were air-dried overnight in a covered sterile cell culture dish.

Synchrotron Radiation X-ray Fluorescence Microscopy (SXRF)

Cells were treated as described above, and, immediately following fluorescence imaging, rinsed quickly with PBS, then twice with isotonic ammonium acetate (0.1 M) prepared in Milli-Q water, and finally dried in air overnight. Synchrotron radiation x-ray fluorescence (SXRF) microscopy was performed at the 2-ID-D beamline of the Advanced Photon Source located at Argonne National Laboratory (IL, USA). The air-dried cells grown on silicon nitride windows were placed onto a kinematic specimen holder suitable for both optical and x-ray fluorescence microscopy. The holder was mounted on a light microscope (Leica DMXRE) and target cells were located on the grid relative to a pre-determined reference point using a motorized x/y stage (Ludl Bioprecision). Coordinates were recorded and used to precisely locate the target cell(s) once the grid was transferred to the microprobe. For cells stained with Hoechst dye, fluorescence images of cells occurring at each phase of mitosis were also acquired using a standard DAPI filter set. For XRF excitation, a monochromatic X-ray beam generated by an undulator source was focused to a spot size of 0.2x0.2 μm^2 on the specimen by using a Fresnel zone plate. An excitation energy of 10 keV was chosen to ensure excitation of all first row transition elements as well as Ca and K, although to a lesser

extent. The sample was subsequently raster scanned through the beam at 298K under a helium atmosphere. The pixel step size was set to 0.2 μm and the entire X-ray spectrum was recorded for each pixel using an energy dispersive germanium detector (Canberra LEGe detector).

Data Analysis

Elemental maps were created by spectral filtering, using spectral regions of interest matched to characteristic x-ray emission lines to determine the fluorescence signal for each element. Calibration to elemental area densities (μg/cm2) was done by comparison of x-ray fluorescence signal strength from the sample to fluorescence from thin film standards NBS-1832 and NBS-1833 from the National Bureau of Standards (NBS/NIST, Gaithersburg, MD) using MAPS software [72]. Elemental content was calculated by fitting of individual spectra of the acquired fluorescence datasets, and comparing fitted fluorescence signal strength to that resulting from fitting of NBS 1832/33 standard spectra.

Acknowledgments

We thank Jonathan Gitlin (Washington University, St. Louis, USA) for providing us with samples of the Atox1$^{-/-}$ and Atox1$^{+/+}$ cell lines. We also thank Stefan Vogt (Argonne National Laboratory) for providing support with the MAPS software. Financial support from the National Institutes of Health (R01GM067169) is gratefully acknowledged. Use of the Advanced Photon Source was supported by the U.S.

Department of Energy, Office of Science, Office of Basic Energy Sciences, under Contract No. DE-AC02-06CH11357.

6.6 Literature Cited

1. Vahrenkamp, H. (2007) Why Does Nature Use Zinc - a Personal View. *Dalton Trans.*, 4751-4759.

2. Andrews, N. C. (2002) Metal Transporters and Disease. *Curr. Opin. Chem. Biol.* **6**, 181-186.

3. De Bie, P., Muller, P., Wijmenga, C., & Klomp, L. W. J. (2007) Molecular Pathogenesis of Wilson and Menkes Disease: Correlation of Mutations with Molecular Defects and Disease Phenotypes. *J. Med. Genet.* **44**, 673-688.

4. Loudianos, G., & Gitlin, J. D. (2000) Wilson's Disease. *Semin. Liver Dis.* **20**, 353-364.

5. Gitlin, J. D. (2003) Wilson Disease. *Gastroenterology* **125**, 1868-1877.

6. Kitzberger, R., Madl, C., & Ferenci, P. (2005) Wilson Disease. *Metab. Brain Dis.* **20**, 295-302.

7. Jansen, J., Karges, W., & Rink, L. (2009) Zinc and Diabetes - Clinical Links and Molecular Mechanisms. *J. Nutr. Biochem.* **20**, 399-417.

8. Bush, A. I. (2000) Metals and Neuroscience. *Curr. Opin. Chem. Biol.* **4**, 184-191.

9. Bush, A. I. (2003) Copper, Zinc, and the Metallobiology of Alzheimer Disease. *Alzheimer Dis. Assoc. Dis.* **17**, 147-150.

10. Gaggelli, E., Kozlowski, H., Valensin, D., & Valensin, G. (2006) Copper Homeostasis and Neurodegenerative Disorders (Alzheimer's, Prion, and Parkinson's Diseases and Amyotrophic Lateral Sclerosis). *Chem. Rev.* **106**, 1995-2044.

11. Barnham, K. J., & Bush, A. I. (2008) Metals in Alzheimer's and Parkinson's Diseases. *Curr. Opin. Chem. Biol.* **12**, 222-228.

12. Macreadie, I. G. (2008) Copper Transport and Alzheimer's Disease. *Eur. Biophys. J. Biophys. Lett.* **37**, 295-300.

13. Colvin, R. A., Bush, A. I., Volitakis, I., Fontaine, C. P., Thomas, D., Kikuchi, K., et al. (2008) Insights into Zn2+ Homeostasis in Neurons from Experimental and Modeling Studies. *Am. J. Physiol.-Cell Physiol.* **294**, C726-C742.

14. Bitanihirwe, B. K. Y., & Cunningham, M. G. (2009) Zinc: The Brain's Dark Horse. *Synapse* **63**, 1029-1049.

15. Sensi, S. L., Paoletti, P., Bush, A. I., & Sekler, I. (2009) Zinc in the Physiology and Pathology of the Cns. *Nat. Rev. Neurosci.* **10**, 780-U738.

16. Kozlowski, H., Janicka-Klos, A., Brasun, J., Gaggelli, E., Valensin, D., & Valensin, G. (2009) Copper, Iron, and Zinc Ions Homeostasis and Their Role in Neurodegenerative Disorders (Metal Uptake, Transport, Distribution and Regulation). *Coord. Chem. Rev.* **253**, 2665-2685.

17. Bohnsack, B. L., & Hirschi, K. K. (2004) Nutrient Regulation of Cell Cycle Progression. *Annu. Rev. Nutr.* **24**, 433-453.

18. Trinkle-Mulcahy, L., & Lamond, A. I. (2007) Toward a High-Resolution View of Nuclear Dynamics. *Science* **318**, 1402-1407.

19. Rafelski, S. M., & Marshall, W. F. (2008) Building the Cell: Design Principles of Cellular Architecture. *Nat. Rev. Mol. Cell Biol.* **9**, 593-602.

20. Uriu-Adams, J. Y., Scherr, R. E., Lanoue, L., & Keen, C. L. (2010) Influence of Copper on Early Development: Prenatal and Postnatal Considerations. *Biofactors* **36**, 136-152.

21. Azman, M. S., Saudi, W. S. W., Ilhami, M., Mutalib, M. S. A., & Rahman, M. T. (2009) Zinc Intake During Pregnancy Increases the Proliferation at Ventricular Zone of the Newborn Brain. *Nutr. Neurosci.* **12**, 9-12.

22. Brandaoneto, J., Stefan, V., Mendonca, B. B., Bloise, W., & Castro, A. V. B. (1995) The Essential Role of Zinc in Growth. *Nutr. Res.* **15**, 335-358.

23. Vallee, B. L., & Auld, D. S. (1993) Zinc - Biological Functions and Coordination Motifs. *Accounts Chem. Res.* **26**, 543-551.

24. Vallee, B. L., & Falchuk, K. H. (1993) The Biochemical Basis of Zinc Physiology. *Physiol. Rev.* **73**, 79-118.

25. Corniola, R. S., Tassabehji, N. M., Hare, J., Sharma, G., & Levenson, C. W. (2008) Zinc Deficiency Impairs Neuronal Precursor Cell Proliferation and Induces Apoptosis Via P53-Mediated Mechanisms. *Brain Res.* **1237**, 52-61.

26. Adamo, A. M., Zago, M. P., Mackenzie, G. G., Aimo, L., Keen, C. L., Keenan, A., et al. (2010) The Role of Zinc in the Modulation of Neuronal Proliferation and Apoptosis. *Neurotox. Res.* **17**, 1-14.

27. Chesters, J. K., & Petrie, L. (1999) A Possible Role for Cyclins in the Zinc Requirements During G1 and G2 Phases of the Cell Cycle. *J. Nutr. Biochem.* **10**, 279-290.

28. Prasad, R., Kaur, G., Nath, R., & Walia, B. N. S. (1996) Molecular Basis of Pathophysiology of Indian Childhood Cirrhosis: Role of Nuclear Copper Accumulation in Liver. *Mol. Cell. Biochem.* **156**, 25-30.

29. Sun, D. X., Zhang, L. Y., Wang, Y. S., Wang, X. L., Hu, X. Y., Cui, F. A., et al. (2007) Regulation of Zinc Transporters by Dietary Zinc Supplement in Breast Cancer. *Mol. Biol. Rep.* **34**, 241-247.

30. Paski, S. C., & Xu, Z. M. (2001) Labile Intracellular Zinc Is Associated with 3t3 Cell Growth. *J. Nutr. Biochem.* **12**, 655-661.

31. Prasad, A. S., Fernandezmadrid, F., & Ryan, J. R. (1977) Thymidine Kinase (Tk) Activity, Ribonucleic Acid Deoxyribonucleic Acid (Rna-DNA), Total Collagen and Protein in Human Zinc-Deficient Tissue. *Clin. Res.* **25**, A523-A523.

32. Wu, F. Y. H., & Wu, C. W. (1987) Zinc in DNA-Replication and Transcription. *Annu. Rev. Nutr.* **7**, 251-272.

33. Macdonald, R. S., Wollard-Biddle, L. C., Browning, J. D., Thornton, W. H., & O'dell, B. L. (1998) Zinc Deprivation of Murine 3t3 Cells by Use of Diethylenetrinitrilopentaacetate Impairs DNA Synthesis Upon Stimulation with Insulin-Like Growth Factor-I (Igf-I). *J. Nutr.* **128**, 1600-1605.

34. Alessandri, G., Raju, K., & Gullino, P. M. (1984) Angiogenesis Invivo and Selective Mobilization of Capillary Endothelium Invitro by Heparin-Copper Complex. **1**, 329-346.

35. Raju, K. S., Alessandri, G., Ziche, M., & Gullino, P. M. (1982) Ceruloplasmin, Copper Ions, and Angiogenesis. *J. Natl. Cancer Inst.* **69**, 1183-1188.

36. Finney, L., Vogt, S., Fukai, T., & Glesne, D. (2009) Copper and Angiogenesis: Unravelling a Relationship Key to Cancer Progression. *Clin. Exp. Pharmacol. Physiol.* **36**, 88-94.

37. Lowndes, S. A., & Harris, A. L. (2005) The Role of Copper in Tumour Angiogenesis. *J. Mammary Gland Biol. Neoplasia* **10**, 299-310.

38. Pan, Q., Kleer, C. G., Van Golen, K. L., Irani, J., Bottema, K. M., Bias, C., et al. (2002) Copper Deficiency Induced by Tetrathiomolybdate Suppresses Tumor Growth and Angiogenesis. *Cancer Res.* **62**, 4854-4859.

39. Chen, K. G., Valencia, J. C., Lai, B., Zhang, G. F., Paterson, J. K., Rouzaud, F., et al. (2006) Melanosomal Sequestration of Cytotoxic Drugs Contributes to the Intractability of Malignant Melanomas. *Proc. Natl. Acad. Sci. U. S. A.* **103**, 9903-9907.

40. Hassouneh, B., Islam, M., Nagel, T., Pan, Q., Merajver, S. D., & Teknos, T. N. (2007) Tetrathiomolybdate Promotes Tumor Necrosis and Prevents Distant Metastases by Suppressing Angiogenesis in Head and Neck Cancer. *Mol. Cancer Ther.* **6**, 1039-1045.

41. Du, T., Filiz, G., Caragounis, A., Crouch, P. J., & White, A. R. (2008) Clioquinol Promotes Cancer Cell Toxicity through Tumor Necrosis Factor Alpha Release from Macrophages. *J. Pharmacol. Exp. Ther.* **324**, 360-367.

42. Tardito, S., & Marchio, L. (2009) Copper Compounds in Anticancer Strategies. *Curr. Med. Chem.* **16**, 1325-1348.

43. Rudolf, E., & Cervinka, M. (2008) External Zinc Stimulates Proliferation of Tumor Hep-2 Cells by Active Modulation of Key Signaling Pathways. *J. Trace Elem. Med. Biol.* **22**, 149-161.

44. Hashemi, M., Ghavami, S., Eshraghi, M., Booy, E. P., & Los, M. (2007) Cytotoxic Effects of Intra and Extracellular Zinc Chelation on Human Breast Cancer Cells. *Eur. J. Pharmacol.* **557**, 9-19.

45. Huesca, M., Lock, L. S., Khine, A. A., Viau, S., Peralta, R., Cukier, I. H., et al. (2009) A Novel Small Molecule with Potent Anticancer Activity Inhibits Cell Growth by Modulating Intracellular Labile Zinc Homeostasis. *Mol. Cancer Ther.* **8**, 2586-2596.

46. Kim, I., Lee, K. S., Hwang, J. S., Ahn, M. Y., Yun, E. Y., Li, J. H., et al. (2006) Molecular Cloning and Characterization of Atx1 Cdna from the Mole Cricket, Gryllotalpa Orientalis. *Arch. Insect Biochem. Physiol.* **61**, 231-238.

47. Kim, B. E., & Petris, M. J. (2007) Phenotypic Diversity of Menkes Disease in Mottled Mice Is Associated with Defects in Localisation and Trafficking of the Atp7a Protein. *J. Med. Genet.* **44**, 641-646.

48. Binnebosel, M., Grommes, J., Koenen, B., Junge, K., Klink, C. D., Stumpf, M., et al. (2010) Zinc Deficiency Impairs Wound Healing of Colon Anastomosis in Rats. *Int. J. Colorectal Dis.* **25**, 251-257.

49. Outten, C. E., & O'halloran, T. V. (2001) Femtomolar Sensitivity of Metalloregulatory Proteins Controlling Zinc Homeostasis. *Science* **292**, 2488-2492.

50. Mcrae, R., Lai, B., & Fahrni, C. J. (2010) Copper Redistribution in Atox1-Deficient Mouse Fibroblast Cells. *J. Biol. Inorg. Chem.* **15**, 99-105.

51. Sakaue-Sawano, A., Kurokawa, H., Morimura, T., Hanyu, A., Hama, H., Osawa, H., et al. (2008) Visualizing Spatiotemporal Dynamics of Multicellular Cell-Cycle Progression. *Cell* **132**, 487-498.

52. Latt, S. A., Stetten, G., Juergens, L. A., Willard, H. F., & Scher, C. D. (1975) Recent Developments in Detection of Deoxyribonucleic-Acid Synthesis by 33258-Hoechst Fluorescence. *J. Histochem. Cytochem.* **23**, 493-505.

53. Latt, S. A., & Wohlleb, J. C. (1975) Optical Studies of Interaction of 33258 Hoechst with DNA, Chromatin, and Metaphase Chromosomes. *Chromosoma* **52**, 297-316.

54. Latt, S. A., & Stetten, G. (1976) Spectral Studies on 33258-Hoechst and Related Bisbenzimidazole Dyes Useful for Fluorescent Detection of Deoxyribonucleic-Acid Synthesis. *J. Histochem. Cytochem.* **24**, 24-33.

55. Yang, L. C., Mcrae, R., Henary, M. M., Patel, R., Lai, B., Vogt, S., et al. (2005) Imaging of the Intracellular Topography of Copper with a Fluorescent Sensor and by Synchrotron X-Ray Fluorescence Microscopy. *Proc. Natl. Acad. Sci. U. S. A.* **102**, 11179-11184.

56. Mcrae, R., Lai, B., Vogt, S., & Fahrni, C. J. (2006) Correlative Microxrf and Optical Immunofluorescence Microscopy of Adherent Cells Labeled with Ultrasmall Gold Particles. *J. Struct. Biol.* **155**, 22-29.

57. Shakib, K., Norman, J. T., Fine, L. G., Brown, L. R., & Godovac-Zimmermann, J. (2005) Proteomics Profiling of Nuclear Proteins for Kidney Fibroblasts Suggests Hypoxia, Meiosis, and Cancer May Meet in the Nucleus. *Proteomics* **5**, 2819-2838.

58. Tapiero, H., & Tew, K. D. (2003) Trace Elements in Human Physiology and Pathology: Zinc and Metallothioneins. *Biomed. Pharmacother.* **57**, 399-411.

59. Tal, M. (1969) Metal Ions and Ribosomal Conformation. **195**, 76-&.

60. Tal, M. (1968) On Role of Zn2+ and Ni2+ in Ribosome Structure. **169**, 564-&.

61. Chvapil, M. (1973) New Aspects in Biological Role of Zinc - Stabilizer of Macromolecules and Biological-Membranes. *Life Sci.* **13**, 1041-1049.

62. Maret, W., & Li, Y. (2009) Coordination Dynamics of Zinc in Proteins. *Chem. Rev.* **109**, 4682-4707.

63. Scholey, J. M., Brust-Mascher, I., & Mogilner, A. (2003) Cell Division. *Nature* **422**, 746-752.

64. Gaietta, G. M., Giepmans, B. N. G., Deerinck, T. J., Smith, W. B., Ngan, L., Llopis, J., et al. (2006) Golgi Twins in Late Mitosis Revealed by Genetically Encoded Tags for Live Cell Imaging and Correlated Electron Microscopy. *Proc. Natl. Acad. Sci. U. S. A.* **103**, 17777-17782.

65. Muto, A., Kume, S., Inoue, T., Okano, H., & Mikoshiba, K. (1996) Calcium Waves Along the Cleavage Furrows in Cleavage-Stage Xenopus Embryos and Its Inhibition by Heparin. *J. Cell Biol.* **135**, 181-190.

66. Noguchi, T., & Mabuchi, I. (2002) Localized Calcium Signals Along the Cleavage Furrow of the Xenopus Egg Are Not Involved in Cytokinesis. *Mol. Biol. Cell* **13**, 1263-1273.

67. Webb, S. E., Li, W. M., & Miller, A. L. (2008) Calcium Signalling During the Cleavage Period of Zebrafish Development. *Philos. Trans. R. Soc. B-Biol. Sci.* **363**, 1363-1369.

68. Mullins, J. M., & Mcintosh, J. R. (1982) Isolation and Initial Characterization of the Mammalian Mid-Body. *J. Cell Biol.* **94**, 654-661.

69. Dan, K., & Tanaka, Y. (1990) Attachment of One Spindle Pole to the Cortex in Unequal Cleavage. *Ann. N.Y. Acad. Sci.* **582**, 108-119.

70. Skop, A. R., & White, J. G. (1998) The Dynactin Complex Is Required for Cleavage Plane Specification in Early Caenorhabditis Elegans Embryos. *Curr. Biol.* **8**, 1110-1116.

71. Miller, R. K., Cheng, S. C., & Rose, M. D. (2000) Bim1p/Yeb1p Mediates the Kar9p-Dependent Cortical Attachment of Cytoplasmic Microtubules. *Mol. Biol. Cell* **11**, 2949-2959.

72. Vogt, S., Maser, J., & Jacobsen, C. (2003) Data Analysis for X-Ray Fluorescence Imaging. *J. Phys. IV* **104**, 617-622.

Chapter 7: Future Directions

The results presented in this thesis have paved a route with many new roads for future exploration. The observations of intriguing re-distributions of copper and zinc and the fascinating three-fold increase in zinc content occurring as cells entered mitosis are of particular interest given the potential implication of these results to the field of cancer research. A number of future research investigations, highlighted below, are devoted specifically towards understanding the roles played by copper and zinc in the normal progression of mammalian cells through their cell cycle.

One investigation would involve elucidating the percentage of the copper and zinc that undergoes the major re-distribution and influx, in the case of zinc, that is labile metal. The Cu(I)-selective and Zn(II)-selective fluorescence probes introduced in the first half of this thesis could be applied directly to cells and correlated with the corresponding SXRF elemental distribution maps for cells undergoing mitosis. Another interesting study would involve determining the intracellular structures or organelles associated with copper and zinc during mitosis. This could be determined using the correlative imaging method developed in Chapter 4 of this thesis. After answering these questions, a next effort would entail an analysis of the quantitative metal distributions occurring in diseased-model cell lines, particularly those representing various forms of cancer, via SXRF microscopy. While these are only a few examples of the many possibilities for future investigations, they represent the fundamental significance and underscore the potentially high impact such research holds in the medical field.